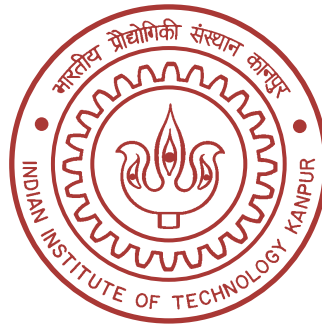


Statistical properties of rapidly rotating turbulence

by

Manohar Kumar Sharma



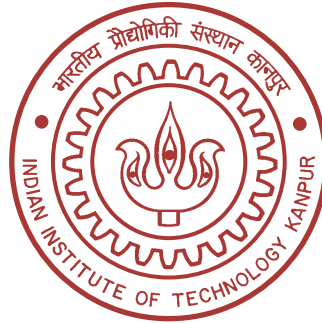
DEPARTMENT OF PHYSICS
INDIAN INSTITUTE OF TECHNOLOGY KANPUR
November, 2019

Statistical properties of rapidly rotating turbulence

A Thesis Submitted
in Partial Fulfilment of the Requirements
for the Degree of
Doctor of Philosophy

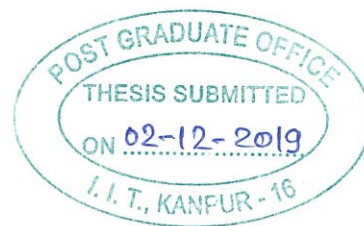
by

Manohar Kumar Sharma



to the
DEPARTMENT OF PHYSICS
INDIAN INSTITUTE OF TECHNOLOGY KANPUR
November, 2019

Certificate



It is certified that the work contained in the thesis titled "Statistical properties of rapidly rotating turbulence", by Manohar Kumar Sharma, has been carried out under our supervision and that this work has not been submitted elsewhere for a degree.

Handwritten signature of Prof. Sagar Chakraborty in black ink.

Prof. Sagar Chakraborty
(Thesis Supervisor)
Department of Physics
IIT Kanpur
Kanpur - 208016
India

Handwritten signature of Prof. Mahendra K. Verma in black ink.

Prof. Mahendra K. Verma
(Thesis Co-Supervisor)
Department of Physics
IIT Kanpur
Kanpur - 208016
India

November, 2019

Declaration

This is to certify that the thesis titled **Statistical properties of rapidly rotating turbulence** has been authored by me. It presents the research conducted by me under the supervision of **Prof. Sagar Chakraborty and Prof. Mahendra Kumar Verma**. To the best of my knowledge, it is an original work, both in terms of research content and narrative, and has not been submitted elsewhere, in part or in full, for a degree. Further, due credit has been attributed to the relevant state-of-the-art and collaborations (if any) with appropriate citations and acknowledgements, in line with established norms and practices.

Signature *Manohar Kr. Sharma*

Name: Manohar Kumar Sharma.
Programme: PhD
Department: Physics
Indian Institute of Technology Kanpur
Kanpur 208016

Synopsis

Name	: Manohar Kumar Sharma
Roll No.	: 13109881
Degree for which submitted	: Doctor of Philosophy
Department	: Physics
Title of the Thesis	: Statistical properties of rapidly rotating turbulence
Thesis Supervisors	: Prof. Sagar Chakraborty Prof. Mahendra Kumar Verma
Month and year of submission	: November, 2019

Turbulence is an omnipresent phenomenon observed at all scales from a cup of coffee being stirred to intracluster medium in the galaxy cluster. Although turbulence is observed ubiquitously in nature, it is not straightforward to provide a precise definition for turbulent flows. Usually, it is characterized by randomness in velocity and vorticity fields, high diffusivity, dissipation, and strong nonlinearity in the flow. Being inherently random in nature, it is best studied statistically. It is well known that Kolmogorov [1] proposed an inertial range energy spectrum for homogeneous and isotropic three-dimensional (3D) hydrodynamics turbulence: $E(k) \sim \epsilon^{2/3} k^{-5/3}$, where ϵ is the constant energy dissipation rate and k is wavenumber. The Kolmogorov spectrum is quite universal and observed in a plethora of other realistic settings, e.g., shear flows [2], viscoelastic fluids [3], buoyancy-driven systems [4], and jet flows [5]. On the other hand, the energy cascade for the two-dimensional (2D) turbulent system shows

[1] A.N. Kolmogorov, *The local structure of turbulence in incompressible viscous fluid for very large Reynolds numbers*, *Dokl. Akad. Nauk SSSR* **30**, p. 301-305 (1941).

[2] G.E. Elsinga, *The anisotropic structure of turbulence and its energy spectrum*, *Phys. Fluids* **28**, p. 011701 (2016).

[3] P.C. Valente et al., *Energy spectra in elasto-inertial turbulence*, *Phys. Fluids* **28**, p. 075108 (2016).

[4] M. K. Verma, *Physics of Buoyant Flows: From Instabilities to Turbulence*, World Scientific, Singapore, 2018.

[5] P. Buchhave and C. M. Velte, *Measurement of turbulent spatial structure kinetic energy spectrum by exact temporal-to-spatial mapping*, *Phys. Fluids* **29**, p. 085109 (2017).

dual behaviour [6] [7]: an inverse cascade at large scales with $E(k) \sim k^{-5/3}$ and a forward cascade of enstrophy at relatively smaller scales with $E(k) \sim k^{-3}$.

While turbulence itself is an intricate phenomenon, the presence of rotation makes it even more complex. Rotating turbulence [8]—turbulence in rotating fluids—is a commonly occurring phenomenon in the geophysical and the astrophysical flows. It also occurs in the engineering flows like the ones in turbo-machinery and reciprocating engines with swirl and tumble. The large-scale structures of the turbulent system are affected by rotation due to the Coriolis force that acts in the plane perpendicular to the direction of angular velocity. Intriguingly, the scaling law of the energy spectrum in the inertial range changes with the rotation rate in a way so as to two-dimensionalize the 3D fluid turbulence.

The energy transfer between different scales is a defining feature of any kind of turbulent flow. This exchange of energy in the system occurs owing to the nonlinear interactions among different scales. In 3D (non-rotating) isotropic homogeneous turbulence, the nonlinear terms in the Navier–Stokes (NS) equations are solely responsible for the transfer of energy from the larger scales (where energy is usually injected into the system) to the smaller scales (where energy is dissipated into heat by viscous term). The case of the rapidly rotating 3D turbulence is, however, much more involved not only because of the introduction of another time-scale in the problem but also because the system is predominantly anisotropic. Thus, in order to understand the system, an understanding of the anisotropic properties of the energy transfer is paramount.

The Reynolds number (a non-dimensional number) is an important parameter in the study of turbulence in fluid flows. It is the ratio of the inertial force to the viscous force of the flow. Apart from the Reynolds number in 3D turbulence, rotation introduces a new non-dimensional number called Rossby number (Ro). The Rossby number is the ratio of the inertial force and the Coriolis force. Low Ro corresponds to the high rotation rate. The Rossby number for the solar dynamo should be $\mathcal{O}(10^{-2})$, whereas for the geodynamo of the Earth is $\mathcal{O}(10^{-6})$. The Rossby number for the Earth and the Mars atmosphere is $\mathcal{O}(10^{-1})$ and for the Venus 10 – 50. The tornadoes have Rossby number of the order of 10^3 , and large ocean flows have $\text{Ro} \sim 10^{-2}$.

[6] R. H. Kraichnan, *Inertial ranges in two-dimensional turbulence*, *Phys. Fluids* **10**, p. 1417 (1967).

[7] J. Paret and P. Tabeling, *Experimental observation of the two-dimensional inverse energy cascade*, *Phys. Rev. Lett.* **79**, p. 4162 (1997).

[8] P. A. Davidson, *Turbulence in Rotating, Stratified and Electrically Conducting Fluids*, Cambridge University Press, Cambridge UK, 2013.

The nonlinear interactions between different scales cause the transfer of energy from one scale to another scale. In turbulence, the energy injected at a larger scale goes down to smaller scales and dissipate at the Kolmogorov dissipation scale. The Kolmogorov dissipation scale ($k_\eta = (\epsilon/\nu^3)^{1/4}$) corresponds to the scale where the nonlinear term is comparable to the viscous dissipation term. This is the mechanism for energy transport in 3D homogeneous and isotropic turbulence. In the case of rotation, rotation introduces another scale called the Zeman scale [9], $k_\Omega = (\Omega^3/\epsilon)^{1/2}$, in the rotating turbulent flows. The Zeman scale corresponds to the scale where the inertial force is comparable to the Coriolis force in the system. The behavior of the kinetic energy spectrum may change due to the dominance of the Coriolis force up to the wavenumber k_Ω . The behavior of the kinetic energy spectrum in the two different wavenumber regions, $k < k_\Omega$, and $k > k_\Omega$, is still not completely understood. Zeman proposed a model for the kinetic energy spectrum of the rotating turbulence, where the energy scales as $k^{-11/5}$ in wavenumber range $k < k_\Omega$, and $k^{-5/3}$ in range $k > k_\Omega$. The Coriolis force in the rotating turbulence makes the flow anisotropic. It is good, however, more meaningful to investigate the anisotropic behavior of the energy spectrum. A model for the scaling of the anisotropic kinetic energy spectrum was proposed by Galtier [10].

There are two approaches to study the turbulent systems: (a) deterministic approach, and (b) statistical approach. In the deterministic approach, researchers study the behavior of the flow as a dynamical system and the stabilities of the flows in various situations. On the other hand, in the statistical approach, researchers try to model the statistical quantities of the flow. Many researchers conduct experiments and numerical simulations to investigate the statistical properties of the turbulence. In our study, we follow the statistical approach to explore the energetics of rotating turbulence numerically. Specifically, in this thesis we ask the following questions: (a) what is the scaling of the kinetic energy spectrum in the lower wavenumber region and in the far dissipation range, and (b) what is the nature of energy transfers due to the anisotropy induced by rotation in the system? These questions are not completely understood. With a view to gaining insight into these issues, we investigate the behavior of the kinetic energy spectrum and the kinetic energy flux in the rotating turbulent flows using numerical simulations and phenomenological modeling.

[9] O. Zeman, *A note on the spectra and decay of rotating homogeneous turbulence*, *Phys. Fluids* **6**, p. 3221-3224 (1994).

[10] S. Galtier, *Weak inertial-wave turbulence theory*, *Phys. Rev. E* **68**, p. 015301 (2003).

To this end, we simulate the governing NS equations in a cubic periodic box of box-size $(2\pi)^3$. We use the pseudo-spectral code **Tarang** [11] [12] for numerical simulation. We have performed a direct numerical simulation of decaying and forced rotating turbulence for the grid resolutions of 512^3 and 1024^3 . The Reynolds number is high $\mathcal{O}(10^3)$ and the Rossby number is quite low $\mathcal{O}(10^{-3})$. We have investigated the scaling of the kinetic energy spectrum for the decaying and the forced rotating turbulent flows. We have also investigated the behavior of the kinetic energy spectrum in the far dissipation range for forced rotating turbulence. We have studied the role of the rotation in the anisotropic energy transfer due to nonlinear interactions in velocity fields. The measures of the energy transfer are shell-to-shell energy transfer, flux, ring-to-ring energy transfer. We have studied these transfers in minute detail. Our main findings for the rotating turbulence are as follows:

- In the case of decaying rotating turbulence, we have observed that the most energetic modes in Fourier space are $(\pm 1, 0, 0)$ and $(0, \pm 1, 0)$ and our proposed model for kinetic energy spectrum is quite good in agreement with numerical data [13].
- We have observed that the kinetic energy spectrum of the forced rotating turbulence follows Kuznetsov–Zakharov–Kolmogorov (KZK) scaling in lower wavenumber range, and exhibits exponential behavior in the far dissipation range [14].
- Our extensive study of anisotropic energy transfers shows that the kinetic energy is transferred from the polar region to the equatorial region in both the cases of decaying and forced rotating turbulence [15].

In this thesis that is arranged into following six chapters, we essentially present the details behind these findings:

[11] M. K. Verma, A. G. Chatterjee, K.S. Reddy, R. Yadav, S. Paul, M. Chandra, and R. Samtaney *Benchmarking and scaling studies of pseudo-spectral code Tarang for turbulence simulations*, *Pramana* **81**, p. 617-629 (2013).

[12] A. G. Chatterjee, M. K. Verma, A. Kumar, R. Samtaney, B. Hadri, and R. Khurram, *Scaling of a fast Fourier transform and a pseudo-spectral fluid solver up to 196608 cores*, *J. Parallel Distrib. Comput.* **113**, p. 77-91 (2018).

[13] Manohar K. Sharma, Abhishek Kumar, Mahendra K. Verma, and Sagar Chakraborty, *Statistical features of rapidly rotating decaying turbulence: Enstrophy and energy spectra and coherent structures*, *Phys. Fluids* **30**, p. 045103 (2018).

[14] Manohar K. Sharma, Mahendra K. Verma, and Sagar Chakraborty, *On the energy spectrum of rapidly rotating forced turbulence*, *Phys. Fluids* **30**, p. 115102 (2018).

[15] Manohar K. Sharma, Mahendra K. Verma, and Sagar Chakraborty, *Anisotropic energy transfers in rapidly rotating turbulence*, *Phys. Fluids* **31**, p. 085117 (2019).

-
- In chapter 1, we introduce governing equations, essential parameters, and invariant quantities of the system. Further, we discuss the statistical properties like the kinetic energy spectrum of 3D and 2D turbulence. We also present the available literature survey on the kinetic energy spectrum, kinetic energy fluxes for the decaying, and the forced rotating turbulence.
 - In chapter 2, we discuss the numerical scheme employed to solve the governing equation of flow. We also discuss the formulation of the kinetic energy spectrum, the kinetic energy flux, the shell-to-shell energy transfer, the ring-to-ring energy transfer, and the Conical flux in the rotating turbulence. We discuss the initial conditions and the random forcing scheme as employed in the simulations.
 - In chapter 3, we investigate the energy spectrum and structures of rapidly rotating decaying turbulence. Here we focus on the nonhelical flows (zero kinetic helicity). We perform sufficiently high-resolution spectral simulations that help us analyze the asymptotic regime. We find that as the turbulent flow evolves in time, the Rossby number decreases to $\sim 10^{-3}$, and the flow becomes quasi-two-dimensional with strong coherent columnar structures arising due to the inverse cascade of energy. We establish that a major fraction of energy is confined in Fourier modes $(\pm 1, 0, 0)$ and $(0, \pm 1, 0)$ that corresponds to the largest columnar structure in the flow. Following the earlier works on rotating turbulence, we observe a strong inverse cascade of energy that strengthens the coherent columnar structures. The kinetic energy trapped in such structures dissipates very slowly, and hence the Reynolds number remains quite large with slow variation in time. For wavenumbers (k) greater than the enstrophy dissipation wavenumber (k_d), our phenomenological arguments and numerical study show that the enstrophy flux and spectrum of a horizontal cross-section perpendicular to the axis of rotation are given by $\epsilon_\omega \exp(-C(k/k_d)^2)$ and $C\epsilon_\omega^{2/3}k^{-1} \exp(-C(k/k_d)^2)$ respectively; for this 2D flow, ϵ_ω is the enstrophy dissipation rate, and C is a constant. Using these results, we propose a new form for the energy spectrum of rapidly rotating decaying turbulence: $E(k) = C\epsilon_\omega^{2/3}k^{-3} \exp(-C(k/k_d)^2)$. This model of the energy spectrum is based on wavenumber-dependent enstrophy flux, and it deviates significantly from the power-law energy spectrum reported earlier.
 - In chapter 4, we investigate the behavior of the kinetic energy spectrum for the forced rotating turbulence. The introduction of forcing at an intermediate scale—corresponding wavenumber being k_f —breaks the kinetic energy spectrum into

two disjoint region: larger scales $k < k_f$ and smaller scales $k > k_f$. Contrary to what has been observed in the decaying case, the energy spectrum in the forced case shows power law scaling close to $E(k_\perp, k_\parallel) \sim k_\perp^{-5/2} k_\parallel^{-1/2}$ in highly anisotropic large scales. (The subscripts ' \perp ' and ' \parallel ' respectively refer to the directions perpendicular and parallel to the rotation axis). In the rather isotropic far dissipation range, the energy spectrum becomes exponential function of ' $-k$ '. Additionally, although we have observed that $(\pm 1, 0, 0)$ and $(0, \pm 1, 0)$ still contain a major fraction of the total energy, the energy content in the intermediate and the smaller scales is much more than that for the decaying rotating turbulent; as a result, one observes rather diffused columnar structures in case of forced rotating turbulence. The main aim of our thesis is to elaborate on these interesting results and to contrast the forced turbulence with the decaying one.

- In chapter 5, we have performed direct numerical simulations of 512^3 grid resolution for the decaying as well as the forced rotating turbulent fluids, and investigated the anisotropic nature of the transfer of energy. As the main result, we establish that the energy is transferred from the polar region to the equatorial region in the case of the decaying rotating turbulence. However, for the case of the forced rotating turbulence, we have observed two different types of energy transfers: (a) in wavenumber-region $|\mathbf{k}| < k_f$ (where \mathbf{k} is the wave vector and k_f is the forcing wavenumber), the energy is transferred from the equatorial region to the polar region; and (b) in region $|\mathbf{k}| > k_f$, the energy is transferred from the poles towards the equator.
- Finally, in chapter 6, we summarize our results on the rotating turbulence and discuss some future directions of research in the context of our work.

Acknowledgements

I start with a quote "When one door closes, another opens; but we often look so long and so regretfully upon the closed door that we do not see the one that has opened for us" written by Alexander Graham Bell. The person who, helps to identify the open door has a significant role in making anyone future. For a Ph.D. student, it is the supervisor who helps to identify the open door.

So first of all, I would like to express my sincere gratitude to my thesis supervisors, Prof. Sagar Chakraborty and Prof. Mahendra Kumar Verma, for their continuous support, guidance, and patience throughout my Ph.D. days. It is a privilege for me to work under these two intelligent and hardworking people. I learned a lot of things from them, including scientific temperament, more specifically scientific writing and presentation skills. Their suggestions helped me a lot in my scientific oral presentation. I learned a lot of things from Prof. Mahendra K. Verma, especially from the courses on turbulence, parallel programming, computational physics, etc. Prof. Verma has a great ability to find compelling research problems. He only engaged with his research work and new ideas, which inspires a lot. I learned nonlinear dynamics from Prof. Sagar Chakraborty through his Course on nonlinear dynamics. These courses help me in my research works. I would like to thanks my senior and collaborator, Dr. Abhishek Kumar, for his continuous guidance and moral supports. He helped me a lot in initial phase of this journey. I also thank Mr. Biplab Dutta for his data, which helped me in the initial stage of my numerical simulations.

I am grateful to my peer-review committee members: Prof. Anand Kumar Jha, Prof. Supratik Banerjee, Prof. Saikat Ghosh, for their valuable suggestion and constant encouragement, which help me to finish this endless journey of Ph.D. I am thankful to the teachers who taught me during my master's and Ph.D. I am especially thankful to Prof. Manoj Kumar Harbola, Prof. Tarun Kanti Ghosh. Prof. Kausik Bhattacharje who introduce me to different realities of physics. I thank Prof. Anirban Guha, who taught me geophysical fluid dynamics, which helps in my research work. I would like to acknowledge all staff members of the department of physics for their kind supports. I would like to thank all the teaching and non-teaching staff of IIT Kanpur.

I start with another quote, "In life have a friend that is like a mirror and shadow; Mirror doesn't lie, and shadow never leaves." During my Ph.D. I have two close friends Dr. Primtam Kumar Roy and Shailendra Rathor. They are like my mirror and shadow;

whenever I made a mistake, they point it out tried to mend it. They are also like my shadow; during my tough time of Ph.D., they are always with me in every moment. This journey is not possible without them. I would like to thank the founding members of Manohar palace, especially Manu Mannatil, Rohitashwa Chatopadhyay, Asutosh Singh, and Depnajan Dey, and Dr. Manish Kaushal for their co-operation to run Manohar Palace. I am also thankful to Manu Mannatil to help me in coding in my initial phase of Ph.D.

Further, I would like to thank all my lab mates, specially Shubhadeep Sadhukhan, Anupam Ghosh, Suman, Archan Mukhopadhyay, Anurag Sharma, Versa Pawar, Sourav Mittal, Roshan Samuels, Shasawat Bhattacharjee, Soumaydeep, Mohamed Anas, Shadab Aalam to maintain the lab decorum. I thank Anando Gopal Chatterjee for his help in computational related issues. I am also thankful to my seniors Dr. Ambrish Pandey, Sandeep Reddy, late Dr. Rohit Kumar, for the encouragement and healthy discussion of research related problems. I would like to thank Kabyashree Sonowal for encouraging me and their motivational quotes. I am also thankful to Dr. Akanksha Gupta for a healthy discussion on two-dimensional turbulence and research related topics. I thank Shailendra Rathor, Rohitashawa, Dr. Akanksha Gupta, Anas, and Roshan Samuels to read the preprint of my thesis.

I am thankful to the developers of open source packages, especially late John Hunter, for developing *matplotlib*. In my research work, I used *python* which includes *matplotlib*. I would like to acknowledge HPC2010, HPC2013, and Chaos of IIT Kanpur for providing computational facilities.

I am thankful to Roshan Bhaskaran and Manmohan Debvanshi, who helped me with lab-related issues. I thank Mr. Arvind Mishara, Mr. Vishal Garg, and Mr. Vivek Garg for their help in computer-related issues.

I am thankful to anonymous referees and editors for their comments and suggestion, which improved the quality of our research papers. I am thankful to the various funding agencies, Science and Engineering Research Board (SERB), Department of Science and Technology (DST), IIT Kanpur, and Russian Science Foundation Russia for providing the funds to my supervisors who helped me pursue my research work. I am also thankful to ICTS Bangalore to organizes conferences on turbulence time-to-time, which helps me to exchange the knowledge with the experts in my fields.

My stay in IIT Kanpur would not have enjoyable without some good friends.

I thank all my friends and seniors Divya Jyoti Sivananda, Sourav Baruwa, Gaurav Goswami, Saurav Bhattarjee, Indrajeet, and other friends whose names are not here. I also enjoyed the company of my batch mates Arif Warsi Lasker, Kamalika Nath, Ankit Kumar, Pramod Ghishing, Shamik Ghosh, Tanmay Majhi, Depanwita Ghanti, Ankit Sharma, Rahul Saini, and Ashish. I would also thank the friends in my badminton court, with whom I usually played badminton in New SAC.

I can not think about this journey without the support of my parents and my siblings. My family members, especially my Mom, who always encourage me in my tough period of Ph.D. My father is very supportive and always encourage me. He usually tells me that do whatever you want, don't regret failure, and fight like warriors, which encourage me. I would like to thank my childhood friends Asit Mahato, Shekhar Pandey, Ajay Kumar Ram, and Shankar Mahato, for their company. In the end, I thank the almighty God for their invisible supports, which helps me to believe in my self and pursue my dreams.

November, 2019

Manohar Kumar Sharma

To my family and teachers...

List of Publications

- **Publications included in the thesis:**

1. **M.K. Sharma***, A. Kumar, M.K. Verma and S. Chakraborty, “*Statistical features of rapidly rotating decaying turbulence: Enstrophy and energy spectra and coherent structures*”, *Phys. Fluids*. **30**, 045103 (2018). [Editor’s picks]
2. **M.K. Sharma***, M.K. Verma and S. Chakraborty, “*On the energy spectrum of rapidly rotating forced turbulence*”, *Phys. Fluids*. **30**, 115102 (2018). [Featured article]
3. **M.K. Sharma***, M.K. Verma and S. Chakraborty, “*Anisotropic energy transfer in rapidly rotating turbulence*”, *Phys. Fluids*. **31**, 0851117 (2019).

*Corresponding author

Contents

Thesis Synopsis	vii
Acknowledgements	xiii
List of Publications	xix
Table of Contents	xxi
List of Figures	xxv
List of Tables	xxxv
1 Introduction	1
1.1 Introduction	1
1.1.1 Experimental setups of rotating turbulence	3
1.2 Governing equations	6
1.2.1 Governing equations in rotating frame of reference	6
1.3 Two-dimensionalisation through rotation	12
1.3.1 Two-dimensional turbulence	19
1.3.2 Towards rotating turbulence	20
1.3.3 Phenomenological model	21

CONTENTS

1.4	Literature survey on rotating turbulence	23
1.4.1	Coherent structures	24
1.4.2	Kinetic energy spectrum	25
1.4.3	Kinetic energy transfer in rotating turbulence	28
1.5	Outline of the thesis	30
2	Numerical scheme to compute statistical quantities	33
2.1	Simulation method	34
2.2	Initial condition and forcing scheme	38
2.3	Kinetic energy spectrum	39
2.4	Kinetic energy transfer	43
2.5	Simulation parameters	46
2.6	Summary	47
3	Coherent structures and modeling of energy spectrum of decaying rotating turbulence	49
3.1	Phenomenology of rotating turbulence	50
3.2	Evolution of system parameters	53
3.3	Columnar structures and associated Fourier modes	56
3.4	Energy and enstrophy fluxes and spectra	61
3.5	Summary	67
4	Energy spectrum of rotating forced turbulence	69
4.1	Quasi-two-dimensionalization	70
4.1.1	Large scale coherent structures	71
4.1.2	Inverse energy cascade	74
4.2	The energy spectrum	74
4.2.1	Model spectrum for smaller scales	75
4.2.2	Model spectrum near larger scales	79
4.3	Summary	80

CONTENTS

5	Anisotropic energy transfer in rotating turbulence	81
5.1	Ring energy spectrum	82
5.2	Shell to shell energy transfer	84
5.3	Ring-to-ring energy transfer	86
5.4	Summary	90
6	Discussions and conclusions	93
6.1	Conclusions of the thesis	93
6.2	Future directions	96
A	Appendix	99
A.1	Finite-size effects	99
A.2	Fourier modes $(1, 0, 0)$ and $(0, 1, 0)$ in rotating turbulence	100
A.3	Comparison between our model and that of Pao's model	101
A.4	Inverse Enstrophy Cascade	102
A.5	Anisotropic Energy Spectrum's Scaling With k_{\parallel}	104
A.6	Integral length scale in decaying rotating turbulence	106
A.7	Statistical properties of forced rotating turbulence	107
A.8	Scale dependent anisotropy in decaying rotating turbulence	110
	Bibliography	111

List of Figures

1.1	A schematic diagram of an experimental setup [1] of rotating turbulence: A Plexiglas cylindrical water tank is kept on a rotating platform and energy is injected from the bottom. A horizontal laser sheet is used to illuminate a horizontal cross-sectional area, and a co-rotating camera on the top..	4
1.2	A schematic diagram of an experimental setup [2] of rotating turbulence: A cubical water tank is kept on a rotating and the turbulence in the system is generated by towing a grid with velocity V_g	5
1.3	Schematic diagram shows how the energy in a sphere is affected by other terms in the energy evolution equation. This figure is adapted from a figure from Ref. [3].	10
1.4	A schematic diagram [3] to shows the rate of transfer of energy from a shell.	11
1.5	Schematic diagram [4] of kinetic energy spectrum for 3D homogeneous and isotropic turbulence.	15

LIST OF FIGURES

1.6	Schematic diagram [4] of kinetic energy spectrum for 2D homogeneous and isotropic turbulence.	19
1.7	Schematic diagram for the comparison of different wavenumbers in rotating turbulence.	20
2.1	Schematic diagram for the computation of nonlinear term $(\mathbf{u} \cdot \nabla) \mathbf{u}$ by pseudo-spectral method. This figure is adapted from a figure from Ref. [3].	36
2.2	The plots show the schematic diagram of, (a) ring decomposition in Fourier space, (b) cross-sectional view of shells, sectors and rings, (c) conical energy flux $\Pi(\theta)$: the rate of transfer of energy from the modes inside the cone of semi-vertical angle θ to the modes outside the cone. This figure is adapted from a figure from Ref. [5].	39
2.3	Schematic diagram of Fourier space decomposed in cylindrical rings. . .	41
2.4	Schematic diagram for the computation of kinetic energy flux for a sphere of radius k_0 in Fourier space. This figure is adapted from a figure from Ref. [3].	44
2.5	Schematic diagram for the computation of shell-to-shell energy transfer. This figure is adapted from a figure from Ref. [3].	45
3.1	For 1024^3 (red dashed) and 512^3 (blue) grids simulation with $\Omega = 16$, variation of characteristic system parameters with time t : (a) the total energy $E(t)$, (b) the integral length scale, L , (c) the Reynolds number, Re , (d) the Rossby number, Ro , (e) the Zeman wavenumber, k_Ω , (f) the Kolmogorov dissipation wavenumber, k_η , and (g) anisotropy of the system A . The inset in subfigure (a) is log-log plot showing $E(t) \sim t^{-0.33}$. . .	54

- 3.2 For the rapidly rotating decaying turbulence on 512^3 grid: The top panel exhibits the isosurfaces of the magnitude of vorticity $|\omega|$ at (a) $t = 49$, (b) $t = 98$, and (c) $t = 148$. The bottom panel shows velocity vector plot superposed with the density plot for ω_z for the horizontal cross section at $z = \pi$ at (d) $t = 49$, (e) $t = 98$, and (f) $t = 148$. Note that (f) contains only one vortex that appears to be split in two due to the periodic boundary conditions. 56
- 3.3 For the rapidly rotating decaying simulation on 512^3 grid, the energy transfers $S(\mathbf{k}'|\mathbf{p}|\mathbf{q})$ for some of the dominant triads averaged over five eddy turnover time from $t = 148$ to 152. The numbers above the arrows are $S(\mathbf{k}'|\mathbf{p}|\mathbf{q}) \times 10^5$ for convenient description. The most dominant energy transfers are in the triad $[(-1, 0, 0), (1, -1, 0), (0, -1, 0)]$ 60
- 3.4 Kinetic energy flux $\Pi(k)$ and enstrophy flux $\Pi_\omega^{(2D)}(k)$ for rapidly rotating decaying turbulence. (a) $\Pi(k)$ of 3D velocity field for 512^3 (magenta) and 1024^3 (blue dashed curve) grids at $t = 4$. (b) $\Pi_\omega^{(2D)}(k)$ for the 2D cross section at $z = \pi$. Figure (b) has the same color convention as (a). (c) $\Pi(k)$ at $t = 49$ (green), and $t = 148$ (red) for the grid resolutions of 512^3 and at $t = 49$ (cyan) for 1024^3 grids. (d) $\Pi_\omega^{(2D)}(k)$ for 2D cross section at $z = \pi$. Figure (d) has the same color convention as (c). Note that $\Pi_\omega^{(2D)}(k)$ is significant, but $\Pi(k)$ is negligible. Note: The x-scales are in log. 62

LIST OF FIGURES

3.5	For the rapidly rotating decaying simulation using \mathbf{u}_\perp at $z = \pi/2, \pi, 3\pi/2$. Two-dimensional enstrophy spectrum $kE_\omega^{(2D)}(k)$ for (a) $z = \pi/2$, (b) $z = \pi$, (c) $z = 3\pi/2$ at $t = 49$ (green) and $t = 148$ (red) for 512^3 grid simulation, and at $t = 49$ (cyan) for the 1024^3 grid. The best fit curves using Equation (3.9) with parameters of Table 5.1 are shown as black dashed curves. (d,e,f) The corresponding plots of the 2D enstrophy flux $\Pi_\omega^{(2D)}(k)$ following the same color convection as above. The best fit curves however are of the form of Equation (3.10). Since $E_\omega^{(2D)}(k)$ and $\Pi_\omega^{(2D)}(k)$ of 512^3 and 1024^3 grids almost overlap on each other, we multiply $E_\omega^{(2D)}(k)$ and $\Pi_\omega^{(2D)}(k)$ of 1024^3 grid with a factor $1/100$ to differentiate the two plots.	65
3.6	For the rapidly rotating decaying turbulence: (a) Normalized 3D energy spectrum $k^3E_\perp(k)$ vs. k at $t = 49$ (green),148 (red) for 512^3 grid simulation, and at $t = 49$ (cyan) for 1024^3 grid. The best fit curves following Equation (3.24) with ϵ_ω and C of Table 5.1 are plotted as black dashed curves. (b) The corresponding plots of $k^3E(k)$ where $E(k) = E_\perp(k) + E_\parallel(k)$. Since $E(k)$ of 512^3 and 1024^3 grids almost overlap on each other, we multiply $E(k)$ of 1024^3 grid with a factor $1/100$ to differentiate the two plots.	66
4.1	Anisotropy of the forced rotating turbulent system vs. wavenumber at $t = t_f$ for grid simulation of 512^3 grid resolution (magenta) and 1024^3 grid resolution (blue).	71
4.2	Plots for (a) iso-surfaces of various magnitudes of the 3D vorticity field, and (b) the density plot for the cross-section of 2D velocity field taken at $z = \pi$. Both the plots use the 1024^3 -grid simulations data.	72
4.3	Plot of kinetic energy flux $\Pi(k)$ vs. k of the 3D velocity field at $t = t_f$ for grid resolution 512^3 (magenta) and 1024^3 grid resolution (blue). The peaks in the plots indicate the corresponding forced wavenumbers k_f	74

4.4	Plots of (a) the non-dimensionalized energy spectra, $\bar{E}(\bar{k})$, and (b) the non-dimensionalized energy flux, $\bar{\Pi}(\bar{k})$ at $t = t_f$, as generated by the simulations done with grid resolutions of 512^3 (magenta) and 1024^3 (blue) for the forced rotating turbulent fluid. The dotted lines are the fits generated in accordance with the energy spectra and the energy flux given in Eqs. (4.4)-(4.5).	76
4.5	Plots of the (anisotropic) energy spectrum, $E(k_\perp, k_\parallel)$ at $t = t_f$, as a function of (a) k_\perp for $k_\parallel = 1$, (b) k_\parallel for $k_\perp = 35$, and (c) k_\perp after the spectrum is summed over all k_\parallel . The dashed lines are the fitting lines; we have appropriately used the wavenumber range $1 \leq k_\perp, k_\parallel \leq 6$ for the 512^3 grid and $1 \leq k_\perp, k_\parallel \leq 11$ for the 1024^3 grid as the fitting ranges. As in the other plots, we have used magenta for 512^3 grid-resolution data and blue for 1024^3 grid-resolution data. Subplot (d) exhibits the plots for the (isotropic) energy spectra, $E(k)$ (magenta and blue) and $E(k_\perp)$ (red and black), as functions of k . Here, we have used additional colours—red and black—to respectively indicate the data corresponding to 512^3 grid and 1024^3 grid. The fitting ranges in subplot (d) are $1 \leq k \leq 6$ for 512^3 grid and $1 \leq k \leq 20$ for 1024^3 grid.	78
5.1	<i>Flow structure and distribution of ring energy $E^{(m,\alpha)}(k, \theta)$ in rotating turbulence.</i> The contour plot of 3D vorticity field, the ring energy spectrum, and the contour plot of ring energy spectrum are respectively shown in figures (a)-(c) at time frame $t = 0$ and in figures (d)-(f) at time frame $t = 56$ for the forced rotating turbulence with rotation rate $\Omega = 32$. Similarly, the contour plot of 3D vorticity field, the ring energy spectrum, and the contour plot of ring energy spectrum are respectively depicted in figures (g)-(i) at time frame $t = 0$ and in figures (j)-(l) at time frame $t = 4$ for the decaying rotating turbulence with rotation rate $\Omega = 16$	83

LIST OF FIGURES

5.2 *Inverse and forward cascades.* Shell-to-shell energy transfer rate T_n^m (quantified by the colourbars) for (a) decaying rotating turbulence with $\Omega = 16$ at time frame $t = 50$, and (b) forced rotating turbulence with $\Omega = 32$ at time frame $t = 56$. The subplots (c) and (d) depict the shell-to-shell energy transfers in the two non-overlapping wavenumber regions— $k < k_f$ and $k > k_f$ respectively—for the forced rotating turbulence. The forcing shell number is 24. Here m and n denote the donor and the receiver shells respectively. 85

5.3 *Conical flux is almost monotonic for the decaying rotating turbulence but distinctly non-monotonic for the forced counterpart.* Plots of normalized conical energy flux, $\Pi(\theta) / \max(|\Pi(\theta)|)$, for rapidly rotating decaying turbulence (for $\Omega = 16$ and at $t = 4$) and forced turbulence (for $\Omega = 32$ and at $t = 56$) versus polar angle in radian. The solid black curve with circles and the solid cyan curve with diamonds respectively correspond to the decaying and the forced cases. Furthermore, the blue dotted curve with solid down-triangles and blue dashed curve with up-triangles correspond to the wavenumber ranges $k > k_f$ and $k < k_f$ respectively the same forced system. 87

LIST OF FIGURES

5.4 The local energy transfer is equatorward in decaying case; and is polewards in forced case for $k < k_f$ and equatorward for $k > k_f$. The normalized ring-to-ring energy transfer, $\bar{T}_{(n,\alpha)}^{(m,\beta)}$, has been quantified by the colourbars. The x -axis represents sector index, α , of receiver ring and the y -axis represents sector index, β , of the donor ring. The upper row exhibits the transfer among various rings inside (a) Shell(10) for the decaying rotating turbulence, (b) Shell(10) for the forced rotating turbulence, and (c) Shell(16) for the forced rotating turbulence. Shell(12) corresponds to the forcing scale. The lower panel illustrates the ring-to-ring energy transfer in (d) the decaying rotating turbulence from Shell(10) to Shell(9), (e) the forced rotating turbulence from Shell(10) to Shell(9), and (f) the forced rotating turbulence from Shell(16) to Shell(15). 89

5.5 Schematic diagram for the anisotropic energy transfer in (a) decaying, and (b) forced rotating turbulence. 90

A.1 For rapidly rotating turbulence, the density plots of ω_z at $z = \pi$ in boxes of sizes $(2\pi)^3$ (a) and $(4\pi)^3$ (b). For initial condition, we take the 512^2 data at $t = 49$ of Fig. 3.2. Clearly, the size of the vortex in $(4\pi)^3$ box is twice that of $(2\pi)^3$ box. (c) Plots of the time series of integral length scales L in $(2\pi)^3$ (green curve) and $(4\pi)^3$ (blue curve). Here $L_{4\pi} \approx 2L_{2\pi}$. 100

A.2 (a) For the 2D velocity field $\mathbf{u}(x, y) = \hat{x} \sin y + \hat{y} \sin x$ that corresponds to the Fourier modes $(1, 0, 0)$ and $(0, 1, 1)$, the vector plot of the velocity field superposed with the density plot of the vorticity field ω_z . (b) For the rotating simulation of Appendix A.1, time series of the energies of the modes $(1, 0, 0)$, $(0, 1, 0)$, $(1, 1, 0)$, $(-1, 1, 0)$ and the total energy E_T . . . 101

A.3 Plot of $E(k)$ for the 3D velocity field of 1024^3 grid along with the predictions of our model and that of Pao. This plot corresponds to the green curve of Figure 3.6. 102

LIST OF FIGURES

A.4 Plot of the 2D enstrophy flux, $\Pi_{\omega}^{(2D)}(k)$, for the 2D velocity field on the horizontal cross-section, $z = \pi$, at $t = t_f$ for the grid-resolutions 512^3 (magenta) and 1024^3 (blue). The inset highlights the inverse cascade of the flux. The peaks in the plots indicate the corresponding forced wavenumbers k_f 103

A.5 Plot of the 3D enstrophy flux, $\Pi_{\omega}(k)$, for the 3D velocity field at $t = t_f$ for the grid-resolutions 512^3 . The peaks in the plots indicate the corresponding forced wavenumbers k_f 104

A.6 Plots of the (anisotropic) energy spectrum, $E(k_{\perp}, k_{\parallel})$ at $t = t_f$, as a function of k_{\parallel} with different k_{\perp} for (a) 512^3 grid resolution and (b) 1024^3 grid resolution. The fitting exponent (m) in $E(k_{\perp}, k_{\parallel}) \sim k_{\parallel}^{-m}$ has been calculated in the wavenumber range $1 \leq k_{\parallel} \leq 6$ for the 512^3 grid resolution and $1 \leq k_{\parallel} \leq 11$ for the 1024^3 grid resolution is shown in the legends. . . 105

A.7 The plots show the time evolutions of (a) the integral length scale, L , (b) rms velocity of the field, u_{rms} , and (c) the Reynolds numbers— Re_{box} (solid red curve) and Re_L (solid blue curve) in decaying rotating turbulence. 106

A.8 Plot of the anisotropic parameter of system as a function of wavenumber k for forced rotating turbulence at time frame $t = 56$ 107

A.9 Plots for the time evolution of (a) total energy, (b) the kinetic energy spectrum as a function of k , and (c) kinetic energy flux as a function of k for forced rotating turbulence. 108

A.10 Plots for total kinetic energy spectrum, $E(k)$, as a function of wavenumber k (dashed red curve), $E(k_{\perp})$ as function of k_{\perp} (solid green curve), and $E(k_{\parallel})$ as a function of k_{\parallel} (solid blue curve) for forced rotating turbulence at time frame $t = 56$ 109

LIST OF FIGURES

A.11 Plots for anisotropy A of decaying rotating turbulence as a function of wavenumber k for different time frames $t = 49$ (red solid curve), $t = 98$ (blue solid curve), and $t = 148$ (red solid curve) 110

List of Tables

3.1	Parameters of the direct numerical simulations (DNS): List of total energy E ; integral length scale L ; Reynolds number Re ; Rossby number Ro ; Zeman wavenumber k_Ω ; Kolmogorov dissipation wavenumber k_η ; and anisotropy ratio A at $t = 49, 148$ for 512^3 grids, and at $t = 49$ for 1024^3 grids.	53
3.2	For rapidly rotating turbulence on 512^3 grid at $t = 4, 49, 148$, the energy contents of the dominant modes as percentage of the total energy. Note that $\mathbf{u}(-k_x, -k_y, 0)$, not listed in the table, has the same energy contents as that of $\mathbf{u}(k_x, k_y, 0)$. In the table, $E_{\text{mode}} = u(\mathbf{k}) ^2/2$. For the modes $(0, 1, 0)$ and $(1, 0, 0)$, E_{mode}/E increases with time indicating strengthening of the vortical structures with time.	58
3.3	For the rapidly rotating decaying turbulence, we take the instantaneous 2D velocity field on the horizontal cross sections at $z = \pi/2, \pi$, and $3\pi/2$. List of the enstrophy dissipation rate, ϵ_ω , the enstrophy dissipation wavenumber, k_d , and constant C . These parameters are listed in the table at time $t = 49$ for 512^3 and 1024^3 , and $t = 148$ for 512^3	64

4.1	Parameters of the simulation: the grid-resolution N , the forcing wavenumber band k_f , rotation rate Ω , kinematic viscosity ν , final eddy turnover time t_f , energy supply rate ϵ , Rossby number $\text{Ro}_L := u_{\text{rms}}/2\Omega L$, Reynolds number $\text{Re}_L := u_{\text{rms}}L/\nu$, Zeman wavenumber $k_\Omega, k_{\text{max}}\eta$, and the Kolmogorov dissipation wavenumber k_η . Here, L is integral length scale and it computed by Eq. 1.36.	70
4.2	Percentage energy distribution among dominant modes at $t = 56$ and $t = 3$ for the grid resolution of 512^3 and 1024^3 at the rotation rate $\Omega = 32$ respectively. In table E_{mode} is defined as $E_{\text{mode}} = u(\mathbf{k}) ^2/2$, and E is the total energy of the system at $t = 3, 56$	73
5.1	Parameters of the simulation: The values of the forcing wavenumber band, k_f ; the rotation rate, Ω ; the kinematic viscosity, ν ; the final simulation run time, t_f ; the Rossby number, $\text{Ro}_L := u_{\text{rms}}/2\Omega L$; the Reynolds number, $\text{Re}_L := u_{\text{rms}}L/\nu$; the Zeman wavenumber [6] $k_\Omega := (\Omega^3/\epsilon)^{1/2}$; and the Kolmogorov dissipation wavenumber, $k_\eta := (\epsilon/\nu^3)^{1/4}$ are given in the table. Here, u_{rms} is the r.m.s. velocity of the field and L is the integral length scale. (See Appendix A for details.). In case of forced rotating turbulence the system is forced in the wavenumber band $k_f \in (40, 41)$. . .	82

Chapter 1

Introduction

Turbulence is the most important unsolved problem of classical physics.

– Richard Feynman

In this chapter, we discuss the occurrence of the rotating turbulence in different flows. Afterward, we discuss the governing equations and important parameters of the flows. We also present the literature survey on the rotating turbulence, and finally, we outline the contents of the thesis.

1.1 Introduction

Turbulence is an omnipresent phenomenon observed in nature. It is observed at all scales, from a cup of coffee being stirred to intracluster medium in galaxy cluster. Turbulence occurs in engineering flows like air flowing past the boundary of an aircraft, fluid flows around automobiles, submarines, ships, etc. The flows in geophysics like water currents inside oceans, gulf streams, motion of clouds, atmospheric circulation, etc. are all turbulent. We also encounter turbulence in and around our bodies like blood flowing through the veins, air at the nose during exhalation, etc. Although turbulence is observed ubiquitously in nature, it is hard to precisely define it.

Turbulence is characterized by randomness in velocity and vorticity fields, high

diffusivity, nonlinearity, etc. in the flow. Rotation makes turbulence even more complex by introducing new time and length scales in the system. The flows observed in nature, whether it is astrophysical flow or geophysical flow, are rotating about some axis. Along with rotation, the astrophysical flows are also generally turbulent; for example, accretion disk [7], zonal atmospheric flows on Jupiter [8], etc. The rotation also affects the dynamics of geophysical flows. The conducting fluids inside the core of the earth produce geomagnetic fields, and rotation of the earth helps in sustaining it [9]. Atmospheric and oceanic flows are affected by the rotation of the earth, for example, the generation of cyclones and anti-cyclones. Winds blowing over the ocean creates instability at the surface of contact resulting in turbulence. The Coriolis force due to rotation of the earth converts this turbulence into cyclones in the Northern hemisphere and anti-cyclones in the Southern hemisphere [10].

The Reynolds number (a non-dimensional number) is an important parameter in the study of turbulence in fluid flows. It is the ratio of the inertial force to the viscous force of the flow. Apart from the Reynolds number in 3D turbulence, rotation introduces a new non-dimensional number called Rossby number (Ro). The Rossby number is the ratio of the inertial force and the Coriolis force. Low Ro corresponds to the high rotation rate. The Rossby number for the solar dynamo should be $\mathcal{O}(10^{-2})$, whereas for the geodynamo of the Earth is $\mathcal{O}(10^{-6})$. The Rossby number for the Earth and the Mars atmosphere is $\mathcal{O}(10^{-1})$ and for the Venus 10 – 50. The tornadoes have Rossby number of the order of 10^3 , and large ocean flows have $Ro \sim 10^{-2}$.

Engineers face turbulence while designing automobiles, airplanes, ships, submarines, compressors, turbines, etc. In addition, rotation in turbulence during the design of the aforementioned structures makes the job of engineers even more difficult. For example, one can observe rotating turbulent flow near the blade of the turbine, which occurs due to shear stress between the blade and the fluid flow. The cyclone separator is another example where rotation is used to separate heavy and light particles from the flow.

The ubiquitous and challenging nature of turbulence makes this field very interesting for scientists and engineers. Turbulence is studied numerically, analytically, and experimentally. In this thesis, we use numerical simulations to study the effects of rotation on the statistical properties like the kinetic energy spectrum and the kinetic energy in the flow numerically.

1.1.1 Experimental setups of rotating turbulence

In this section, we discuss some experimental techniques of studying rotating turbulence in the laboratory. Yarom et al. [1] have investigated the statistical behavior like the kinetic energy flux of the forced rotating turbulence. In their study, they have reported an inverse cascade of kinetic energy—transfer of energy from larger wavenumber to smaller wavenumber. They have studied the flow in a cylindrical geometry. The experimental set-up has a rotating plexiglass cylinder of 90 cm height and 80 cm diameter (see Fig. 1.1). The cylinder is filled with water, and white polyamide of size $50\mu\text{m}$ is used as particle tracers. The cylinder is closed with a transparent lid. The laser is used to illuminate the cross-section of the cylinder at a specific height. A co-rotating camera at the top captures the light reflected by the tracer particles from a specific height. Particle image velocimetry (PIV) is used to obtain the velocity field $v(x, y)$ from the photos captured by the co-rotating camera. Energy is injected into the cylinder by the pump, which circulates water through the hexagonal grid from the bottom. The hexagonal grid has a 248 small (0.8 mm) outlet and 73 larger (6 mm) inlets. This energy injected from the bottom hexagonal grid generates small scale 3D turbulence.

After an interval of 5s, the inertial wave propagates through the entire volume of the tank, and the system comes into statistical steady-state in 100s. The flow rate (Q) is set in the range $Q = 0.7 - 1.5$ l/s, and the rotation rate is in the range $\Omega = 9.4 - 12.6$ rads/sec. This flow and the rotation rate corresponds to the Reynolds number $\text{Re} \sim 10^3 - 10^4$ and the Rossby number $\text{Ro} \sim 10^{-2}$, respectively. The PIV measurements are taken at a height $h = 68$ cm above the injection pump. In this experimental setup, Yarom et al. [1] investigated the behavior of the kinetic energy spectrum of the horizontal velocity field at scales larger than the energy injection scale. Their study showed kinetic energy spectrum in rotating turbulence is similar to the kinetic energy spectrum observed in 2D turbulence in inverse cascade region.

Apart from the experimental setup mentioned above, there are other experimental setups in cylindrical geometry to study the rotating turbulence [11–18]. One such example is the case where turbulence in the system is generated by oscillating a grid along the axis of rotation [19].

The rotating turbulence has also been studied Experimentally [20, 21] in a cubical geometry [2]. One such study for the decaying rotating turbulence has performed by Lambriben et al. [22]. In their study, they have found that the rotation induced an

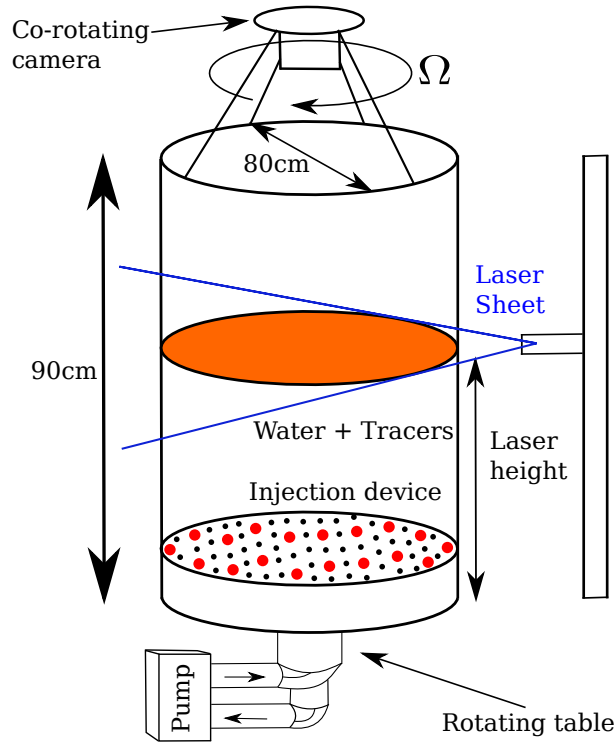


FIGURE 1.1: A schematic diagram of an experimental setup [1] of rotating turbulence: A Plexiglas cylindrical water tank is kept on a rotating platform and energy is injected from the bottom. A horizontal laser sheet is used to illuminate a horizontal cross-sectional area, and a co-rotating camera on the top..

anisotropy in energy transfer which leads to anisotropy in the energy spectrum. The setup consists of a cubical box of box-size $(60\text{cm})^3$ with water filled up to a height of 52cm (see Fig. 1.2). This box is kept on a rotating table whose diameter is 32m. The turntable is rotating with angular velocity $\Omega = 0.84 \text{ rad s}^{-1}$ (8 rotation per minute). The system is rotated for half an hour before initiating the experiment in order to dampen the spin-up circulation. As a result, the system behaves like a rotating solid body. A horizontal cover is placed at the height of $H = 49\text{cm}$ to close the setup. A square grid is used to generate turbulence in the system, which consists of 8mm thick square bars with a mesh size of $M = 40\text{mm}$. The solid-to-total area ratio is 0.36, and it is situated 3mm away from the side walls. Half meshes are placed along the four sides of the grid to optimize the homogeneity of the flows. The grid is rapidly towed from bottom to top with the help of four servo-controlled brush-less motors (which provides a vertical velocity of $V_g = 0.70\text{ms}^{-1}$) till it reaches a height of 46cm. The grid then comes to a stop, and the turbulence in the system decays. The Reynolds number

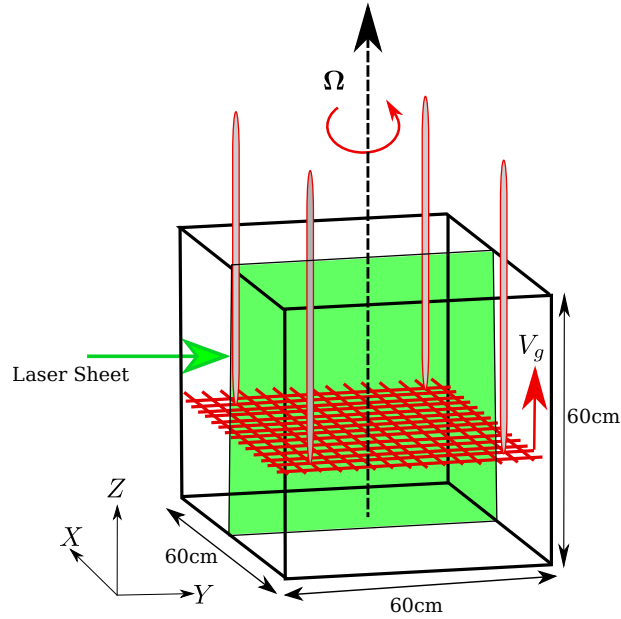


FIGURE 1.2: A schematic diagram of an experimental setup [2] of rotating turbulence: A cubical water tank is kept on a rotating and the turbulence in the system is generated by towing a grid with velocity V_g .

and the Rossby number of the flow just near the grid are 28000 and 10.4 respectively.

The flow is seeded by tracer particle of size $10\mu\text{m}$. These tracer particles are illuminated by a co-rotating laser sheet which passes through the center of the cubic tank (in Fig. 1.2, the green vertical plane). A two-dimensional PIV system measures the velocity of the tracer particles in the illuminated plane. The illuminated plane with area $60 \times 46 \text{ cm}^2$ are imaged through double-buffer high-resolution camera resolution 2048×2048 pixels. The camera is also rotating with the table, and has the same angular velocity. The camera is kept perpendicular to the illuminated plane. The properties of inertial modes generated by rotation in decaying rotating turbulence are investigated using the experimental setup described above by Lamriben et al. [2]. They have reported a significant amount of energy (typically 50%) is confined in the resonant inertial modes and the energy confined in the inertial modes are reduced by adding a set of inner tanks attached to the grid.

1.2 Governing equations

Turbulence is also studied using numerical simulations. In the numerical simulation, the governing equations of the flow are solved on the numerical grid points. There are various ways to solve the governing equation like large eddy simulation, direct numerical simulation, Reynolds average Navier–Stokes equation scheme, etc. We now discuss the governing equation and important parameters of the flow.

1.2.1 Governing equations in rotating frame of reference

In rotating frame of reference, the Navier–Stokes (NS) equation for an incompressible flow in the absence of body force is given by [3, 9, 23, 24],

$$\frac{\partial \mathbf{u}}{\partial t} + (\mathbf{u} \cdot \nabla) \mathbf{u} = -\nabla \left(\frac{p}{\rho} \right) - 2\boldsymbol{\Omega} \times \mathbf{u} + \nu \nabla^2 \mathbf{u}. \quad (1.1)$$

Here, $\mathbf{u} = (u_x, u_y, u_z)$ is the velocity field, p is the modified pressure which includes the centrifugal term, $2\boldsymbol{\Omega} \times \mathbf{u}$ is the Coriolis force, ρ is the density of the flow, ν is the kinematic viscosity, and $\nu \nabla^2 \mathbf{u}$ is the dissipative term in the system. The system is assumed to be incompressible i.e. $\nabla \cdot \mathbf{u} = 0$.

In the presence of an external forcing term (\mathbf{f}), NS equation becomes,

$$\frac{\partial \mathbf{u}}{\partial t} + (\mathbf{u} \cdot \nabla) \mathbf{u} = -\nabla \left(\frac{p}{\rho} \right) - 2\boldsymbol{\Omega} \times \mathbf{u} + \nu \nabla^2 \mathbf{u} + \mathbf{f}. \quad (1.2)$$

In our numerical simulations, we use the non-dimensional form of the NS equation. We use the following non-dimensional variables [3];

$$x' = x/L, \quad \mathbf{u}' = \mathbf{u}/U, \quad t' = t/(L/U), \quad \nu' = \nu/(UL), \quad (1.3)$$

$$\nabla' = L\nabla, \quad p' = p/(\rho U^2), \quad \mathbf{f}' = L\mathbf{f}/U^2, \quad \boldsymbol{\Omega}' = \boldsymbol{\Omega}L/U, \quad (1.4)$$

where L is the system size and U is the large scale velocity field. We have taken the rotation direction along the z-axis in our study.

Using the above non-dimensional variables, we derive the non-dimensional form

of the NS equation in the rotating frame;

$$\frac{\partial \mathbf{u}'}{\partial t'} + (\mathbf{u}' \cdot \nabla') \mathbf{u}' = -\nabla' p' - \frac{1}{\text{Ro}} (\hat{\mathbf{z}} \times \mathbf{u}') + \frac{1}{\text{Re}} \nabla'^2 \mathbf{u}' + \mathbf{f}'. \quad (1.5)$$

We use $\text{Ro} = 1/2\Omega'$ and $\text{Re} = 1/\nu'$, and drop primes for notational convenience. Therefore, the non-dimensionalized NS equation is

$$\frac{\partial \mathbf{u}}{\partial t} + (\mathbf{u} \cdot \nabla) \mathbf{u} = -\nabla p - 2(\boldsymbol{\Omega} \times \mathbf{u}) + \nu \nabla^2 \mathbf{u} + \mathbf{f}. \quad (1.6)$$

with the incompressibility condition,

$$\nabla \cdot \mathbf{u} = 0. \quad (1.7)$$

The dynamics of the system depends on the relative strength of the terms in Eq. 1.1. The relative strength of these terms are represented by non-dimensional numbers, where the Reynolds number, Re , is defined as,

$$\text{Re} = \frac{(\mathbf{u} \cdot \nabla \mathbf{u})}{\nu \nabla^2 \mathbf{u}} \sim \frac{UL}{\nu}, \quad (1.8)$$

and Rossby number, Ro , is defined as,

$$\text{Ro} = \frac{(\mathbf{u} \cdot \nabla \mathbf{u})}{\boldsymbol{\Omega} \times \mathbf{u}} \sim \frac{U}{\Omega L}, \quad (1.9)$$

The smallest length scale of the system is the Kolmogorov micro-scale, from where the dissipation term of the system becomes dominant over the other terms in the governing equation of the flow. The Kolmogorov micro-scale η is estimated by comparing the inertial term and the dissipation term i.e. $(\mathbf{u} \cdot \nabla) \mathbf{u} = \nu \nabla^2 \mathbf{u}$ such that,

$$\eta \sim \left(\frac{\nu^3}{\epsilon} \right)^{1/4}, \quad (1.10)$$

where $\epsilon = \nu \int \nabla^2 \mathbf{u} d\mathbf{r}$ is the energy dissipation rate.

The circulation of the velocity field is one of the characteristics of turbulence. This circulation is measured in term of vorticity field $\boldsymbol{\omega}$, which is defined as,

$$\boldsymbol{\omega} = \nabla \times \mathbf{u}. \quad (1.11)$$

Taking curl of Eq. 1.6, we get the time evolution equation of the vorticity field for constant rotation rate along z- direction:

$$\frac{\partial \boldsymbol{\omega}}{\partial t} + (\mathbf{u} \cdot \nabla) \boldsymbol{\omega} = 2(\boldsymbol{\Omega} \cdot \nabla) \mathbf{u} + (\boldsymbol{\omega} \cdot \nabla) \mathbf{u} + \nu \nabla^2 \boldsymbol{\omega} + \nabla \times \mathbf{f}. \quad (1.12)$$

The following quadratic quantities in turbulent flows, constructed by the velocity and the vorticity fields are of great importance [3,4]:

$$E(t) = \frac{1}{2} \int [\mathbf{u}(\mathbf{r}, t)]^2 d\mathbf{r}, \quad (1.13)$$

$$H(t) = \frac{1}{2} \int [\mathbf{u}(\mathbf{r}, t) \cdot \boldsymbol{\omega}(\mathbf{r}, t)] d\mathbf{r}, \quad (1.14)$$

$$E_\omega(t) = \frac{1}{2} \int [\boldsymbol{\omega}(\mathbf{r}, t)]^2 d\mathbf{r}. \quad (1.15)$$

In absence of viscosity and external forcing, in 3D turbulence, total kinetic energy ($E(t)$), and total kinetic helicity ($H(t)$) are invariant of motion. However, in two-dimensional turbulence the total kinetic energy ($E(t)$) and the total enstrophy ($E_\omega(t)$) are the invariant quantities.

Since turbulence is a multi-scale phenomenon, the spectral (Fourier) method is one of the best approaches to explore the behavior of the system at different scales. In a cubic periodic box of box-size $L_x \times L_y \times L_z$, the velocity field in Fourier space is represented by [25–27],

$$\mathbf{u}(\mathbf{r}, t) = \sum_{\mathbf{k}} \hat{\mathbf{u}}(\mathbf{k}, t) \exp(j\mathbf{k} \cdot \mathbf{r}), \quad (1.16)$$

where $\mathbf{u}(\mathbf{r}, t)$ is the velocity field in real space and $\hat{\mathbf{u}}(\mathbf{k}, t)$ is the velocity field of wavenumber mode \mathbf{k} in the Fourier space. The wave vectors live in the cubic periodic box is bounded in Fourier domain with $k_x = \frac{2l\pi}{L_x}$, $k_y = \frac{2m\pi}{L_y}$, and $k_z = \frac{2n\pi}{L_z}$, where l, m, n are integers varying from $-\infty$ to ∞ .

The inverse Fourier transform is defined as,

$$\mathbf{u}(\mathbf{k}, t) = \frac{1}{L_x L_y L_z} \int [\mathbf{u}(\mathbf{r}, t) \exp(-j\mathbf{k} \cdot \mathbf{r})] d\mathbf{r}. \quad (1.17)$$

Using Eq. 1.16, the NS equation for incompressible flow in a rotating frame of reference in Fourier space takes the form [4,25,26],

$$\frac{d\hat{\mathbf{u}}(\mathbf{k}, t)}{dt} = -j\mathbf{k}\hat{p}(\mathbf{k}, t) - \hat{\mathbf{N}}_u(\mathbf{k}, t) - 2\boldsymbol{\Omega} \times \hat{\mathbf{u}}(\mathbf{k}, t) - \nu k^2 \hat{\mathbf{u}}(\mathbf{k}, t) + \hat{\mathbf{f}}(\mathbf{k}, t), \quad (1.18)$$

$$\mathbf{k} \cdot \hat{\mathbf{u}}(\mathbf{k}) = 0. \quad (1.19)$$

The nonlinear term $\hat{\mathbf{N}}_u(\mathbf{k}, t)$ in Eq. 1.18 is defined as,

$$\hat{\mathbf{N}}_u(\mathbf{k}) = j \sum_{\mathbf{p}} [\mathbf{k} \cdot \hat{\mathbf{u}}(\mathbf{q})] \hat{\mathbf{u}}(\mathbf{p}). \quad (1.20)$$

where $\mathbf{q} = \mathbf{k} - \mathbf{p}$ and the summation is non-zero only for triad i.e. $\mathbf{k} = \mathbf{p} + \mathbf{q}$.

Similarly, the Fourier transform of the total vorticity is defined as,

$$\boldsymbol{\omega}(\mathbf{k}, t) = j\mathbf{k} \times \hat{\mathbf{u}}(\mathbf{k}, t). \quad (1.21)$$

Taking curl of Eq. 1.18, we obtain the following dynamical equation of the vorticity field in the Fourier space [3],

$$\frac{d\hat{\boldsymbol{\omega}}(\mathbf{k}, t)}{dt} + \hat{\mathbf{N}}_\omega(\mathbf{k}, t) = -2j\mathbf{k} \times [\boldsymbol{\Omega}(\mathbf{k}, t) \times \hat{\mathbf{u}}(\mathbf{k}, t)] - \nu k^2 \hat{\boldsymbol{\omega}}(\mathbf{k}, t) + \hat{\mathbf{F}}_\omega(\mathbf{k}, t), \quad (1.22)$$

$$\hat{\mathbf{N}}_\omega(\mathbf{k}, t) = j \sum_{\mathbf{p}} [(\mathbf{k} \cdot \hat{\mathbf{u}}(\mathbf{q}, t)) \hat{\boldsymbol{\omega}}(\mathbf{p}, t) - (\mathbf{k} \cdot \hat{\boldsymbol{\omega}}(\mathbf{q}, t)) \hat{\mathbf{u}}(\mathbf{p}, t)], \quad (1.23)$$

$$\hat{\mathbf{F}}_\omega(\mathbf{k}) = j\mathbf{k} \times \hat{\mathbf{f}}(\mathbf{k}). \quad (1.24)$$

The energy evolution equation of a turbulent flow in the Fourier space is obtained by taking the scalar product of Eq. 1.18 with $\hat{\mathbf{u}}^*(\mathbf{k}, t)$, and adding the resultant equation with its complex conjugate. The energy equation in the Fourier space is [3],

$$\frac{\partial E(\mathbf{k}, t)}{\partial t} = T(\mathbf{k}, t) - D(\mathbf{k}, t) + F(\mathbf{k}, t), \quad (1.25)$$

The terms $E(\mathbf{k}, t) = |\hat{\mathbf{u}}(\mathbf{k}, t)|^2/2$, $T(\mathbf{k}, t)$, $D(\mathbf{k}, t) = 2\nu k^2 E(\mathbf{k}, t)$, and $F(\mathbf{k}, t) = \Re \left[\hat{\mathbf{f}}(\mathbf{k}, t) \cdot \hat{\mathbf{u}}^*(\mathbf{k}, t) \right]$ are, respectively, the modal kinetic energy, the rate of energy transfer to the Fourier mode \mathbf{k} due to nonlinear interactions to be defined below in Eq. 1.26, the energy dissipation rate, and the kinetic energy supply rate to the mode \mathbf{k} by external forcing. Here \Re stands for the real part of a complex number.

The energy transfer rate $T(\mathbf{k}, t)$ is defined as [28];

$$T(\mathbf{k}, t) = \sum_{\mathbf{p}} S(\mathbf{k}|\mathbf{p}|\mathbf{q}) = \sum_{\mathbf{p}} \Im[(\mathbf{k} \cdot \mathbf{u}(\mathbf{q}, t))(\mathbf{u}(\mathbf{p}, t) \cdot \mathbf{u}^*(\mathbf{k}, t))]. \quad (1.26)$$

Here, \Im stands for the imaginary part of the argument and $\mathbf{q} = \mathbf{k} - \mathbf{p}$. $S(\mathbf{k}|\mathbf{p}|\mathbf{q})$ represents the rate of transfer of energy from the velocity mode $\mathbf{u}(\mathbf{p})$ to the velocity mode $\mathbf{u}(\mathbf{k})$, where the velocity mode $\mathbf{u}(\mathbf{q})$ acts as mediator in a triad which satisfies the condition $\mathbf{k} + \mathbf{p} + \mathbf{q} = 0$.

The rate of change of kinetic energy inside a sphere of radius k_0 (see Fig. 1.3) is given by [3];

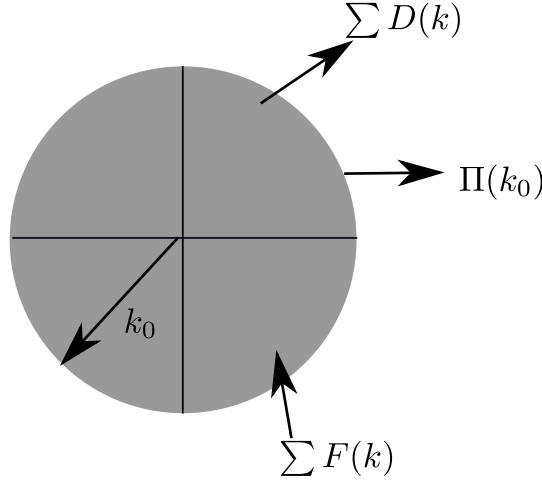


FIGURE 1.3: Schematic diagram shows how the energy in a sphere is affected by other terms in the energy evolution equation. This figure is adapted from a figure from Ref. [3].

$$\frac{\partial}{\partial t} \sum_{|\mathbf{k}| \leq k_0} E(\mathbf{k}) = \sum_{|\mathbf{k}| \leq k_0} T(\mathbf{k}) + \sum_{|\mathbf{k}| \leq k_0} F(\mathbf{k}) - \sum_{|\mathbf{k}| \leq k_0} D(\mathbf{k}), \quad (1.27)$$

In Fig. 1.3, we see that $\sum_{|\mathbf{k}| \leq k_0} D(\mathbf{k})$ dissipate the energy, $\sum_{|\mathbf{k}| \leq k_0} F(\mathbf{k})$ and $\sum_{|\mathbf{k}| \leq k_0} T(\mathbf{k})$ enhance or dissipate the energy depending on their sign. The rate of transfer of energy from the modes inside the sphere of radius k_0 to the modes outside the sphere due to nonlinear interaction is called kinetic energy flux, $\Pi(k_0)$. The energy lost by the modes inside the sphere due to nonlinear interaction equals to the energy gain by the modes

outside the sphere. This transfer of energy is defined as [27,29,30],

$$\Pi(k_0) = - \sum_{|\mathbf{k}| \leq k_0} T(\mathbf{k}). \quad (1.28)$$

Now, the evolution of energy for the modes lying between the spheres of radii k and $k + dk$ (see Fig. 1.4) is given by [3],

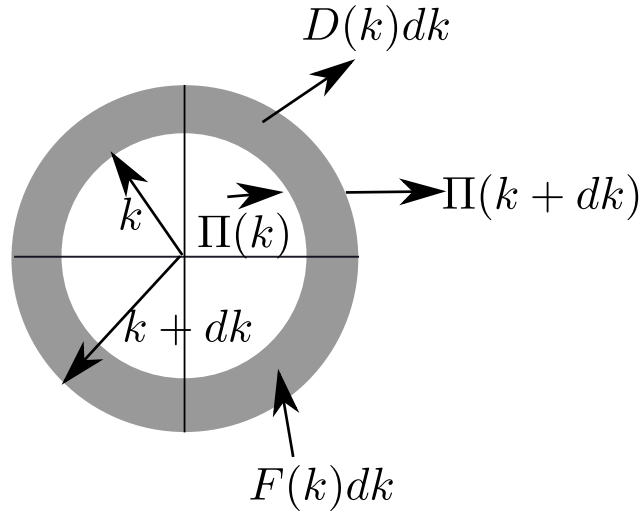


FIGURE 1.4: A schematic diagram [3] to shows the rate of transfer of energy from a shell.

$$\begin{aligned} \frac{\partial}{\partial t} \sum_{k < k' \leq k+dk} E(\mathbf{k}') &= \sum_{k < k' \leq k+dk} T(\mathbf{k}') + \sum_{k < k' \leq k+dk} F(\mathbf{k}') - \sum_{k < k' \leq k+dk} D(\mathbf{k}'), \\ &= [-\Pi(k + dk) + \Pi(k)] + \sum_{k < k' \leq k+dk} F(\mathbf{k}') - \sum_{k < k' \leq k+dk} D(\mathbf{k}'). \end{aligned} \quad (1.29)$$

In the limit $dk \rightarrow 0$, the above equation becomes,

$$\frac{\partial}{\partial t} E(k) = - \frac{\partial \Pi(k)}{\partial k} + F(k) - D(k), \quad (1.30)$$

where

$$F(k)dk = \sum_{k < |\mathbf{k}'| \leq k+dk} \text{Re} \left[F(\mathbf{k}') \cdot \mathbf{u}'(\mathbf{k}') \right], \quad (1.31)$$

$$D(k)dk = 2\nu \sum_{k < |\mathbf{k}'| \leq k+dk} k'^2 E(\mathbf{k}'). \quad (1.32)$$

In steady state, $\partial E(k)/\partial t = 0$, Eq. 1.30 becomes,

$$\frac{\partial \Pi(k)}{\partial k} = F(k) - D(k). \quad (1.33)$$

The above equation is for the variable energy flux. Away from the forcing (where i.e. $F(k) \sim 0$) scale Eq. 1.33 becomes [31–33],

$$\frac{\partial \Pi(k)}{\partial k} \equiv -D(k) = -2\nu k^2 E(k).. \quad (1.34)$$

In our analysis, we use the above Eq. 1.34 as an expression for the variable energy flux, away from the forcing scale. For the case of homogeneous isotropic three-dimensional turbulence, one can use the exact relation due to Von Karman and Howarth that gives an expression for the energy flux for 3D homogeneous and isotropic turbulence.

1.3 Two-dimensionalisation through rotation

In the rotating frame of reference, the flow is affected by the Coriolis and the centrifugal forces. While the centrifugal force term may be absorbed into the pressure gradient term of the NS equation, the Coriolis force—which is perpendicular to the direction of rotation—tends to make the flow quasi-two-dimensional (2D). The Taylor–Proudman theorem [24] predicts the formation of the Taylor columns and emergence of quasi 2D behavior. Note, however, that the Taylor–Proudman theorem is applicable in the linear limit of rapidly rotating steady flow. The quasi-2D behavior of the turbulent rotating fluid is however more subtle, and its defining signatures are still not completely understood [34–37]

Before discussing the statistical properties of rotating turbulence, it is useful, for the sake of comparison, to briefly discuss the features of two-dimensional and three-dimensional turbulence. In turbulence, dynamics occur at every scales. The most im-

portant length scales of turbulence are the forcing scale, where the energy is injected in the system, and the dissipation scale, where the energy predominantly dissipates into heat. The dissipation scale of the system is called the Kolmogorov length scale, and it is given by [38],

$$\eta = \left(\frac{\nu^3}{\epsilon} \right)^{1/4}, \quad (1.35)$$

where $\epsilon = \nu \int \nabla^2 \mathbf{u} d\mathbf{r}$ is the energy dissipation rate in the 3D turbulent flow. The Kolmogorov length scale is the size of the smallest surrounding eddy in the system, and the eddies smaller than this scale dissipate into heat (the corresponding length scale in Fourier space is $k_\eta = (\epsilon/\nu^3)^{1/4}$). Other than the forcing length scale and the dissipation scale, there is another length scale i.e., the integral length scale in the turbulent flow. The integral length L scale is the largest size of the eddy in the system. The integral length scale is defined as [39],

$$L = 2\pi \frac{\int_0^{k_{max}} E(k) k^{-1} dk}{\int_0^{k_{max}} E(k) dk}. \quad (1.36)$$

where k_{max} is the maximum wavenumber available in the system.

In 1941 Kolmogorov [40] proposed a model for the kinetic energy spectrum of homogeneous and isotropic 3D turbulence. According to his model, the kinetic energy spectrum scales as $E(k) \sim k^{-5/3}$ in the inertial range. The inertial range consists of the scales (l) lying between forcing scale and Kolmogorov dissipation scale such that, $l_f \gg l \gg \eta$, where l_f is the forcing scale. In the inertial range, the energy of the system only depends on ϵ , the energy dissipation rate, and l , the length scale [40]. From the dimensional analysis, the form of kinetic energy spectrum [4, 41],

$$E(k) = K_{K_0} \epsilon^{2/3} k^{-5/3}, \quad (1.37)$$

where K_{K_0} is the Kolmogorov constant. Analytical studies show that the Kolmogorov constant depends on the details of the flow, and hence it is not universal [42, 43]. Verma and Bhattacharjee [44] reported the Kolmogorov constant as 1.47 for the fluid turbulence and 3.55 in the fully magnetic limit (where the kinetic energy becomes zero). The study by Sreenivasan [45] based on experimental data showed the Kolmogorov constant to be universal and independent of the nature of flow for the high microscale

Reynolds number. But the result was for one-dimensional energy spectrum only. However, in the numerical studies (from 512^3 to 4096^3 grid resolutions) on the universality of Kolmogorov constant [46–48] reported that the value of the Kolmogorov constant varies from 1.58 to 1.68. The behavior of the kinetic energy spectrum is shown in Fig. 1.5. The Kolmogorov spectrum is quite universal and observed in a plethora of other realistic settings, e.g., shear flows [49], buoyancy-driven systems [27, 50], and jet flows [51]. In viscoelastic fluids [52], the scaling of kinetic energy approaches the Kolmogorov scaling, i.e. $k^{-5/3}$ (from steep power-law scaling) for large Deborah numbers while steepening of the kinetic energy spectrum (approaching towards k^{-3}) is observed for low to moderate Deborah number, in the DNS.

In passing, it is of importance to remark on the energy spectrum in the far dissipation range. Kolmogorov’s first universality assumption [38] on small-scale statistical properties of turbulence with very high Reynolds numbers implies, based on dimensional arguments, the following form of the kinetic energy spectrum at large wavenumbers:

$$E(k) = \epsilon^{2/3} k^{-5/3} F(\eta k). \quad (1.38)$$

The nondimensional functional argument of $F(\eta k)$ makes the function non-dimensional. The determination of the functional form of $F(\eta k)$ has been attempted in several early studies, but von Neuman’s remark on the behaviour of (the Fourier transform of) an analytic function at high wavenumbers is particularly interesting and relevant. He inferred exponential fall-off of the Fourier transform of an analytic function at high wavenumbers from the position of singularity in the complex space nearest to the real domain. For details, one may refer to von Neuman [53], and Frisch and Morf [38, 54]. The conjectured boundedness of the solution of the three-dimensional Navier–Stokes equation with positive viscosity implies that the solution (velocity) is analytic. This suggests, based on von Neuman’s remark, that the behaviour of $F(\eta k)$ at high k should be exponential fall-off instead of the rapid algebraic fall-off.

Furthermore, Pope has proposed a model [41] of the energy spectrum for the full range of wavenumbers is given by,

$$E(k) = K_{K_0} \epsilon^{2/3} k^{-5/3} f_L(kL) f_\eta(k\eta), \quad (1.39)$$

where f_L and f_η are the non-dimensional functions. The function f_L takes care of the

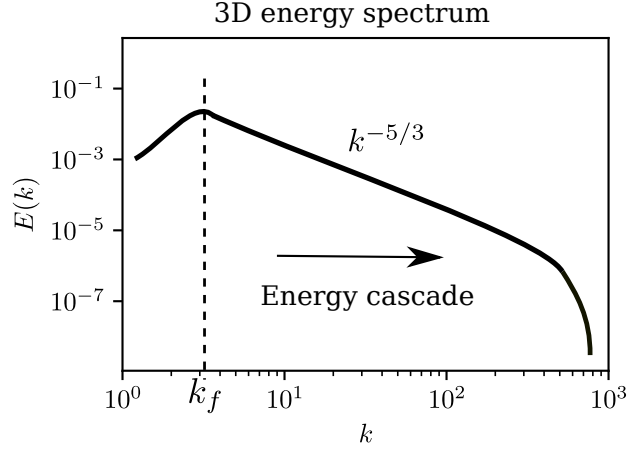


FIGURE 1.5: Schematic diagram [4] of kinetic energy spectrum for 3D homogeneous and isotropic turbulence.

shape of the energy spectrum in the energy-containing range and turns to unity for large kL . However, the function f_η determines the shape of the energy spectrum in the dissipation range and turns to unity for small $k\eta$. In the inertial range, both functions become unity so that the spectrum reduces to the Kolmogorov scaling.

The functional form of f_L is [41]:

$$f_L(kL) = \left(\frac{kL}{[(kL)^2 + c_L]^{1/2}} \right)^{5/3+p_0}, \quad (1.40)$$

where p_0 is a constant, and its value decides the behavior of the energy spectrum at the smaller wavenumbers. Here, c_L is also a positive constant. For $p_0 = 2$, the Pope spectrum shows k^2 scaling for the kinetic energy spectrum at the smaller wavenumbers. The functional form of f_η is given by [41]:

$$f_\eta(k\eta) = \exp \left(-\beta [(k\eta)^4 + c_\eta^4]^{1/4} - c\eta \right), \quad (1.41)$$

where β and c_η are constants. The value of $\beta = 5.2$ has been reported experimentally by Saddoughi and Veeravalli [55].

Pao's [56] has also proposed a model for the kinetic energy spectrum of three-

dimensional turbulence for the wavenumber range $k \gg k_f$, where k_f is the forcing wavenumber. In this model, Pao's has assumed that the ratio of the kinetic energy spectrum and the kinetic energy flux is independent of ν . The proposed model is expressed as follows:

$$E(k) = K_{K_0} \epsilon^{2/3} k^{-5/3} \exp\left(-\frac{3}{2} K_{K_0} \nu \epsilon^{-1/2} k^{4/3}\right). \quad (1.42)$$

While the form of the energy spectrum in the inertial range is well established. However, the behavior of the energy spectrum in the far dissipation range, i.e., $k > k_\eta$, is not still very clear. An energy spectrum in far dissipation range was proposed by Kraichnan [57] and the model is given by,

$$E(k) \approx (k\eta)^\gamma \exp(-\beta(k\eta)) \quad (1.43)$$

where γ , β , and n are real constants and k_η is the Kolmogorov dissipation scale. The values of γ , β and n are often debated in turbulence community. While $n = 1$ (cf. Smith and Reynold [58] supporting $n = 2$) is agreed upon by many researchers [59–63], there is relatively more disagreement about the value [57, 64–66] of γ ($= 3, -1.6, -2, 3.3$) and the value [55, 64, 66] of β ($= 4.9, 7.1, 5.2$). These models are essentially asymptotic series whose dominant terms dictate the Kolmogorov scaling, and they contain sufficient fitting parameters making the model appropriate for fitting data.

For the statistics of turbulent flows, it is customary to study the moments of velocity increments known as the structure functions. The q th order structure-function in terms of length scale l is defined as $S_q(\mathbf{l}) = \langle (\delta u(\mathbf{x}, \mathbf{l}))^q \rangle$, where $\delta u(\mathbf{x}, \mathbf{l}) = (u(\mathbf{x} + \mathbf{l}) - u(\mathbf{x}))$ is the velocity increment and $\langle \rangle$ denotes the averaging over space x . An extended result of Kolmogorov 4/5 law [40], where the third-order structure function depends on the mean dissipation rate (ϵ) and the length scale (l), is presented in Eq. (1.37). Kolmogorov discovered an exact law for longitudinal third-order structure function in homogeneous isotropic turbulence as

$$S_3(l) = \langle (\delta \mathbf{u}(\mathbf{x}, \mathbf{l}) \cdot \hat{\mathbf{l}})^3 \rangle = -\frac{4}{5} \langle \epsilon \rangle l, \quad (1.44)$$

where $\hat{\mathbf{l}} = \mathbf{l}/l$ is the unit vector. This exact law considers scale-to-scale self-similar behavior of turbulence in the inertial range of scales. The exact relation (Eq. 1.44) can

further be generalized, based on dimensional arguments, for higher-order structure functions as

$$S_q(l) \sim (\langle \epsilon \rangle l)^{\frac{q}{3}}. \quad (1.45)$$

Kolmogorov (1941) assumed that mean energy dissipation rate is necessary (in addition to the scale l) for uniquely determining the statistical properties of scales in the inertial range in turbulence, but Landau [67] had an objection on the necessity of the mean value of energy dissipation rate. He argued that the energy transfer fluctuates in the inertial range, and so does the dissipation rate. Subsequently, Kolmogorov [68] revised his assumption and defined a local mean dissipation rate,

$$\epsilon_l(\mathbf{l}, t) = \int_{V_l} \epsilon(x + l, t) dV, \quad (1.46)$$

where ϵ_l is the local mean dissipation rate for a sphere of radius l and ϵ_l scale as,

$$\langle \epsilon_l \rangle \sim l^{\tau_p}, \quad (1.47)$$

where τ_p is a scaling exponent. Taking the modification in dissipation rate, Eq. (1.45) becomes,

$$\begin{aligned} S_q(l) &\approx (\langle \epsilon_l \rangle l)^{\frac{q}{3}}, \\ &\approx l^{q/3 + \tau_p}. \end{aligned} \quad (1.48)$$

The deviation τ_p in the scaling of structure-function is attributed to intermittency in the system. Intermittency is essentially the manifestation of irregular alternation of large deviations of the flow from its mean. This also means a deviation in the scaling of the kinetic energy spectrum that now becomes,

$$E(k) \approx k^{-(5/3+\tau_2)}. \quad (1.49)$$

There are various models proposed to study intermittency. One of the models is the multifractal model proposed by Frisch [69]. In another model, Yaglom [70] considered the log-normal behavior of energy dissipation rate and derived the scaling exponent (ζ_q) for structure-function as,

$$\zeta_q = \frac{q}{3} + \frac{\mu}{18}(3q - q^2), \quad (1.50)$$

where μ is the intermittency parameter. According to Yaglom the scaling of kinetic energy spectrum deviates from Kolmogorov as,

$$E(k) \approx k^{-(5/3+\mu/9)}. \quad (1.51)$$

Sreenivasan and Kailasnath [71] reported the value of intermittency parameter $\mu = 0.25$ for atmospheric turbulence data. Intermittency in turbulence has been widely studied numerically [72,73] and experimentally [74–76], and a great deal of research is currently dedicated to intermittency in the turbulence community.

Intermittency is also actively being studied in rotating turbulence. Recent numerical as well as experimental studies on rotating turbulence show reduction in intermittency both in decaying and forced turbulent systems [16,77–79]. In the research work intended for this thesis, we have taken only the mean dissipation rate in our proposed models, and so we have not considered any intermittency correction in the models. Nonetheless, our models predict the results which are in very good agreement with the results from our numerical simulations. We believe that the decrease of intermittency with rotation makes our models (even though devoid of any intermittency corrections) decently agreeable with the numerical results.

1.3.1 Two-dimensional turbulence

There are dissimilarities between the 2D and the 3D turbulent flows. In particular, the vortex stretching is a purely 3D phenomenon, and it is absent in 2D turbulence [3, 80]. In 3D turbulence, the total kinetic energy and total kinetic helicity remain invariant, whereas, in 2D turbulence, the total kinetic energy, and total enstrophy are invariant [3, 4, 38]. Kraichnan reported the difference between 2D and 3D turbulence for the first time in 1967 [81]. Although idealized 2D turbulence is not observed in nature, many aspects of 2D turbulence are used to understand the geophysical flows, e.g., flows in the earth atmosphere and the oceans. The invariances of the energy and the enstrophy in 2D turbulence leads to the inverse cascade of kinetic energy and a forward cascade of enstrophy in the system.

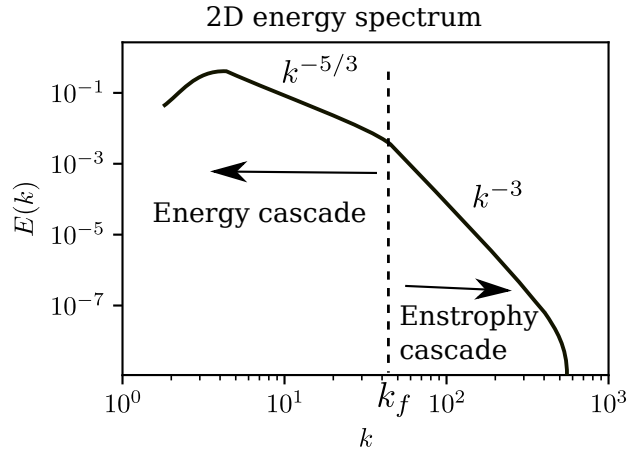


FIGURE 1.6: Schematic diagram [4] of kinetic energy spectrum for 2D homogeneous and isotropic turbulence.

The statistical behavior of 2D turbulence has been extensively investigated numerically as well as experimentally [82–92] by many researchers. In 2D turbulence, the kinetic energy spectrum scale as $E(k) \sim k^{-5/3}$ for the wavenumber range $k < k_f$ and $E(k) \sim k^{-3}$ in the wavenumber range for $k > k_f$. Some unique properties of 2D turbulence are shown in Fig. 1.6. Strong vortex structure is a prominent feature of 2D turbulence which occurs in the system due to the inverse cascade of the kinetic energy (energy transfer from the forcing scale to the box-size) [93]. Borue [94], Chertkov et al. [95], and Tran and Bowman [96] have investigated the kinetic energy spectrum of 2D turbulence system and reported $E(k) \sim k^{-3}$ scaling. However, Fischer and Bruneau

[97] have reported energy spectrum steeper than $k^{-5/3}$.

1.3.2 Towards rotating turbulence

The Coriolis force linearly affects all the scales present in the turbulent system. Specifically, it introduces a new length scale called Zeman scale [6] into the rotating turbulent system. The Zeman length scale corresponds to the wavenumber where the Coriolis force term and the non-linear term becomes comparable. The Zeman wavenumber (k_Ω) is estimated to be [6],

$$k_\Omega = \left(\frac{\Omega^3}{\epsilon} \right)^{1/2}. \quad (1.52)$$

Now, in the system, we have three wavenumbers, namely, the energy injection wavenumber k_f , the Zeman wavenumber k_Ω , and the Kolmogorov dissipation wavenumber k_η . We can understand the role of these wavenumbers in the system from Fig. 1.7.

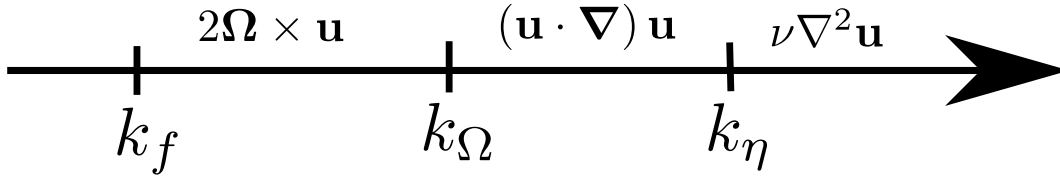


FIGURE 1.7: Schematic diagram for the comparison of different wavenumbers in rotating turbulence.

In Fig. 1.7, k_f is the forcing wavenumber (where energy is injected in the system), k_Ω is the Zeman wavenumber (the length scale where the Coriolis force is comparable to the inertial force) and k_η (where kinetic energy converts into heat) is Kolmogorov dissipation scale. Up to the Zeman wavenumber Coriolis force in the system dominant over both the nonlinear term and the dissipation term and from k_Ω to k_η nonlinear term is dominant over Coriolis term and dissipation term in the system. Beyond the dissipation scale, k_η dissipation term is dominant, and the kinetic energy is converted into heat. The Zeman wavenumber depends upon the strength of rotation. At a very high rotation rate, k_Ω may go beyond k_η , i.e., the effect of rotation may spread over all the scales present in the system.

The dynamics of the rotating turbulent system below and above k_Ω are quite

different. Below the wavenumber k_Ω , the system is anisotropic; and above k_Ω , the system is isotropic [98,99]. Now the question arises about the form of the kinetic energy spectrum of the rotating turbulent system in the wavenumber range $k_f < k < k_\Omega$ and $k_\Omega < k < k_\eta$. This question has been addressed quite extensively in the literature analytically [6,100], numerically [77,79,101–103], and experimentally [12,16,18,19,104,105].

1.3.3 Phenomenological model

The Coriolis force acts as the restoring force that generates inertial waves in the flow. In cylindrical co-ordinate, assume that a parcel of fluid suddenly displaced with an instantaneous velocity $\mathbf{u} = (u_r, 0, 0)$ along radial direction [9]. The angular velocity $\boldsymbol{\Omega}$ is in z -direction. The Coriolis force acts on the parcel $F_c = -2\boldsymbol{\Omega} \times \mathbf{u} = -2\Omega u_r \hat{e}_\theta$ along the direction of unit vector \hat{e}_θ and so pushes the fluid parcel along \hat{e}_θ . The Coriolis force does not contribute to the total energy of the flow. Thus, in an inviscid case, $\nu = 0$, total energy of the flow remains conserved. However, increase in u_θ due to the Coriolis force leads to the decrease in radial velocity u_r . Now the motion along unit vector \hat{e}_θ exerts a force on the fluid parcel originated due to the Coriolis force $F_c = 2\boldsymbol{\Omega} \times \mathbf{u}_\theta = -2\Omega u_\theta \hat{e}_r$ in the direction opposite to unit vector \hat{e}_r . Again the Coriolis force due to the velocity component opposite to the unit vector \hat{e}_r exerts a force on the fluid parcel, which decreases the velocity along \hat{e}_θ . As a result, the fluid particle starts oscillation and generates waves called inertial waves.

To understand the inertial wave and its properties in incompressible flow, we take curl of Eq. 1.6, and assume that $\text{Ro} \ll 1$ (i.e. $(\mathbf{u} \cdot \nabla) \mathbf{u} \rightarrow 0$, $\nu \rightarrow 0$ and zero forcing, we get [9,106],

$$\frac{\partial \boldsymbol{\omega}}{\partial t} = 2(\boldsymbol{\Omega} \cdot \nabla) \mathbf{u}. \quad (1.53)$$

Applying the operator $\nabla \times \partial/\partial t$ on Eq. 1.53 gives,

$$\frac{\partial^2}{\partial t^2} \nabla^2 \mathbf{u} + 2(\boldsymbol{\Omega} \cdot \nabla) \frac{\partial \boldsymbol{\omega}}{\partial t} = 0. \quad (1.54)$$

Using Eq. 1.53 and Eq. 1.54, we obtain a wave like equation,

$$\frac{\partial^2}{\partial t^2} \nabla^2 \mathbf{u} + 4 (\boldsymbol{\Omega} \cdot \nabla)^2 \mathbf{u} = 0. \quad (1.55)$$

We look for the solution of Eq. 1.55 in the form,

$$\mathbf{u} = \tilde{\mathbf{u}} e^{i(\mathbf{k} \cdot \mathbf{x} - \omega t)}, \quad (1.56)$$

where $\tilde{\mathbf{u}}$ is the amplitude, and ω is the frequency of the wave (called inertial wave). Substituting \mathbf{u} in Eq. 1.55, we obtain a dispersion relation of inertial waves,

$$\omega = \pm \frac{2\boldsymbol{\Omega} \cdot \mathbf{k}}{k} = \pm \frac{2\Omega k_{\parallel}}{k}, \quad (1.57)$$

where $k = |\mathbf{k}|$ and the rotation axis is along z -direction. The k_{\parallel} is the wavenumber along the direction of rotation. The inertial waves propagate with the group velocity \mathbf{c}_g and the phase velocity \mathbf{c}_p . The group velocity of (a wavepacket of) inertial waves is,

$$\mathbf{c}_g = \pm \frac{2k^2 \boldsymbol{\Omega} - 2(\boldsymbol{\Omega} \cdot \mathbf{k}) \mathbf{k}}{k^3}, \quad (1.58)$$

and the phase velocity of an inertial wave is,

$$\mathbf{c}_p = \pm \frac{2(\mathbf{k} \cdot \boldsymbol{\Omega})}{k^3}. \quad (1.59)$$

The nonlinear interaction of wavepackets of (inertial) waves results in the transfer of kinetic energy. The transfer of significant amount of energy (with respect to the energy content of the length scale) from length scale l to the smaller length scales requires a multitude of such nonlinear interactions or collisions of wavepackets of inertial waves. A wave packet gets distorted, in a typical collision, by an amount $\delta u_l \sim (\mathbf{u} \cdot \nabla) \mathbf{u} t_{\Omega} \sim (u_l^2/l) t_{\Omega} \sim (u_l/l) u_l t_{\Omega} \sim (T_{NL} \omega)^{-1} u_l$, where u_l is the velocity of length scale l , $T_{NL} = u_l/l$ is the nonlinear time scale, and t_{Ω} is the time scale of inertial waves [107]. The significant distortion in velocity field requires $N \sim (u_l/\delta u_l)^2$ number of collisions. The time (τ_{tr}) required to transfer the energy from length scale l to smaller length scales becomes,

$$\tau_{tr} = N t_{\Omega} = (T_{NL} \omega)^2 t_{\Omega} = T_{NL}^2 \omega. \quad (1.60)$$

From dimensional analysis, the rate of transfer of energy can be estimated as,

$$\epsilon \sim \frac{u^2}{\tau_{tr}} \sim \frac{E(k_{\perp}, k_{\parallel}) k_{\perp} k_{\parallel}}{\tau_{tr}}. \quad (1.61)$$

In anisotropic limit $k_{\perp} \gg k_{\parallel}$, the nonlinear time is given by $T_{NL} \sim (k_{\perp} u)^{-1}$ and so the energy transfer time (τ_{tr}) becomes,

$$\tau_{tr} \sim \frac{\Omega}{k_{\perp}^4 E(k_{\perp}, k_{\parallel})}. \quad (1.62)$$

The energy spectrum is obtained from the Eq. 1.61 after substituting τ_{tr} from the above relation [108],

$$E(k_{\perp}, k_{\parallel}) \sim (\epsilon \Omega)^{1/2} k_{\perp}^{-5/2} k_{\parallel}^{-1/2}. \quad (1.63)$$

This energy spectrum is known as Kuznetsov–Zakharov–Kolmogorov (KZK) spectrum. This is to note that the KZK spectrum for anisotropic turbulence is applicable in the anisotropic limit only.

The rotation makes the system anisotropic, and the kinetic energy spectrum of the system does not show exactly Kolmogorov scaling. The behavior of the kinetic energy spectrum in the case of rotating turbulence is an open problem. Although this has been investigated by many researchers, the problem of the scaling of the kinetic energy spectrum is not yet settled [16, 77, 79, 101–103, 109–114]. In the next section, we discuss some of the existing literature of the kinetic energy spectrum and the behavior of kinetic energy transfer in the rotating turbulence.

1.4 Literature survey on rotating turbulence

In the rotating frame of reference, the flow is affected by the Coriolis and the centrifugal forces. While the centrifugal force may be absorbed into the pressure gradient term of the Navier–Stokes equation, the Coriolis force, which is perpendicular to the direction of rotation, tends to make the flow quasi two-dimensional (2D). The Taylor–Proudman theorem [24] predicts formation of the Taylor columns and emergence of quasi 2D behavior. Note, however, that the Taylor–Proudman theorem is applicable in the linear

limit of rapidly rotating steady flow. The quasi-2D behavior of the turbulent rotating fluid is, however, much more subtle and is full of defining signatures that are still not fully understood [34–37]. As mentioned earlier, 2D turbulence has its own caveats. The velocity component along the rotation axis, although relatively weaker than the perpendicular component, plays a significant role in rotating turbulence. The intricate statistical behavior of the rotating turbulence tempts the researcher to study the system. Now, we briefly discuss the efforts made by the researchers to understand the complexity of the system.

1.4.1 Coherent structures

The Coriolis force acts on the system in the direction perpendicular to the velocity field. Although the Coriolis force does not do any work on fluid, it is the main reason behind the formation of columnar structures in the rotating turbulence. This columnar structure is one of the prominent features of rotating turbulence. Nonlinear interactions among the inertial waves too yield quasi-2D behaviour [102, 108, 115, 116]—a result more relevant to the present study of the turbulent rotating flow. Note that two-dimensionalization of the flow leads to an inverse cascade of energy (Iyer *et al.* [117]) that strengthens the columnar structures. The inverse cascade of kinetic energy also found in three-dimensional helical turbulence which is not related to the two-dimensionalization of the flow (cf. Biferale *et al.* [118, 119]). Similar structures are predicted by the Taylor–Proudman theorem in the linear limit (i.e., when the convective term in Eq. (1.6) is negligible) of rapidly rotating laminar flow [24]. The existence of Taylor columns was first predicted by Proudman [120] analytically, and this was experimentally verified by Taylor [121]. Evidently, these features go beyond the linear limit. As mentioned earlier, through the formation of the columnar structure in the system, the nonlinear term redistributes the energy in an anisotropic way and makes the system quasi-two-dimensional. It has been verified in experimental as well as numerical studies [13, 102, 108, 112, 115, 116, 122, 123].

The first experimental study of the decaying rotating turbulence was conducted by Ibbetson and Tritton [124] in an annular cylinder kept on a rotating table. The turbulence in the system was generated by towing a grid between the top and bottom of the cylinder. The results show a fast increase of length scale along the direction of rotation as compared to the length scale in the plane perpendicular to the rotation

axis. They reported an increase in the energy dissipation rate. However, the decrease in the dissipation rate in rotating turbulence has been validated by many researchers experimentally [17] and numerically [102, 125–127]. On the other hand, Jacquin et al. reported a decrease in the energy dissipation rate due to rotation [17]. The increase of the integral length scale in rotating turbulence is a signature of the formation of columnar structures in the system. These columnar structures are primarily cyclonic (the vorticity is in the direction of rotation). The existence of antisymmetric cyclonic and anticyclonic behavior in the system has been examined by Morize, et al. [122] experimentally, where the turbulence in the system is generated by towing a grid in a rotating water tank. Davidson et al. [128] reported the dominance of inertial waves generated by the linear term (Coriolis force) in the system over the nonlinear term in homogeneous turbulence. Furthermore, the inertial wave plays a major role in structure formation in homogeneous decaying rotating turbulence with $Ro \sim \mathcal{O}(1)$ [13].

Apart from the experimental study, the coherent structures in rotating turbulence have been extensively studied numerically [102, 125–127]. The numerical evidence of a decrease in the dissipation rate and increase of the integral length scale was reported by Bardina et al. [129]. Rotation makes the system asymmetric, i.e., cyclones are more stable than the anticyclones in the rotating turbulence system when $2\Omega = [\omega_{2D}]_{rms}$ [126]. Using large-scale simulations on 4096^3 grid, Biferale *et al.* [102] studied in detail the complex structures of rotating turbulence, in particular, the vortical structures and 3D anisotropic fluctuations. The large coherent structure in the rotating system accounts for the inverse cascade of energy (transfer of energy from higher wavenumber towards smaller wavenumber) in the system. Other than the large scale coherent structures in the system, rotation makes the system anisotropic, i.e., the velocity fields and other physical quantities become the function of angle, where the reference for the angle is taken from the axis of rotation.

1.4.2 Kinetic energy spectrum

One of the least understood non-equilibrium statistical mechanical system is a fully developed turbulent flow [130–132]. Intriguingly, the scaling law of the energy spectrum in the inertial range changes with the rotation rate in a way so as to two-dimensionalize the three-dimensional (3D) fluid turbulence. As mentioned earlier, Kolmogorov [40, 133] proposed a theory for homogeneous and isotropic three-dimensional (3D) hydro-

dynamic turbulence, according to which the inertial-range energy spectrum $E(k) \sim \epsilon^{2/3}k^{-5/3}$. Here ϵ is the energy dissipation rate that equals the energy flux, and k is the wavenumber. This theory successfully explains many experimental and numerical findings [4, 24, 38, 134–137]. Kraichnan [81] however showed that the two-dimensional (2D) hydrodynamic turbulence has further complexities—here the small wavenumber Fourier modes exhibit inverse cascade of energy with $E(k) \sim k^{-5/3}$, while the large wavenumber Fourier modes exhibit forward enstrophy cascade with $E(k) \sim k^{-3}$.

The fluid flows in nature and in laboratory are generally quite complicated. For example, they may involve external magnetic field, rotation, or buoyancy [4, 24, 38, 134–137]. The aforementioned hydrodynamic turbulence phenomenologies play major role in modeling these flows. Researchers have shown that the external magnetic field [30, 138, 139] and rotation [4, 9, 140] typically affect the energy spectrum in the inertial range.

Several models have been proposed to study the kinetic energy spectrum of rotating turbulence. Zeman [6] proposed a dual spectrum: the large- k modes exhibit Kolmogorov's spectrum ($k^{-5/3}$), while small- k modes show $k^{-11/5}$ spectrum. Zhou [100] proposed that $E(k) \sim k^{-2}$ for the entire inertial range when the rotation rate is very high, whereas Smith and Waleffe [110] argued that $E(k_{\perp}) \sim k_{\perp}^{-3}$, where k_{\perp}, k_{\parallel} are respectively the components of wavevector \mathbf{k} perpendicular and parallel to the rotation axis. Chakraborty [141] argued that $E(k) \sim k^m$ where $m \in [-2, -3]$; the spectral range can be further confined to $m \in [-2, -7/3]$ by kinetic helicity. Additionally, in the limit of very strong rotation, Kraichnan [57] proposed that $E(k) \sim \exp(-2\nu k^2 t)$, where ν is the kinematic viscosity and t is the time elapsed. This model assumes absence of nonlinearity. Baqui and Davidson [142] and Baqui *et al.* [114] constructed a phenomenological theory of rotating turbulence and argued that the flow is anisotropic with $E(k_{\perp}) \sim \epsilon^{2/3}k_{\perp}^{-5/3}$ and $E(k_{\parallel}) \sim \epsilon^{2/3}(L_{\parallel}/L_{\perp})^{2/3}k_{\parallel}^{-5/3}$, where L_{\parallel} and L_{\perp} are respectively the integral length scales parallel and perpendicular to the direction of rotation. However, an intriguing aspect of the results of Baqui and coworkers is the absence of power law scaling in the inertial range of $E(k)$. In this thesis we show that the nonlinearity, though weak, is present, and it produces nonzero energy and enstrophy fluxes.

Many researchers [12, 16, 18, 19, 104, 105], have attempted to verify the aforementioned models of rotating turbulence using experiments. Morize *et al.* [122] studied decaying turbulence in a rotating tank and showed that the energy spectrum steepens

from $k^{-5/3}$ to k^{-2} , or even further as the rotation speed is increased. Baroud et al. [16] reported k^{-2} scaling for forced rotating turbulence experimentally.

A large number of numerical experiments have been performed on rotating turbulence [129, 143–145]. Yang and Domaradzki [101], Müller and Thiele [77], Mininni *et al.* [79], and Biferale *et al.* [102] showed that the energy spectrum of rotating turbulence is approximately k^{-2} or k_{\perp}^{-2} . However, Smith and Lee [112] and Sen *et al.* [103] argued that the energy spectrum is proportional to k_{\perp}^{-3} . Mininni [98] studied the rotating helical turbulence numerically and found that for $k > k_{\Omega}$, the energy spectrum exponent is -2.2 , and the helicity spectrum exponent is -1.8 ; here k_{Ω} is the Zeman wavenumber. For $k > k_{\Omega}$, they observed that the system becomes isotropic, and both energy and helicity spectra exhibit $k^{-5/3}$ scaling. Yeung and Zhou [109] studied the forced rotating turbulent system numerically and reported that energy spectrum underwent a transition from $k^{-5/3}$ to k^{-2} . Smith and Waleffe [110] examined the dynamical properties of forced rotating fluid and observed k^{-3} scaling for $k < k_f$. Baroud et al. [16] reported that the kinetic energy spectrum becomes k^{-2} for rotating quasi-2D turbulent flow for forced rotating turbulent system. Hattori et al. [111] also reported the steepening of energy spectrum from $k^{-5/3}$ to k^{-2} using shell model for forced rotating turbulent system. Apart from these power-law scalings for relatively larger scales, the energy spectrum for the smaller scales in rotating turbulence is equally enigmatic.

In nonrotating 3D turbulent fluids, subsequent to a model proposed by Kraichnan [57] for the kinetic energy spectrum in far dissipation range, Pao [56] and Pope [41] separately proposed models which are applicable in both the inertial as well as the dissipation ranges. These two model spectra respectively are $E(k) = K_0 \epsilon^{2/3} k^{-5/3} \exp(-\frac{3}{2} \alpha \nu \epsilon^{-1/3} k^{4/3})$, where K_0 is Kolmogorov constant and ν is the kinematic viscosity; and $E(k) = C \epsilon^{2/3} k^{-5/3} f_L(kL) f_{\eta}(k\eta)$, where C is a real constant, L is the integral length scale, η is the Kolmogorov length scale, and f_L and f_{η} are two non-dimensional functions [41]. Another widely used typical phenomenological form of the energy spectrum in far dissipation range of 3D isotropic homogeneous turbulence is given by $E(k) \sim (k/k_{\eta})^{\gamma} \exp[-\beta(k/k_{\eta})^n]$, where γ , β , and n are real constants and k_{η} is the Kolmogorov dissipation scale. The values of γ , β and n are often debated in turbulence community. While $n = 1$ (cf. Smith and Reynold [58] supporting $n = 2$) is agreed upon by many researchers [59–63], there is relatively more disagreement about the value [57, 64–66] of γ ($= 3, -1.6, -2, 3.3$) and the value [55, 64, 66] of β ($= 4.9, 7.1, 5.2$). Needless to say, as far as the more complex problem of the forced rotating turbulence

is concerned, the issue of such an energy spectrum is even wider open. Given the uncertainty in the two exponents, the usage of this energy spectrum is debatable. In fact, to the best of our knowledge, no one has reported such an energy spectrum for smaller scales that extend far into the dissipation range of the forced rotating fluid turbulence.

1.4.3 Kinetic energy transfer in rotating turbulence

The energy transfer between different scales is a defining feature of any kind of turbulent flow. This exchange of energy in the system occurs owing to the nonlinear interactions among different scales. In 3D (non-rotating) isotropic homogeneous turbulence, the nonlinear terms in the Navier–Stokes equations are solely responsible for the transfer of energy from the larger scales (where energy is usually injected into the system) to the small scales (where energy is dissipated into heat by viscous term). This is essentially the backbone picture of Kolmogorov’s phenomenological model of turbulence [133]. Over the last fifty years, the nature of the energy transfer in 3D turbulence—including the question whether the transfer is local or nonlocal in nature—has been extensively investigated theoretically [146–150], experimentally [151–153] and numerically [154–168].

The scale-to-scale energy transfer in the rotating hydrodynamic turbulence gives rise to dual cascade of the kinetic energy: an inverse cascade among the relatively smaller wavenumbers and a forward cascade in the comparatively higher wavenumber region. The energy transfer and the frequently accompanying inverse cascade in the rotating turbulence have been explored in quite some detail [1, 15, 22, 77, 79, 99, 103, 108–110, 112, 116, 127, 145, 169–181]. The inverse cascade can be credited with the formation of the coherent structures, which is one of the most prominent features of the rotating turbulence [13, 14, 122, 126, 144, 182–185]. In the presence of the rotation, the Coriolis force redistributes the kinetic energy and the initial three dimensional isotropic system becomes anisotropic. With the increase in the rotation rate, the three dimensional (3D) turbulence progressively starts showing signatures that mimic the features of the two-dimensional turbulence; in other word, the rotating turbulence is quasi-two-dimensionalized [34, 35, 141, 186].

The case of the rapidly rotating 3D turbulence is, however, much more involved not only because of the introduction of another time-scale in the problem, but also because the system is predominantly anisotropic. Thus, in order to understand the sys-

tem, an understanding of the anisotropic properties of the energy transfer is paramount. Lamriben et al. [22] have experimentally measured the anisotropic behaviour of energy transfer in decaying rotating turbulence and have found the anisotropy of the energy transfer to be mostly driven by the angular dependence of the flux density function. Delache et al. [99] have decomposed the spectral space into rings (the intersections of shells and sectors) [5, 187] and have studied the energy transfers inside the rings, i.e., the angular dependence of energy transfer. They have reported that the energy transfer is predominantly negative at the larger scales and positive at the smaller scales in each ring. The anisotropic energy transfer has been studied analytically (using EDQNM approximation) by Cambon and Jacquin [169]; and by Waleffe [188], who has studied the behaviour of the energy transfer using instability assumption for the resonance triads. In both the papers, it has been reported that the transfer of energy is from the polar region to the equatorial region.

In this context it is worth pointing out that there are strong similarities between the rotating turbulence and the magnetohydrodynamic (MHD) turbulence. Specifically, in both the system, the respective external forces—the Coriolis due to the rotation and the Lorentz force due to the magnetic field—affects only the dynamics. The behavior of the energy transfer in the MHD turbulence has been thoroughly examined in the scientific community [5, 28, 31, 139, 187, 189–203]. For example, Teaca et al. [187] have studied the energy transfer between rings numerically. They have reported that the energy transfers between u to u , and b to b (where u is the velocity field and b is the magnetic field) are from the equatorial region to the polar region, whereas the transfer of the energy for u to b is from the polar to the equatorial region. Similarly, Reddy et al. [5] have shown that the rings with higher polar angles transfer energy to the ones with lower polar angles. Knaepen and Moreau [204] also support this conclusion. The mechanism behind the energy transfer's direction may be argued to depend on the Joule dissipation in the MHD turbulence. In quasi-static MHD [204–206] turbulence the Joule dissipation of energy along the direction of the magnetic field is relatively higher and it is zero along the equator. Thus, the energy should be transferred from the equator to the poles due to the inherent nonlinear interactions in order to balance the Joule dissipation rate so that a steady state is maintained. However, this direction of energy transfer is not unanimously accepted: the results reported by Oughton et al. [207] show that the energy is transferred from the polar region to the equatorial region, and Galtier and Chandran [208] also have reported that the energy transfer happens preferentially towards the modes perpendicular to the magnetic field.

Rotation suppresses the energy cascade, hence several researchers have revisited the decay law of total energy. Thiele and Muller [113] observed that the total energy $E \sim t^{-1.5}$ for nonrotating flows, but the exponent decreases from 1.5 to ≈ 0.5 as the rotation speed is increased. Baqui and Davidson [142] also arrived at similar conclusions. Teitelbaum and Mininni [209] however argued that $E \sim t^{-1}$ for nonhelical rotating flows, but $E \sim t^{-1/3}$ for the helical ones. Here the inverse cascade of energy suppresses the decay of turbulence.

1.5 Outline of the thesis

The overall aim of this thesis is to understand the effects of rotation on nonlinear interaction in hydrodynamic turbulence. The nonlinear term helps to transfer the energy from one scale to the other scales. Rotation thus affects the distribution of energy in different scales, which in turn affects the behavior of the kinetic energy spectrum. So we investigate the statistical properties like the kinetic energy spectrum and the anisotropic energy transfer in both the decaying and the forced rotating turbulence. The outline of the thesis is as follows:

- In chapter 2, we discuss the numerical scheme employed to solve the governing equations of flow. We use a pseudo-spectral code Tarang in our numerical simulations. We also discuss the formulation of the kinetic energy spectrum, the kinetic energy flux, the shell-to-shell energy transfer, the ring-to-ring energy transfer, and the Conical flux in rotating turbulence. We discuss the initial conditions and the random forcing scheme as used in the numerical simulations.
- In chapter 3, we investigate the energy spectrum and structures of rapidly rotating decaying turbulence. Here we focus on the nonhelical flows (zero kinetic helicity). We perform sufficiently high-resolution spectral simulations that help us analyze the asymptotic regime. We find that as the turbulent flow evolves in time, the Rossby number decreases to $\sim 10^{-3}$, and the flow becomes quasi-two-dimensional with strong coherent columnar structures arising due to the inverse cascade of energy. We establish that a major fraction of energy is confined in Fourier modes $(\pm 1, 0, 0)$ and $(0, \pm 1, 0)$ that corresponds to the largest columnar structure in the flow. Following the earlier works on rotating turbulence, we observe a strong inverse cascade of energy that strengthens the coherent columnar

structures. The kinetic energy trapped in such structures dissipates very slowly, and hence the Reynolds number remains quite large with slow variation in time. For wavenumbers (k) greater than the enstrophy dissipation wavenumber (k_d), our phenomenological arguments and numerical study show that the enstrophy flux and spectrum of a horizontal cross-section perpendicular to the axis of rotation are given by $\epsilon_\omega \exp(-C(k/k_d)^2)$ and $C\epsilon_\omega^{2/3}k^{-1} \exp(-C(k/k_d)^2)$ respectively; for this 2D flow, ϵ_ω is the enstrophy dissipation rate, and C is a constant. Using these results, we propose a new form for the energy spectrum of rapidly rotating decaying turbulence: $E(k) = C\epsilon_\omega^{2/3}k^{-3} \exp(-C(k/k_d)^2)$. This model of the energy spectrum is based on wavenumber-dependent enstrophy flux, and it deviates significantly from the power-law energy spectrum reported earlier.

- In chapter 4, we investigate the behavior of the kinetic energy spectrum for the forced rotating turbulence. The introduction of forcing at an intermediate scale—corresponding wavenumber being k_f —breaks the kinetic energy spectrum into two disjoint region: larger scales $k < k_f$ and smaller scales $k > k_f$. Contrary to what has been observed in the decaying case, the energy spectrum in the forced case shows power law scaling close to $E(k_\perp, k_\parallel) \sim k_\perp^{-5/2}k_\parallel^{-1/2}$ in highly anisotropic large scales. (The subscripts ‘ \perp ’ and ‘ \parallel ’ respectively refer to the directions perpendicular and parallel to the rotation axis). In the rather isotropic far dissipation range, the energy spectrum becomes exponential function of ‘ $-k$ ’. Additionally, although we have observed that $(\pm 1, 0, 0)$ and $(0, \pm 1, 0)$ still contain a major fraction of the total energy, the energy content in the intermediate and the smaller scales is much more than that for the decaying rotating turbulent; as a result, one observes rather diffused columnar structures in case of forced rotating turbulence. The main aim of our thesis is to elaborate on these interesting results and to contrast the forced turbulence with the decaying one.
- In chapter 5, we have performed direct numerical simulation of 512^3 grid resolution for the decaying as well as the forced rotating turbulent fluids, and investigated the anisotropic nature of the transfer of energy. As the main result, we establish that the energy is transferred from the polar region to the equatorial region in the case of the decaying rotating turbulence. However, for the case of the forced rotating turbulence, we have observed two different types of energy transfers: (a) in wavenumber-region $|\mathbf{k}| < k_f$ (where \mathbf{k} is the wave vector and k_f is the forcing wavenumber), the energy is transferred from the equatorial region to the polar region; and (b) in region $|\mathbf{k}| > k_f$, the energy is transferred from the

poles towards the equator.

- Finally, in chapter 6, we summarize our results on the rotating turbulence and discuss some future directions of research in the context of our work.

Chapter 2

Numerical scheme to compute statistical quantities

It is going to be necessary that everything that happens in a finite volume of space and time would have to be analyzable with a finite number of logical operations. The present theory of physics is not that way, apparently. It allows space to go down into infinitesimal distances, wavelengths to get infinitely great, terms to be summed in infinite order, and so forth; and therefore, if this proposition [that physics is computer-simulatable] is right, physical law is wrong.

– Richard P. Feynman

Turbulence is an unsolved problem in classical physics. The Navier–Stokes (NS) equation is the governing equation of turbulent flows. The nonlinear property of the NS equation makes it analytically unsolvable except a few elementary problems. Since turbulence is ubiquitous in nature, it is interesting to explore its behaviour in great detail. We solve this equation numerically. In this chapter, we discuss the numerical scheme in detail, which is used to solve the governing equation of the flow in a rotating frame of reference. We used a pseudo-spectral solver TARANG [210,211] for numerical simulations of turbulent flows in a cubic box geometry. To solve the NS equation for incompressible flow, there are other methods like the projection operator method, velocity vector potential, etc. In the projection operator method, the projection operator P is defined as $P\mathbf{u} = \mathbf{u}$, which gives $P(\nabla p) = 0$. Applying this operator on the NS equation gives an equation of the velocity field, which does not contain any pressure

part. The pressure part can be computed using gradients of the term containing the nonlinear part and viscous dissipation part [212]. In the vector potential method, velocity in 3D is represented by $\mathbf{u} = \nabla \times \mathbf{A}$, where \mathbf{A} is a vector potential, and it satisfies $\nabla \cdot \mathbf{A} = 0$, whereas in the case of 2D, \mathbf{A} is replaced by stream function ψ . The statistical properties have been studied using stream functions in 2D turbulence [89,96].

This chapter is organized as follows: In Sec. 2.1, we describe the pseudo-spectral method to solve the governing equation of the flow. Here, we discuss the pseudo-spectral method in detail. In Sec. 2.2, we discuss the initial condition chosen for the simulation and forcing scheme applied to the system. In section 2.3-2.4, we show the formalism to compute the following statistical quantities, namely, kinetic energy spectrum, kinetic energy flux, shell-to-shell energy transfer, ring-to-ring energy transfer, and conical energy flux. In the last section 2.5, we detail the simulation parameters of rotating turbulence.

2.1 Simulation method

We perform simulations in a three-dimensional cubic periodic box with box size $(2\pi)^3$ i.e. $L_x \times L_y \times L_z = 2\pi \times 2\pi \times 2\pi$. The Fourier expansion of velocity fields can be written as,

$$u_x(x, y, z) = \sum_{k_x, k_y, k_z} \hat{u}_x(k_x, k_y, k_z) \exp(i(k_x x + k_y y + k_z z)), \quad (2.1)$$

$$u_y(x, y, z) = \sum_{k_x, k_y, k_z} \hat{u}_y(k_x, k_y, k_z) \exp(i(k_x x + k_y y + k_z z)), \quad (2.2)$$

$$u_z(x, y, z) = \sum_{k_x, k_y, k_z} \hat{u}_z(k_x, k_y, k_z) \exp(i(k_x x + k_y y + k_z z)), \quad (2.3)$$

where $\mathbf{u} = (u_x, u_y, u_z)$ is the velocity field in real space, whereas $\hat{\mathbf{u}} = (\hat{u}_x, \hat{u}_y, \hat{u}_z)$ is the velocity field in Fourier space. The wave vector $\mathbf{k} = (k_x, k_y, k_z) = (\frac{2\pi n_x}{L_x}, \frac{2\pi n_y}{L_y}, \frac{2\pi n_z}{L_z})$, where n_x, n_y and n_z are integers.

In Fourier space, the NS equation of incompressible flow in a rotating frame of

reference is given by [25,26];

$$\frac{d\hat{\mathbf{u}}(\mathbf{k})}{dt} = -i\mathbf{k}\hat{p}(\mathbf{k}) - \hat{\mathbf{N}}(\mathbf{k}) - 2\boldsymbol{\Omega} \times \hat{\mathbf{u}}(\mathbf{k}) - \nu k^2 \hat{\mathbf{u}}(\mathbf{k}) + \hat{\mathbf{f}}(\mathbf{k}), \quad (2.4)$$

$$\mathbf{k} \cdot \hat{\mathbf{u}}(\mathbf{k}) = 0, \quad (2.5)$$

with the nonlinear term,

$$\hat{\mathbf{N}}(\mathbf{k}) = i \sum_{\mathbf{p}} [\mathbf{k} \cdot \hat{\mathbf{u}}(\mathbf{k} - \mathbf{p})] \hat{\mathbf{u}}(\mathbf{p}), \quad (2.6)$$

where $\hat{\mathbf{u}}(\mathbf{k})$, $\hat{\mathbf{f}}(\mathbf{k})$, $\boldsymbol{\Omega}$ and $\hat{p}(\mathbf{k})$ are velocity field, forcing function, rotation rate and modified pressure, respectively. The modified pressure includes centrifugal term. In our simulations, we take the rotation axis of angular velocity $\boldsymbol{\Omega}$ along the z -direction. Here, the term $\hat{\mathbf{N}}(\mathbf{k})$ obtained from the convolution of nonlinear term in Fourier space is responsible for the transfer of energy from one Fourier mode to the other Fourier modes.

The pressure in Fourier space is obtained by taking scalar product of $i\mathbf{k}$ and Eq. 2.4 in addition with the incompressibility condition (Eq. 2.6), we get the following expression for pressure in Fourier space,

$$\hat{p}(\mathbf{k}) = \frac{1}{|\mathbf{k}|^2} i\mathbf{k} \cdot [\hat{\mathbf{N}}(\mathbf{k}) + 2\boldsymbol{\Omega} \times \hat{\mathbf{u}}(\mathbf{k}) - \hat{\mathbf{f}}(\mathbf{k})]. \quad (2.7)$$

In our case the force is assumed to be divergence free i.e $\mathbf{k} \cdot \hat{\mathbf{f}}(\mathbf{k}) = 0$, and so the pressure term becomes,

$$\hat{p}(\mathbf{k}) = \frac{1}{|\mathbf{k}|^2} i\mathbf{k} \cdot [\hat{\mathbf{N}}(\mathbf{k}) + 2\boldsymbol{\Omega} \times \hat{\mathbf{u}}(\mathbf{k})]. \quad (2.8)$$

Substituting pressure term from Eq. 2.8 in Eq. 2.4, and choosing $\hat{\mathbf{f}}(\mathbf{k}) = 0$, Eq. 2.4 (in tensorial form), is given by;

$$\left(\frac{d}{dt} + \nu k^2 \right) \hat{u}_i(\mathbf{k}) = k_i \frac{k_j \hat{N}_j(\mathbf{k}) + 2\epsilon_{jlm} k_j \Omega_l \hat{u}_m(\mathbf{k})}{|\mathbf{k}|^2} - \hat{N}_i(\mathbf{k}) - 2\epsilon_{ijk} \Omega_j \hat{u}_k. \quad (2.9)$$

There are two relevant time scales in turbulent flows, large-eddy turnover time, and small scale viscous time. These two-time scales are very different in order of magnitude. We use the exponential trick [25, 213] to reduce the problem to one time scale

by absorbing the viscous term in the velocity field. In our simulations the components of wave vector lie in the domain $k_x = (-N_x/2 : N_x/2)$, $k_y = (-N_y/2 : N_y/2)$ and $k_z = (-N_z/2 : N_z/2)$, where N_x, N_y and N_z are the grid points taken along x, y and z direction respectively. The effective computational domain in Fourier space reduces to the wavenumber range $k_x = (-N/2 : N/2)$, $k_y = (-N/2 : N/2)$ and $k_z = (0 : N/2)$ due to reality condition $\mathbf{u}(-\mathbf{k}) = \mathbf{u}^*(\mathbf{k})$. Time advancement is performed in this domain range.

The computation of the nonlinear term is time-consuming and expensive for the following reason. In Fourier space, the nonlinear term $(\mathbf{u} \cdot \nabla) \mathbf{u}$ is converted into convolution term. The computation of convolution term in Fourier space of $M = N_x \times N_y \times N_z$ grid points requires $\mathcal{O}(M^2)$ operations. Nevertheless, the number of operations can be reduced to $\mathcal{O}(M \log M)$ by using the pseudo-spectral method [25]. In pseudo-spectral method, we use inverse Fast Fourier transform to obtain velocity field in real space, which costs $[\mathcal{O}(M \log M)]$ operations. The nonlinear term in real space can be written as $\partial_j (u_i u_j)$. We multiply the velocity fields in real space and then perform forward Fast Fourier transform of the product, which again takes $[\mathcal{O}(M \log M)]$ operations. The schematic of the pseudo-spectral method is shown in Fig. 2.1. It is to note that the forward Fourier transform of the product of velocity fields generates some spurious modes in Fourier space [25, 26]. These spurious Fourier modes add error to the computation of statistical physical quantities at large wavenumber. This error in the convolution terms is called aliasing error, which is removed by using a 2/3 dealiasing rule, where only 2/3 parts of the modes are considered in each direction. We used an in house pseudo-spectral code TARANG [210, 211]. In this section, we discuss the pseudo-spectral code TARANG and the technical details.

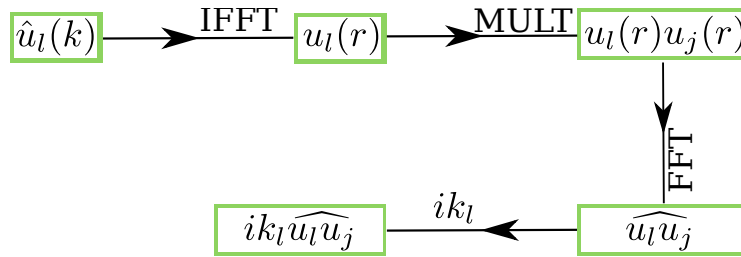


FIGURE 2.1: Schematic diagram for the computation of nonlinear term $(\mathbf{u} \cdot \nabla) \mathbf{u}$ by pseudo-spectral method. This figure is adapted from a figure from Ref. [3].

Now we describe the algorithm of the pseudo-spectral method:

1. We use the Fast-Fourier-Transform FFTK (FFT Kanpur) library for the computation of nonlinear term $(\mathbf{u} \cdot \nabla) \mathbf{u}$, which converts the real field data into Fourier space and vice-versa. Here, we describe the method in details,
 - (a) First, we use inverse Fourier transform to compute $u(x)$ from $\hat{u}(k)$.
 - (b) We compute the product of velocity fields (nonlinear term), which is $u_i(x)u_j(x)$ in real space.
 - (c) We compute FFT $[u_i(x)u_j(x)]$.
 - (d) Finally, we take a product of ik_j with FFT $[u_i(x)u_j(x)]$ for $j = 1, 2, 3$. This procedure is shown in Fig. 2.1.
2. We use 2/3 dealiasing rule to get rid of aliasing error (as explained previously).
3. We use incompressibility condition ($ik_j u_j(k) = 0$) for the computation of pressure term. The pressure term in Fourier space is,

$$\hat{p}(\mathbf{k}) = \frac{1}{|\mathbf{k}|^2} i\mathbf{k} \cdot \left[\hat{\mathbf{N}}(\mathbf{k}) + 2\boldsymbol{\Omega} \times \hat{\mathbf{u}}(\mathbf{k}) - \hat{\mathbf{f}}(\mathbf{k}) \right], \quad (2.10)$$

where $\hat{\mathbf{N}}(\mathbf{k})$ is the Fourier transform of the nonlinear term and is computed in the previous steps. In our simulations the forcing term is divergence free i.e. $\mathbf{k} \cdot \hat{\mathbf{f}}(\mathbf{k}) = 0$.

4. We use the fourth-order Runge-Kutta (RK4) scheme for time-stepping and Courant-Friedrich-Lewy (CFL) condition to optimize the time-stepping (Δt). The CFL condition for minimum time step δt is,

$$\Delta t = C_{CFL} \frac{\Delta x}{U'}, \quad (2.11)$$

where C_{CFL} is set to 0.5, Δx is the length of the smallest grid, and U' is the rms velocity.

In the next section, we discuss about the initial condition and the forcing scheme employed in our numerical simulations.

2.2 Initial condition and forcing scheme

To solve the NS equation, we require initial and boundary conditions for the velocity field. In our numerical simulations for 3D hydrodynamic flows, we take the following energy spectrum as the initial condition [41],

$$E(k) = C\epsilon^{2/3}k^{-5/3}f_L(kL)f_\eta(k\eta), \quad (2.12)$$

where the Kolmogorov constant $C = 1.5$, and the energy dissipation rate $\epsilon = 0.4$. The function $f_L(kL)$ and $f_\eta(k\eta)$ are the energy spectrum at larger and smaller scales respectively. Here, L is the integral length scale, and η is the Kolmogorov dissipation scale. The form of these functions are given below,

$$f_L(kL) = \left(\frac{kL}{[(kL)^2 + c_L]^{1/2}} \right)^{5/3+p_0}, \quad (2.13)$$

$$f_\eta(k\eta) = \exp(-\beta k\eta), \quad (2.14)$$

$$(2.15)$$

where $c_L = 1.5$, $p_0 = 2$, $\beta = 5.2$, and L is the integral length scale. We obtain the velocity from Eq. 2.12. The phase of Fourier modes for velocity fields is randomly generated.

To get the steady-state flow, we apply a random forcing to the velocity field [214–216]. This scheme was first devised by Carati et al. [216]. The forcing scheme is such that it supplies constant energy with zero kinetic helicity to the flow. The energy supply rate of ϵ is distributed among the n_f number of Fourier modes inside the forcing shell. The forcing amplitude is,

$$\hat{f}(\mathbf{k}) = \frac{\epsilon \hat{\mathbf{u}}(\mathbf{k})}{n_f [\hat{\mathbf{u}}(\mathbf{k}) \cdot \hat{\mathbf{u}}^*(\mathbf{k})]}, \quad (2.16)$$

where (\cdot) is the scalar product operator. Here, the forcing is random in nature, because the velocity $\hat{\mathbf{u}}(\mathbf{k})$ is random in phase.

For the initial condition for simulating rotating turbulent flows, we use the following procedure. We performed a numerical simulation with a 512^3 grid resolution

and forced the system in the wavenumber range $k_f \in [11, 12]$ for three-dimensional (3D) homogeneous and isotropic turbulent flow. The forcing maintains a constant kinetic energy supply rate at $\epsilon = 0.4$ in the flow. We use the steady-state data of fully developed hydrodynamic turbulence as an initial condition for the simulation of rapidly rotating turbulence.

In the next section, we discuss the energy evolution of the system and quantification of the energy spectrum, kinetic energy flux, shell-to-shell energy transfer, and conical energy flux.

2.3 Kinetic energy spectrum

We compute the kinetic energy of the modes inside the shell of unit width and so the kinetic energy of all the modes inside the shell of shell radii k and $k + 1$ is defined as,

$$E(k) = \sum_{k \leq |\mathbf{k}'| < k+1} \frac{1}{2} |\hat{\mathbf{u}}(\mathbf{k}')|^2. \quad (2.17)$$

As mentioned earlier, rotation in 3D turbulence makes the flow anisotropic owing to

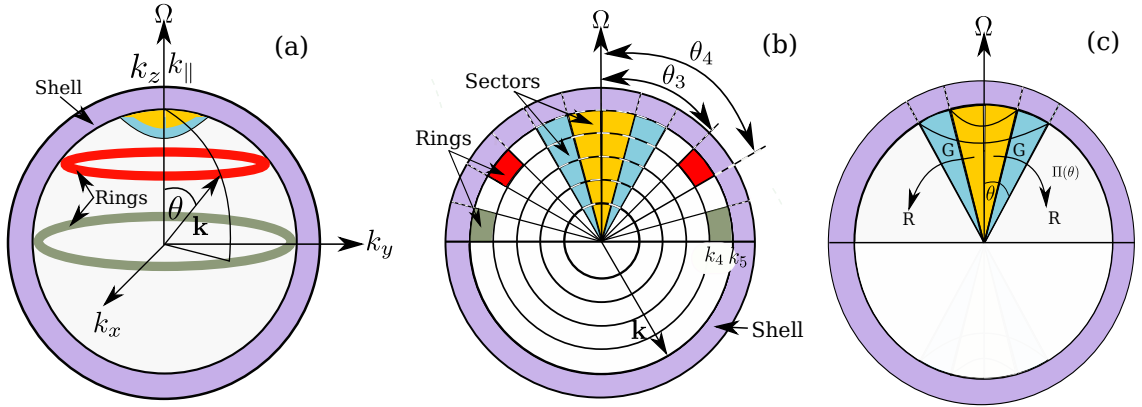


FIGURE 2.2: The plots show the schematic diagram of, (a) ring decomposition in Fourier space, (b) cross-sectional view of shells, sectors and rings, (c) conical energy flux $\Pi(\theta)$: the rate of transfer of energy from the modes inside the cone of semi-vertical angle θ to the modes outside the cone. This figure is adapted from a figure from Ref. [5].

the presence of Coriolis force. In order to quantify this anisotropy in the distribution

of energy in the Fourier modes, we need certain useful mathematical measures. We employ ring spectrum that was first proposed by Teaca et al. [5, 187]. Reddy et al. also used the same technique to study anisotropic energy transfer in MHD [5]. We represent the Fourier space in spherical coordinates and decompose the Fourier space into rings. A ring is defined as the intersection of shells and sectors in Fourier space.

A shell with shell index i in Fourier space—where each point is specified by a vector \mathbf{k} —can be defined as a set, $\text{Shell}(i)$:

$$\text{Shell}(i) := \{ \mathbf{k} : k_{i-1} \leq |\mathbf{k}| < k_i \}, \quad (2.18)$$

where $i \in \mathbb{N}$; and k_{i-1} and k_i are the radii of $(i-1)$ th and i th concentric spheres in the Fourier space. The shells essentially partition the Fourier space into non-overlapping concentric annular regions such that their union is the entire Fourier space under consideration.

The direction of the angular velocity in our system is taken along the z -direction without any loss of generality. Let angle $\theta \in [0, \pi]$ be the angle between the wave vector \mathbf{k} and the z -axis. A sector with sector index j in Fourier space is denoted by $\text{Sector}(j)$ and can be defined as the set [5],

$$\text{Sector}(j) := \left\{ \mathbf{k} : \theta_{j-1} \leq \arccos \left(\frac{k_{\parallel}}{|\mathbf{k}|} \right) < \theta_j \right\}, \quad (2.19)$$

where k_{\parallel} is the component of the wave vector along the direction of the angular velocity, and θ_j is the angle between the z -axis and the corresponding wavevector. The set of all the sectors is another way of partitioning the Fourier space. A sector is essentially the volume between two cones sharing the origin as vertices and the z -axis as their symmetry axes.

Any ring is the intersection between a shell and a sector. In general, a ring of index (i, j) may be defined as [5, 187]:

$$\text{Ring}(i, j) := \{ \mathbf{k} : \mathbf{k} \in \text{Shell}(i) \cap \text{Sector}(j) \}, \quad (2.20)$$

where $i, j \in \mathbb{N}$. For example, in Fig. 2.2(a)-(b), the red-colored region has shell index 5 and sector index 4, so its ring index is $(5, 4)$ and it can be denoted as $\text{Ring}(5, 4)$. In this thesis, we work with exclusively the rings lying inside the angular range from $\theta = 0$ to $\theta = \pi/2$ due to $\theta \rightarrow \pi - \theta$ symmetry. The kinetic energy spectrum of $\text{Ring}(m, \alpha)$ in

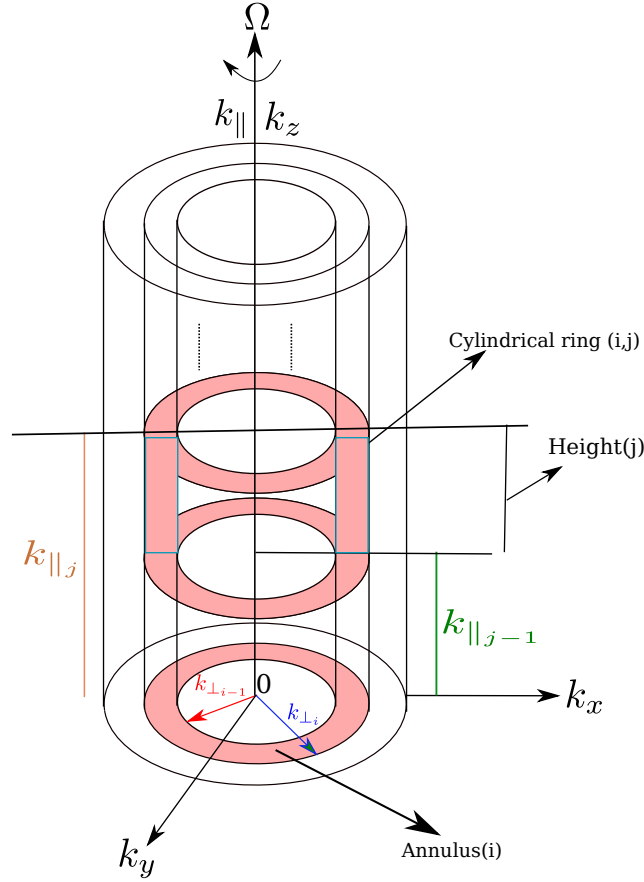


FIGURE 2.3: Schematic diagram of Fourier space decomposed in cylindrical rings.

Fourier space may be defined as,

$$E^{(m,\alpha)}(k, \theta) = \frac{1}{A_\alpha} \sum_{\substack{k_{m-1} < |\mathbf{k}'| \leq k_m \\ \theta_{\alpha-1} < \theta \leq \theta_\alpha}} \frac{1}{2} |\mathbf{u}(\mathbf{k}')|^2, \quad (2.21)$$

where $A_\alpha := |\cos(\theta_\alpha) - \cos(\theta_{\alpha-1})|$ is the normalizing constant that compensate the uneven distribution of modes inside the sectors—a sector consisting of points near the equator contains relatively more modes.

The anisotropic energy spectrum of anisotropic turbulent flow can also be studied in cylindrical co-ordinate in Fourier space. In Fourier space, a cylinder is decomposed into cylindrical rings. A cylindrical ring is defined as the region between two coaxial cylinders with distinct radii and a given height.

A cylindrical ring is specified by ring index (i, j) , where i is the annulus index

and j is the height index (as shown in the figure 2.3).

We define an annulus corresponding to the annulus index i as, $Annulus(i)$:

$$Annulus(i) := \{\mathbf{k} : k_{\perp_{i-1}} < |\mathbf{k}_{\perp}| \leq k_{\perp_i}\}, \quad (2.22)$$

where $i \in \mathbb{N}$, $|\mathbf{k}_{\perp}| = \sqrt{(k_x^2 + k_y^2)}$, $k_{\perp_{i-1}}$ and k_{\perp_i} are the radii of $(i-1)th$ and ith co-axial cylinders with axes along the direction of rotation.

We also define a set of wavevectors with height along the direction of rotation (i.e. k_{\parallel}) corresponding to the height index j as, $Height(j)$:

$$Height(j) := \{\mathbf{k} : k_{\parallel_{j-1}} < k_{\parallel} \leq k_{\parallel_j}\}, \quad (2.23)$$

where $j \in \mathbb{N}$. Here $k_{\parallel} = k_z$ is the component of wavevector along the direction of angular velocity (i.e. along z-axis), and so $k_{\parallel_{j-1}}$ and k_{\parallel_j} are the heights of $(j-1)th$ and jth of the cylinders along the direction of rotation.

Any cylindrical ring is the intersection between an annulus and a height. In general, a cylindrical ring (i, j) contains sets of all wavevectors $\mathbf{k} : \mathbf{k} = \mathbf{k}_{\perp} + k_{\parallel}\hat{z} \in Annulus(i) \cap Height(j)$, where $i, j \in \mathbb{N}$.

The kinetic energy spectrum of the cylindrical ring with ring index (i, j) (see Fig. 2.3) in Fourier space may be defined as,

$$E^{(i,j)}(k_{\perp}, k_{\parallel}) = \sum_{\substack{k_{\perp_{i-1}} < |\mathbf{k}'_{\perp}| \leq k_{\perp_i} \\ k_{\parallel_{j-1}} < k'_{\parallel} \leq k_{\parallel_j}} \frac{1}{2} |\hat{\mathbf{u}}(\mathbf{k}'_{\perp}, k'_{\parallel})|^2. \quad (2.24)$$

where $|\mathbf{k}_{\perp}| = \sqrt{k_x^2 + k_y^2}$, $k_{\parallel} = k_z$ (modes along the direction of rotation), and we assume symmetry along ϕ -direction.

In the next subsection, we discuss the energy transfer due to the nonlinear term in turbulent flow.

2.4 Kinetic energy transfer

In turbulent flows, the energy of a mode is determined by the amount of energy coming to the mode and vice versa, owing to the nonlinear interaction among modes. This transfer of energy is complex in nature due to intricate interaction among the phase of modes participating in nonlinear transfer. Here, we discuss the measures of energy transfer, for example, kinetic energy flux, shell-to-shell energy transfer, ring-to-ring energy transfer, and conical flux [3, 28, 30].

It is insightful to study the energy transfer in detail by computing the mode-to-mode energy transfer in a triad $(\mathbf{k}, \mathbf{p}, \mathbf{q})$, where $\mathbf{k} = \mathbf{p} + \mathbf{q}$ proposed by Dar and Verma [28, 30]. In Fourier space, the mode-to-mode energy transfer, which is the rate of energy transfer from velocity mode $\mathbf{u}(\mathbf{p})$ to velocity mode $\mathbf{u}(\mathbf{k})$ via velocity mode $\mathbf{u}(\mathbf{q})$ acting as a mediator, is given by:

$$S(\mathbf{k}|\mathbf{p}|\mathbf{q}) \equiv \Im[(\mathbf{k} \cdot \mathbf{u}(\mathbf{q}))(\mathbf{u}(\mathbf{p}) \cdot \mathbf{u}^*(\mathbf{k}))]. \quad (2.25)$$

The kinetic energy flux $\Pi(k_0)$ is the rate of transfer of energy from the modes inside the sphere of radius k_0 to the modes outside the sphere in Fourier space. The schematic diagram of the kinetic energy flux is depicted in Fig. 2.4. Dar et al. [28] and Verma [30] proposed a method to compute the kinetic energy flux. The method is as follows,

$$\Pi_{u^>}^u(k_0) = \sum_{|k|>k_0} \sum_{p \leq p_0} S(\mathbf{k}|\mathbf{p}|\mathbf{q}). \quad (2.26)$$

Here,

$$\hat{\mathbf{u}}^>(\mathbf{k}) = \begin{cases} 0 & \text{if } k \leq k_0, \\ \hat{\mathbf{u}}(\mathbf{k}) & \text{if } k > k_0, \end{cases}$$

and,

$$\hat{\mathbf{u}}^<(\mathbf{p}) = \begin{cases} \hat{\mathbf{u}}(\mathbf{p}) & \text{if } p \leq k_0, \\ 0 & \text{if } p > k_0. \end{cases}$$

The sign of this kinetic energy flux, $\Pi_{u^>}^u(k_0)$, indicates whether the transfer of energy is towards the smaller wavenumbers (inverse cascade of kinetic energy) or larger wavenumbers (forward cascade of kinetic energy). The kinetic energy flux does not have information about the detailed nature of energy transfer. The more detailed en-

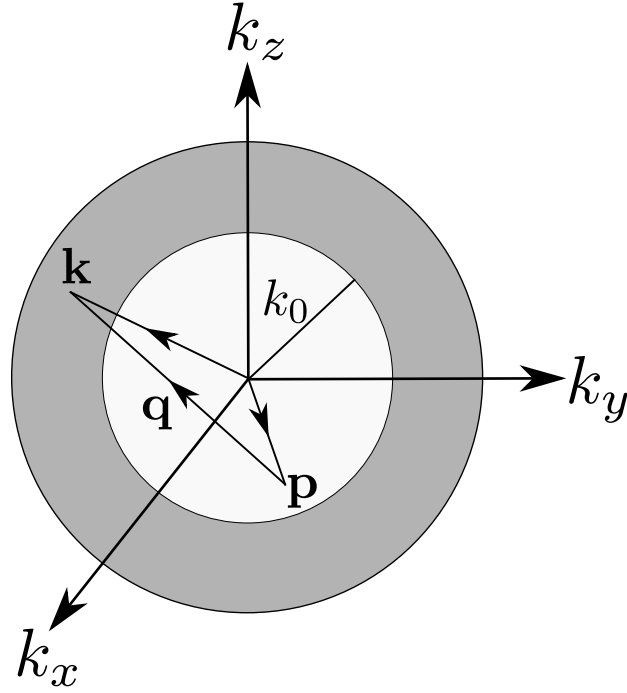


FIGURE 2.4: Schematic diagram for the computation of kinetic energy flux for a sphere of radius k_0 in Fourier space. This figure is adapted from a figure from Ref. [3].

energy transfer is obtained by shell-to-shell energy transfer. The shell-to-shell energy transfer entails the information about the transfer of energy between modes, which may be local or nonlocal. Dar et al. [28] and Verma [30] also proposed a method to capture the local and non-local behavior of energy transfer i.e., shell-to-shell energy transfer. The shell-to-shell energy transfer rate [28, 30, 194],

$$T_n^m = \sum_{\mathbf{k} \in \text{Shell}(n)} \sum_{\mathbf{p} \in \text{Shell}(m)} S(\mathbf{k}|\mathbf{p}|\mathbf{q}), \quad (2.27)$$

from the velocity modes inside $\text{Shell}(m)$ to velocity modes inside $\text{Shell}(n)$. The schematic diagram of shell-to-shell energy transfer is shown in Fig. 2.5.

The shell-to-shell energy transfer provides the information whether the energy transfer is local or nonlocal in nature. However, the shell-to-shell energy transfer does not provide the information about anisotropic energy transfer in the system. In order to quantify the anisotropic behavior of the energy transfer, we employ the ring decomposition of the Fourier space proposed by Teaca et al. [187] to compute ring-to-ring

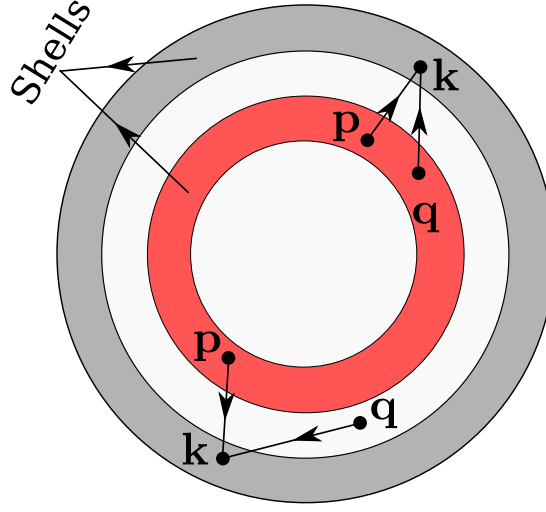


FIGURE 2.5: Schematic diagram for the computation of shell-to-shell energy transfer. This figure is adapted from a figure from Ref. [3].

energy transfer. We also compute the conical energy flux proposed by Reddy et al. [5].

The conical energy flux, $\Pi(\theta)$, is the rate of transfer of energy from the giver/donor modes (say, G) inside the cone of semi-vertical angle θ to the receiver modes (say, R) outside the cone (see Fig. 2.2(c); coloured yellow and cyan). The functional form of the conical energy flux is given by,

$$\Pi(\theta) = \sum_{\mathbf{k} \in R} \sum_{\mathbf{p} \in G} S(\mathbf{k}|\mathbf{p}|\mathbf{q}). \quad (2.28)$$

In order to examine the local or the non-local nature of the energy transfer between the different rings, and also to know about the angular dependent dynamics of the system due to rotation, one needs to investigate the ring-to-ring energy transfer.

The ring-to-ring energy transfer is the rate of transfer of energy from all the velocity modes inside $\text{Ring}(m, \beta)$, say, to all the velocity modes inside $\text{Ring}(n, \alpha)$, say. The mathematical form of the normalized ring-to-ring energy transfer is:

$$T_{(n,\alpha)}^{(m,\beta)} = \frac{1}{A_\alpha A_\beta} \sum_{\mathbf{k} \in \text{Ring}(n,\alpha)} \sum_{\mathbf{p} \in \text{Ring}(m,\beta)} S(\mathbf{k}|\mathbf{p}|\mathbf{q}). \quad (2.29)$$

In the next section, we discuss simulation parameters for decaying and forced rotating turbulence.

2.5 Simulation parameters

We have used pseudo-spectral code Tarang [210,211] to simulate Eqs. 2.4-2.5 with periodic boundary conditions on all the sides of the cubic box. We solve non-dimensionalized equations by expressing length, velocity, and time in the units of $L_0/(2\pi)$, U_0 , and $U_0/(L_0/(2\pi))$ respectively; here L_0 and U_0 are respectively the length scale and the velocity scale of the system. In Eq. (2.4), $\nu \rightarrow \nu/(U_0L_0)$ is nondimensional viscosity, while $\Omega \rightarrow \Omega L_0/U_0$ is the nondimensional angular velocity of the flow.

In our simulations, we have used fourth-order Runge–Kutta method for time-stepping, and Courant–Friedrich–Lewy (CFL) condition to optimize the choice of the time step (Δt) and the 2/3-rule for dealiasing. The simulations have been performed with a grid-resolution of 512^3 and 1024^3 , and rotation rates, $\Omega = 16$ and $\Omega = 32$. The Rossby number and Reynolds number corresponds to $\Omega = 16$ at time frame $t = 155$ are 2515 and 0.002, and $\Omega = 32$ at time frame $t = 56$ are 1736 and 0.007, respectively. The time is taken in units of large eddy turn-over time defined in the above paragraph.

The initial conditions for decaying as well forced rotating turbulence is taken as:

1. In decaying rotating turbulence, we first generate a fully-developed hydrodynamic turbulence without rotation ($\Omega = 0$) with $\nu = 10^{-3}$ on 512^3 grid points with random forcing (see Eq. 2.16) in the wavenumber band (11, 12). The forcing is such that it continuously supplies constant energy with zero kinetic helicity to the flow.

Now we use the steady-state data of the three-dimensional homogeneous isotropic fully-developed hydrodynamic turbulence as an initial condition for the simulation of our rapidly rotating turbulence. Note that such initial conditions have been widely used in earlier simulations of decaying and rotating turbulence [99, 142, 217]. We employ $\Omega = 16$. Note that the (nondimensional) frequency associated with the nonlinearity is $O(1)$, hence our simulation with $\Omega = 16$ is reasonably fast rotating. We carry out simulation of the rotating flow with the same forcing as hydrodynamic simulation for 6 nondimensional time units after which the forcing is turned off. We set $t = 0$ here. The strongly-rotating and decaying simulation starts at this stage, and it is carried out till $t = t_{\text{final}} = 155$ for 512^3 grid. We also carry out simulation of the rotating flow on 1024^3 grid with the same set of parameters and initial conditions. Since 1024^3 simulation is much

more expensive, we end this simulation at $t = 49$ non-dimensional unit of time.

2. For the simulation of the rapidly rotating forced turbulence, we use the steady state data of 3D turbulence with rotation rate $\Omega = 32$ as the initial condition. The 512^3 grid simulation runs upto $t = 56$ non-dimensional units of time. We have used the data corresponding to the time frame $t = 45$ of 512^3 grid resolution as an initial condition for 1024^3 grid. The system evolve up to $t = 3$ eddy turn-over time for 1024^3 grid.

In our all simulations, $k_{max}\eta$ is ensured to be greater than 1.5, where η is the Kolmogorov length scale, and the maximum wavenumber obtained in DNS for a particular grid size is denoted by k_{max} .

To compute energy transfer, for example, kinetic energy flux, shell-to-shell energy transfer, ring-to-ring energy transfer, the Fourier space is decomposed into shells with an inner and outer radii of $Shell(n)$ are k_{n-1} and k_n respectively. The radii of the first three shells are 2, 4, and 8, while the radii of the last two shells are $N/4$, and $N/2$, respectively. The remaining shell in between is logarithmically binned to capture local energy transfer. The radii of the shells in the inertial range are given by the expression,

$$r_i = r_3 \left[\frac{r_n}{16.0} \right]^{\frac{i-1}{n-4}}, \quad (2.30)$$

where r_3 is the radius of 3rd shell and $r_n = N/2$ is the radius of the last shell, where N is the grid resolution along any direction. However, Mininni et al. [79] employed linear binned shells for the calculation of shell-to-shell energy transfer.

In the next section, we summarize this chapter.

2.6 Summary

In this chapter, we have discussed the simulation method, where we showed the computation method implemented in TARANG to compute the statistical quantity like energy spectrum, energy transfer, etc. for rapidly rotating turbulence. We have also discussed the forcing scheme and initial condition implemented in TARANG. In the subsequent chapters, we perform high-resolution simulations using pseudo-spectral code TARANG for rotating turbulence and discuss the results obtained from it.

Chapter 3

Coherent structures and modeling of energy spectrum of decaying rotating turbulence

We put our faith in the tendency for dynamical systems with a large number of degrees of freedom, and with coupling between those degrees of freedom, to approach a statistical state which is independent (partially, if not wholly) of the initial conditions.

– G.K. Batchelor

As mentioned earlier, the rotating turbulence is an omnipresent phenomenon observe in nature. The Rossby number of oceanic flow, flow inside the Earth's core, oceanic tides, and tornadoes are $10^{-2} - 10^2$, $10^{-5} - 10^{-7}$, $10^{-4} - 10^{-2}$, and 10^3 , respectively. The Rossby number deep inside the Sun is $Ro \approx 0.2$, and it helps to sustain the dynamo process inside the Sun's core. The rotation affects the larger-scale motion of the system. The kinetic energy spectrum gets steeper due to rotation [122]. In this chapter, we describe the results obtained from numerical simulation for $\Omega = 16$ on the grid resolution of 512^3 and 1024^3 . Here study is done exclusively for decaying rotating turbulence.

We discuss the time evolutions of different parameters of the system like the integral length scale, the Rossby number, the Reynold number, the kinetic energy, etc.

Our simulations ran up to 155 eddy turn-over time for 512^3 grid resolution and up to $t = 49$ for 1024^3 grid resolution. We show that in rapidly rotating decaying turbulence, columnar structures are formed in the system; and $(\pm 1, 0, 0)$ and $(0, \pm 1, 0)$ are the most energetic modes of the system. These modes contain around 86 percent of the total energy of the system. We model the kinetic energy spectrum of the decaying rotating turbulent systems in the dissipation range. This chapter is based on the results published in Physics of Fluids [184].

This chapter is organized as follows: In Sec. 3.1 we describe energy equations of the system and the formalism of the phenomenological model in the dissipation range. In the subsequent sections, we discuss the results of numerical simulations for rotating decaying turbulence.

3.1 Phenomenology of rotating turbulence

The Coriolis force drives the perpendicular component of the velocity field, $\mathbf{u}_\perp = u_x \hat{x} + u_y \hat{y}$; this is one of the reasons why the rapidly rotating flows tend to be quasi-2D with $u_\perp \gg u_\parallel$ (u_\parallel is the magnitude of the velocity component along z direction) [34–37, 126, 218]. For rapid rotation, the flow tends to be strongly quasi two-dimensional, i.e., $u_z \ll u_\perp$. The Taylor–Proudman theorem [24] predicts such structures in the linear regime. But in the nonlinear regime, structure formation is due to the inverse cascade of energy. Note that in the linear regime, $\text{Re} = 0$, and hence $\Pi(k) = 0$. However, in the nonlinear regime, as will be shown in our numerical simulations, large-scale vortices are formed due to strong nonlinear effects. Therefore we study \mathbf{u}_\perp by taking a horizontal cross section of the flow profile. It is best to relate the 2D-sectional field with 2D hydrodynamic theory of Kraichnan [81]. It is important however to keep in mind that the rotating flow is more complex due to the u_z component that couples with \mathbf{u}_\perp . External forcing is absent in decaying turbulence, but small wavenumber modes supply energy to the large wavenumber modes. Therefore, decaying 2D turbulence and rapidly rotating turbulence exhibit forward enstrophy cascade [219].

The evolution equation of one dimensional energy spectrum for decaying rotating turbulence, which is defined as $E(k) = \sum_{k-1 < k' \leq k} \frac{1}{2} |\mathbf{u}(\mathbf{k}')|^2$ in Fourier space, is given by,

$$\frac{\partial}{\partial t} E(k, t) = -\frac{\partial}{\partial k} \Pi(k, t) - 2\nu k^2 E(k, t), \quad (3.1)$$

where $\Pi(k, t)$ is the energy flux emanating from a wavenumber sphere of radius k at time t . For a steady or a quasi-steady state, $\partial E(k)/\partial t \approx 0$, hence

$$\frac{d}{dk} \Pi(k) = -2\nu k^2 E(k). \quad (3.2)$$

The energy flux and the spectrum, $\Pi(k)$ and $E(k)$, are two unknown functions whose solution cannot be obtained from a single equation, Eq. 3.2. For 3D hydrodynamic turbulent flows, Pao [56] assumed that $E(k)/\Pi(k)$ is independent of ν , and that it depends only on ϵ and k . Under these assumptions, we obtain the following solution for the above:

$$E(k) = K_{\text{Ko}} \epsilon^{2/3} k^{-5/3} \exp\left(-\frac{3}{2} K_{\text{Ko}} (k/k_\eta)^{4/3}\right), \quad (3.3)$$

$$\Pi(k) = \epsilon \exp\left(-\frac{3}{2} K_{\text{Ko}} (k/k_\eta)^{4/3}\right), \quad (3.4)$$

The Pao model has been validated numerically by many authors [220–222]. Since the rapidly rotating flows tend to be quasi-2D, it is important to briefly describe the phenomenology of 2D hydrodynamic turbulence. Kraichnan [81] had reported that the two-dimensional hydrodynamic turbulence has dual spectrum—the energy exhibits inverse cascade for $k < k_f$, while the enstrophy $E_\omega^{(2D)} = \int d\mathbf{r} \omega^2 / 2 = \int d\mathbf{r} |\nabla \times \mathbf{u}|^2 / 2$ exhibits forward cascade for $k > k_f$, where k_f is the forcing wavenumber. Kraichnan [81] showed that for $k < k_f$,

$$E^{(2D)}(k) = K'_{\text{Ko}} [\Pi^{(2D)}(k)]^{2/3} k^{-5/3} \quad (3.5)$$

with $\Pi^{(2D)}(k) = \text{const} < 0$. However, for $k > k_f$,

$$E_\omega^{(2D)}(k) = K_\omega [\Pi_\omega^{(2D)}(k)]^{2/3} k^{-1} \quad (3.6)$$

with $\Pi_\omega^{(2D)}(k) = \text{const} > 0$. Here $\Pi^{(2D)}(k)$ and $\Pi_\omega^{(2D)}(k)$ are the energy and enstrophy fluxes respectively, K'_{Ko} is Kolmogorov's constant for 2D, K_ω is the proportionality constant for the constant enstrophy flux regime.

In the subsequent discussion, we will show that for strongly-rotating turbulence, the intermediate and small-scale structures contain very small amount of energy. Also, since the flow is quasi-2D, we study the enstrophy and energy of a horizontal cross section perpendicular to the rotation axis. The evolution equation for the enstrophy spectrum is

$$\frac{\partial}{\partial t} E_{\omega}^{(2D)}(k, t) = -\frac{\partial}{\partial k} \Pi_{\omega}^{(2D)}(k, t) - 2\nu k^2 E_{\omega}^{(2D)}(k, t), \quad (3.7)$$

where $\Pi_{\omega}^{(2D)}(k, t)$ is the enstrophy flux for the 2D flow of a horizontal cross-section. For a steady or a quasi-steady state, $\partial E_{\omega}^{(2D)}(k, t) / \partial t \approx 0$, hence

$$\frac{d}{dk} \Pi_{\omega}^{(2D)}(k) = -2\nu k^2 E_{\omega}^{(2D)}(k). \quad (3.8)$$

For the intermediate and small scales, following Pao [56], we assume that $E_{\omega}^{(2D)}(k) / \Pi_{\omega}^{(2D)}(k)$ is independent of ν , and it depends only on the enstrophy dissipation rate, ϵ_{ω} , and k . Under this ansatz, $E_{\omega}^{(2D)}(k)$ and $\Pi_{\omega}^{(2D)}(k)$ are given by

$$E_{\omega}^{(2D)}(k) = C \epsilon_{\omega}^{2/3} k^{-1} \exp\left(-C(k/k_d)^2\right), \quad (3.9)$$

$$\Pi_{\omega}^{(2D)}(k) = \epsilon_{\omega} \exp\left(-C(k/k_d)^2\right), \quad (3.10)$$

where

$$k_d = \frac{\epsilon_{\omega}^{1/6}}{\sqrt{\nu}} \quad (3.11)$$

is the enstrophy dissipation wavenumber, and ϵ_{ω} is the enstrophy dissipation rate.

For strongly-rotating turbulence discussed in this chapter, $\text{Re} \gg 1$, and the flow is quasi-2D. In this chapter we show some subtle differences between the 2D hydrodynamic turbulence and the rotating turbulence. We show that Eq. 3.9 and Eq. 3.10 match quite well with our numerical results apart from prefactors. These results will be discussed in Sec. 3.4.

We also remark that in the linear regime where nonlinearity is absent,

$$\frac{\partial}{\partial t} E_{\omega}^{(2D)}(k, t) = -2\nu k^2 E_{\omega}^{(2D)}(k, t), \quad (3.12)$$

which has solution of the form [81],

$$E_{\omega}^{(2D)}(k, t) = E_{\omega}^{(2D)}(k, 0) \exp(-2\nu k^2 t). \quad (3.13)$$

More importantly, the enstrophy flux must be zero for this case. This prediction is not applicable to our numerical results due to the presence of the nonlinear interactions, however weak, and nonzero enstrophy flux.

In the following section, we compare the phenomenology developed in this section with numerical results.

3.2 Evolution of system parameters

We conducted a numerical simulation of the decaying rotating turbulence with rotation rate $\Omega = 16$ for grid-resolutions of 512^3 and 1024^3 . The parameters of the simulation are tabulated in Table 3.1.

Parameters	$t = 49$ ($N = 512^3$)	$t = 148$ ($N = 512^3$)	$t = 49$ ($N = 1024^3$)
E	0.13	0.08	0.13
L	3.11	5.40	3.10
Re	3003	1918	2989
Ro	0.005	0.003	0.005
k_Ω	1888	4300	1900
k_η	32	21	32
A	228	596	241

TABLE 3.1: Parameters of the direct numerical simulations (DNS): List of total energy E ; integral length scale L ; Reynolds number Re; Rossby number Ro; Zeman wavenumber k_Ω ; Kolmogorov dissipation wavenumber k_η ; and anisotropy ratio A at $t = 49, 148$ for 512^3 grids, and at $t = 49$ for 1024^3 grids.

In Fig. 3.1 we show temporal evolution of various quantities for 512^3 (blue) and 1024^3 (red) grids. Figure 3.1(a) exhibits the evolution of total energy, $E = \int dr u^2/2$, that decays from 0.8 to approximately 0.08 following a power law $E \sim t^{-0.33}$. This result is in general agreement with those of Thiele and Muller [113] and Baqui and Davidson [114]. Using Eq. 1.36, we compute integral length scale. In Fig. 3.1(b) we plot the integral length scale.

We observe that beyond $t = 100$, $L \approx 5.43$, which is close to the box size (2π), thus signalling formation of large scale structures. As shown in Fig. 3.1(c), the Reynolds number $\text{Re} = u_{\text{rms}}L_0/\nu$ is in the range of 2000 to 3000. For the computation of Re

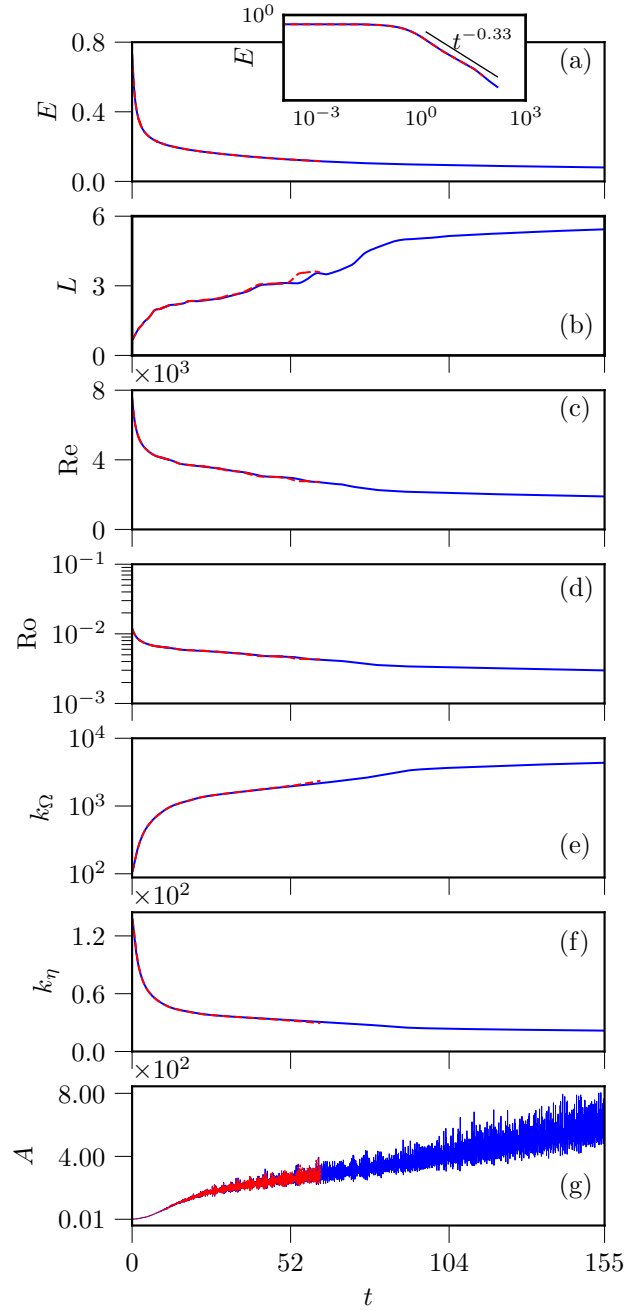


FIGURE 3.1: For 1024^3 (red dashed) and 512^3 (blue) grids simulation with $\Omega = 16$, variation of characteristic system parameters with time t : (a) the total energy $E(t)$, (b) the integral length scale, L , (c) the Reynolds number, Re , (d) the Rossby number, Ro , (e) the Zeman wavenumber, k_{Ω} , (f) the Kolmogorov dissipation wavenumber, k_{η} , and (g) anisotropy of the system A . The inset in subfigure (a) is log-log plot showing $E(t) \sim t^{-0.33}$.

and Ro we employ $L_0 = 2\pi$ (box size), and u_{rms} as the rms speed, which is given by $\left(2 \int_0^{k_{\text{max}}} E(k) dk\right)^{1/2}$.

We compute the Rossby number Ro using Eq. 1.9 and plot its temporal variation in Fig. 3.1(d). The figure shows that Ro varies from 10^{-2} to 3×10^{-3} . Thus, Rossby number at large times is quite small for our simulations. Hence, the Coriolis force dominates the nonlinear term of Eq. 1.6. We remark that some researchers [114] report Ro based on the initial velocity of decaying turbulence. However our definition is based on the instantaneous velocity, thus Ro of Fig. 3.1(d) is that of instantaneous flow.

We also compute the Zeman wavenumber k_Ω using Eq. 1.52, and the Kolmogorov's wavenumber k_η using $(\epsilon/\nu^3)^{1/4}$, and plot them in Fig. 3.1(e) and Fig. 3.1(f), respectively. We observe that in the asymptotic regime, $k_\Omega \gg 1$ indicating dominance of Coriolis force. We observe that $k_\Omega > k_{\text{max}}$, where $k_{\text{max}} = N/2$ with N as the grid size. Hence the above estimate of k_Ω appears to be quite ambiguous. Note that the derivation of k_Ω using Eq. 1.52 assumes that for large k 's, the turbulence is isotropic and $E(k) \sim k^{-5/3}$, which is not the case for our simulations of strongly-rotating turbulence (to be discussed in Sec. 3.4). We show that strongly rotating turbulence makes the flow quasi-2D. Hence, strictly speaking, Eq. 1.52 cannot be employed to compute k_Ω .

In Fig. 3.1(g) we plot the anisotropy parameter

$$A = \frac{E_\perp}{2E_\parallel} \quad (3.14)$$

as a function of time. Here, $E_\perp = E_x + E_y$, and $E_\parallel = E_z$ [with $E_x = \int (u_x^2/2) d\mathbf{r}$, $E_y = \int (u_y^2/2) d\mathbf{r}$, and $E_z = \int (u_z^2/2) d\mathbf{r}$]. We observe that $A \gg 1$ indicating quasi-2D nature of the flow. We have also tabulated the values of E , L , Re , Ro , k_Ω , k_η , and A in Table 3.1 at $t = 49, 148$ for 512^3 grid simulations, and at $t = 49$ for 1024^3 grid simulation respectively.

In the next section we show that the strongly-rotating flow is dominated by the columnar structures.

3.3 Columnar structures and associated Fourier modes

In the earlier section we showed that the global parameters like the integral length scale and the anisotropy parameter indicate presence of large scale structures. In this Section we describe these structures along with their associated Fourier modes.

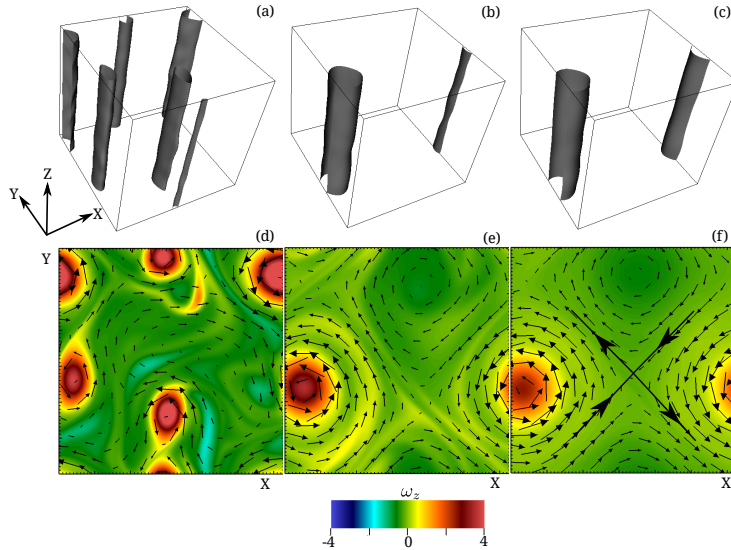


FIGURE 3.2: For the rapidly rotating decaying turbulence on 512^3 grid: The top panel exhibits the isosurfaces of the magnitude of vorticity $|\omega|$ at (a) $t = 49$, (b) $t = 98$, and (c) $t = 148$. The bottom panel shows velocity vector plot superposed with the density plot for ω_z for the horizontal cross section at $z = \pi$ at (d) $t = 49$, (e) $t = 98$, and (f) $t = 148$. Note that (f) contains only one vortex that appears to be split in two due to the periodic boundary conditions.

We investigate the large scale structures by studying the flow profile in real space. In Fig. 3.2(a)-3.2(c), we exhibit the contour plots of the magnitude of the vorticity field, $|\omega|$, at $t = 49$, 98, and 148. These figures demonstrate existence of strong vortical structures. To decipher the flow profiles of these columns, we take horizontal cross section of the flows at $z = \pi$, and present the density plots of ω_z superposed with the vector plot of $\mathbf{u}_\perp = u_x \hat{x} + u_y \hat{y}$. At $t = 49$ we observe four cyclonic vortices that have anticlockwise sense of rotation [see Fig. 3.2(d)]. Note the periodicity of the box. Subsequently these vortices merge and form a single cyclonic vortex, as shown in Fig. 3.2(c) and Fig. 3.2(f). In a periodic box these vortices reside on a lattice along with weak anti-cyclonic vortices. These features are quite similar to those in 2D hydrodynamic turbulence [219].

The cyclonic and anti-cyclonic vortices are separated by a *saddle*, which is symbolised by a cross in Fig. 3.2(f). Morize *et al.* [122] and Staplehurst *et al.* [13] observed cyclonic/anti-cyclonic asymmetry in experiments, while van Bokhoven *et al.* [123] quantified the asymmetry between cyclonic and anti-cyclonic by studying skewness of vertical vorticity. Smith and Lee [112] argued that the cyclonic/anti-cyclonic asymmetry arise due to nonlinear interactions near resonance.

We remark that the size of the asymptotic (at large time) flow structures described above are proportional to the box size. We demonstrate this feature in Appendix A.1 by simulating rotating turbulence in two boxes of sizes $(2\pi)^3$ and $(4\pi)^3$. These results show that the Fourier modes and their interactions are independent of the box size.

When we compare the flow structures of Figs. 3.2(e)-3.2(f) with those found in two-dimensional Hamiltonian dynamics, the cross and the centres of the vortices of Fig. 3.2(f) correspond to the *saddle* and the *centres*. This similarity is due to the divergence-free condition of the velocity field that yields

$$\nabla \cdot \mathbf{u}_\perp = 0 \implies \frac{\partial \dot{x}}{\partial x} + \frac{\partial \dot{y}}{\partial y} = 0, \quad (3.15)$$

which is analogous to the equation for the conservation of phase space area of a two-dimensional Hamiltonian system [223]. Note that $u_z \ll u_\perp$, hence we treat our system as two-dimensional for the above discussion.

The emergence of large scale structures in the flow can be quantified using the energy contents of small wavenumber Fourier modes, which are listed in Table 3.2. Evidently, in the asymptotic regime ($t = 148$), the Fourier mode $\mathbf{k} = (k_x, k_y, k_z) = (1, 0, 0)$ and $(0, 1, 0)$ are the most dominant modes, with the other strong Fourier modes being $(1, 1, 0)$ and $(-1, 1, 0)$. Note that we do not list the energies of $-\mathbf{k}$ modes because $\mathbf{u}(-\mathbf{k}) = \mathbf{u}^*(\mathbf{k})$. Hence, the energies $E(-1, 0, 0) = E(1, 0, 0)$ and $E(0, -1, 0) = E(0, 1, 0)$. When we add the energies of $(\pm 1, 0, 0)$ and $(0, \pm 1, 0)$, we observe that they contain approximately 80% of the total energy. These modes form a strong set of 2D vortices, as discussed in Appendix A.2 and Fig. A.2. The nonlinear dynamics of these modes is very interesting, and it may shed light on the cyclone-anticyclone antisymmetry in the presence of rotation.

At $t = 148$, the sum the energies of the 18 dominant modes listed in Table 3.2 and those of their complex conjugate partners is approximately 98%. These modes lie

TABLE 3.2: For rapidly rotating turbulence on 512^3 grid at $t = 4, 49, 148$, the energy contents of the dominant modes as percentage of the total energy. Note that $\mathbf{u}(-k_x, -k_y, 0)$, not listed in the table, has the same energy contents as that of $\mathbf{u}(k_x, k_y, 0)$. In the table, $E_{\text{mode}} = |u(\mathbf{k})|^2/2$. For the modes $(0, 1, 0)$ and $(1, 0, 0)$, E_{mode}/E increases with time indicating strengthening of the vortical structures with time.

Mode (k_x, k_y, k_z)	E_{mode}/E (%) $t = 4$	E_{mode}/E (%) $t = 49$	E_{mode}/E (%) $t = 148$
(0, 1, 0)	0.04	3.45	22.12
(1, 0, 0)	1.21	7.34	20.79
(1, 1, 0)	0.60	6.20	1.88
(-1, 1, 0)	0.32	1.75	1.66
(2, 1, 0)	0.65	1.60	0.47
(2, -1, 0)	1.08	2.17	0.44
(-2, 1, 0)	1.08	2.17	0.44
(1, 2, 0)	0.74	1.02	0.41
(1, -2, 0)	0.50	1.92	0.40
(2, -2, 0)	0.38	1.23	0.11
(-3, 0, 0)	0.68	0.36	0.10
(2, 2, 0)	0.52	0.96	0.10
(-1, -3, 0)	1.70	0.54	0.05
(3, 1, 0)	0.29	1.04	0.05
(-3, 1, 0)	2.80	0.19	0.05
(3, -2, 0)	0.45	0.19	0.02
(-2, -3, 0)	1.67	0.26	0.02
(-3, -2, 0)	0.89	0.04	0.02
Total %:	13.084	32.43	49.13

within the sphere of radius 4. Hence, modes in the intermediate and small scales contain very small amount of energy. This result has a strong consequence on the energy and enstrophy spectra of the strongly-rotating turbulence, which will be discussed in Sec. 3.4.

In the following discussion we argue why the small wavenumber modes become strong in rapidly rotating turbulence. The strong vortical structures of the flow indicate quasi-2D nature of the flow. This observation is reinforced by the fact that $A = E_{\perp} / (2E_{\parallel}) \gg 1$ [see Fig. 3.1(g)]. The flow become quasi-2D because of the Coriolis force that is active in the perpendicular plane (x, y) , as well as due to the inverse cascade of the kinetic energy from small scales (large k) to large scales (small k). This is in contrast to the emergence of the Taylor columns in the linear limit, as predicted by the Taylor–Proudman theorem; the energy transfer is absent all together in the linear limit.

Let us now quantify the above observations using the mode-to-mode energy transfers and the energy flux. First we describe the energy transfers among the large scale Fourier modes. Dar *et al.* [28] and Verma [30] showed that for an interacting triad of fluid flow $(\mathbf{k}', \mathbf{p}, \mathbf{q})$ that satisfies the relation $\mathbf{k}' + \mathbf{p} + \mathbf{q} = 0$, the rate of energy transfer from mode $\mathbf{u}(\mathbf{p})$ to mode $\mathbf{u}(\mathbf{k}')$ with mode $\mathbf{u}(\mathbf{q})$ acting as a mediator is

$$S(\mathbf{k}'|\mathbf{p}|\mathbf{q}) = -\text{Im}[(\mathbf{k}' \cdot \mathbf{u}(\mathbf{q}))(\mathbf{u}(\mathbf{p}) \cdot \mathbf{u}(\mathbf{k}'))]. \quad (3.16)$$

To investigate the growth of the large scale structures, we study the energy transfers among the small wavenumber modes listed in Table 3.2. Figure 3.3 exhibits some of the dominant interacting triads involving small k Fourier modes. Note that a complete graph with N modes would contain approximately $N(N - 1)/2$ edges, which is quite large for $N \sim 10$. Hence we show only some of the representative energy transfers. The numbers above the arrows represent the energy transfers. The most dominant energy transfer is in the triad $[\mathbf{k}' = (1, 1, 0), \mathbf{p} = (-1, 0, 0), \mathbf{q} = (0, -1, 0)]$ with the mode $\mathbf{u}(-1, 0, 0)$ supplying approximately 136×10^{-5} units of energy to the mode $\mathbf{u}(1, 1, 0)$. We observe that the dominant energy transfers are $(-1, 0, 0) \rightarrow (1, 1, 0) \rightarrow (0, -1, 0) \rightarrow (-1, 1, 0) \rightarrow (-1, 0, 0)$. Thus, the four modes $(1, 0, 0), (0, 1, 0), (1, 1, 0), (-1, 1, 0)$ play a critical role in the energy transfers in rotating turbulence. These issues will be studied in more detail in future. Figure 3.3 also exhibits other dominant energy transfers, but these transfers are order of magnitude smaller than those discussed above.

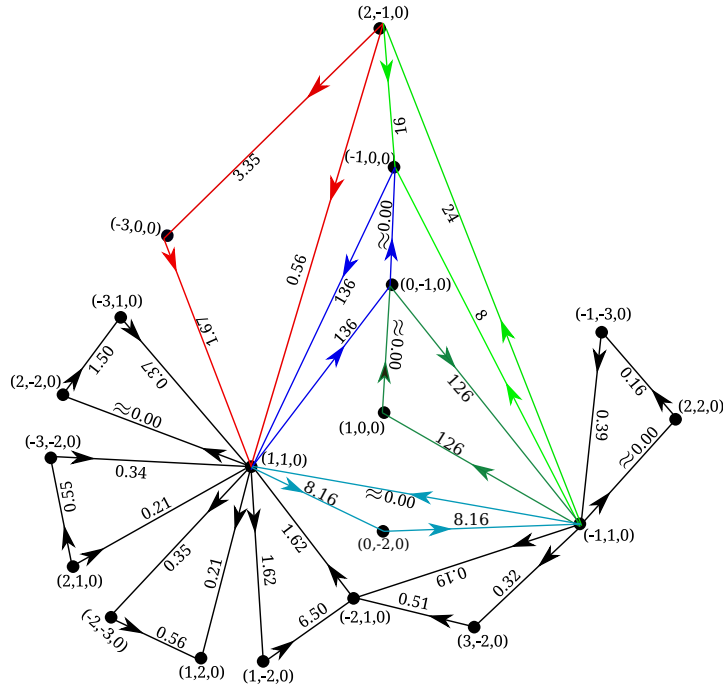


FIGURE 3.3: For the rapidly rotating decaying simulation on 512^3 grid, the energy transfers $S(\mathbf{k}'|\mathbf{p}|\mathbf{q})$ for some of the dominant triads averaged over five eddy turnover time from $t = 148$ to 152 . The numbers above the arrows are $S(\mathbf{k}'|\mathbf{p}|\mathbf{q}) \times 10^5$ for convenient description. The most dominant energy transfers are in the triad $[(-1,0,0), (1,-1,0), (0,-1,0)]$.

After the aforementioned discussion on the large scale structures and their associated Fourier modes, in the next section we present the energy and enstrophy spectra and fluxes of our system.

3.4 Energy and enstrophy fluxes and spectra

The energy spectrum and flux provide valuable information about the flow. In this section we compute these quantities and study their features.

We compute the energy flux at $t = 4, 49$ and 148 using the following formula [30]:

$$\Pi(k_0) = \sum_{k' > k_0} \sum_{p \leq k_0} S(\mathbf{k}' | \mathbf{p} | \mathbf{q}), \quad (3.17)$$

where k_0 is the radius of the wavenumber sphere from whom the flux is being computed, $S(\mathbf{k}' | \mathbf{p} | \mathbf{q})$ is defined in Eq. 3.16, and $\mathbf{k}' + \mathbf{p} + \mathbf{q} = \mathbf{0}$. We compute the energy flux at $t = 4, 49, 148$ using the 512^3 and 1024^3 grid data. These results are plotted in Fig. 3.4(a) and Fig. 3.4(c) for $t = 4$ (magenta), $t = 49$ (green) and 148 (red) of 512^3 grid simulation, and for $t = 4$ (blue dashed) and 49 (cyan) of 1024^3 grid simulation. We observe a significant inverse cascade of kinetic energy at early stages. As time progresses, the kinetic energy flux becomes weaker and gets concentrated in the wavenumber band $k \in [1, 8]$. This feature is compatible with the strongly vortical quasi-2D structure of the flow. Ours is a decaying simulation, so we expect the inverse energy cascade regime to be narrower, and the forward enstrophy cascade regime to be effective for a larger wavenumber range. For this reason, it is more appropriate to study the enstrophy spectrum and flux, for which we employ the data obtained from horizontal cross sections at $z = \pi/2, \pi$, and $3\pi/2$.

We compute the enstrophy flux of the 2D velocity field \mathbf{u}_\perp at the planes $z = \pi/2, \pi$, and $3\pi/2$ using

$$\Pi_\omega^{(2D)}(k_0) = \sum_{k > k_0} \sum_{p \leq k_0} S^{\omega\omega}(\mathbf{k}' | \mathbf{p} | \mathbf{q}), \quad (3.18)$$

where

$$S^{\omega\omega}(\mathbf{k}' | \mathbf{p} | \mathbf{q}) = -\text{Im}[(\mathbf{k} \cdot \mathbf{u}_\perp(\mathbf{q}))\omega_z(\mathbf{p})\omega_z(\mathbf{k}')] \quad (3.19)$$

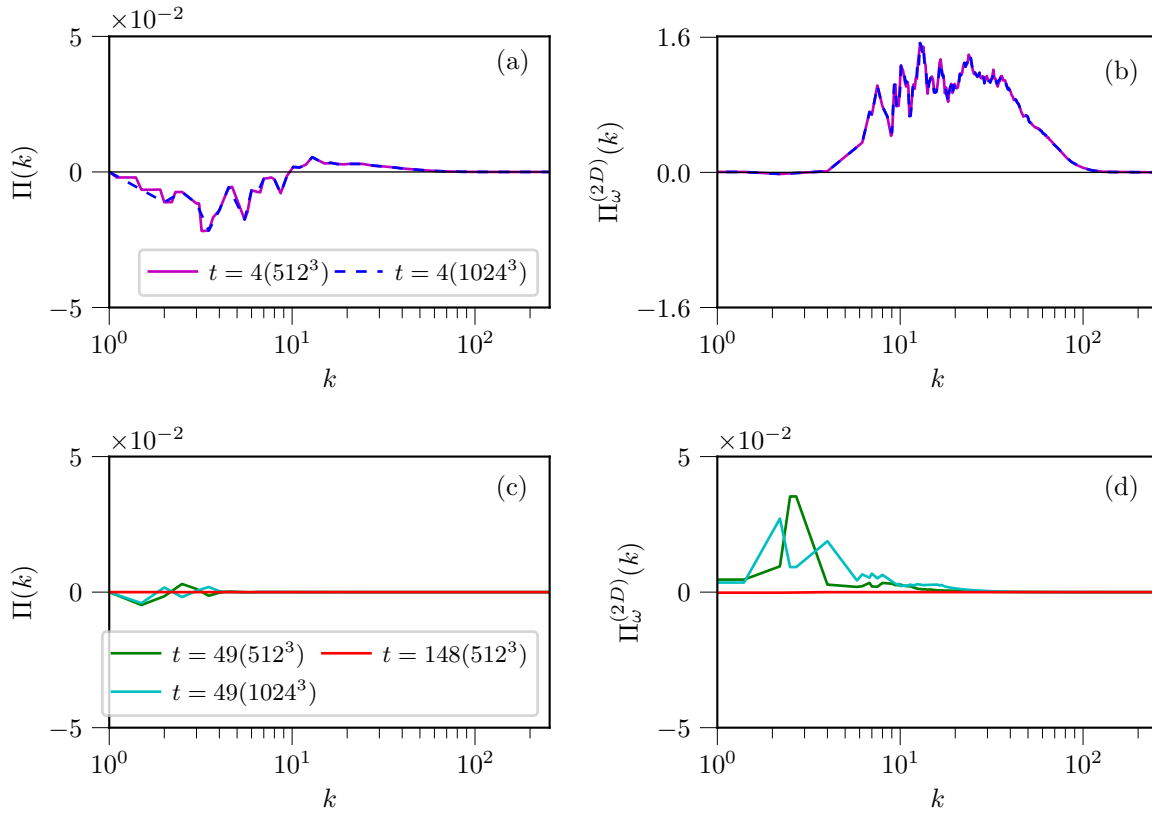


FIGURE 3.4: Kinetic energy flux $\Pi(k)$ and enstrophy flux $\Pi_\omega^{(2D)}(k)$ for rapidly rotating decaying turbulence. (a) $\Pi(k)$ of 3D velocity field for 512^3 (magenta) and 1024^3 (blue dashed curve) grids at $t = 4$. (b) $\Pi_\omega^{(2D)}(k)$ for the 2D cross section at $z = \pi$. Figure (b) has the same color convention as (a). (c) $\Pi(k)$ at $t = 49$ (green), and $t = 148$ (red) for the grid resolutions of 512^3 and at $t = 49$ (cyan) for 1024^3 grids. (d) $\Pi_\omega^{(2D)}(k)$ for 2D cross section at $z = \pi$. Figure (d) has the same color convention as (c). Note that $\Pi_\omega^{(2D)}(k)$ is significant, but $\Pi(k)$ is negligible. Note: The x-scales are in log.

represents the enstrophy transfer from mode $\omega_z(\mathbf{p})$ to mode $\omega_z(\mathbf{k})$ with mode $\mathbf{u}_\perp(\mathbf{q})$ acting as a mediator. Note that $\mathbf{u}_\perp = u_x\hat{x} + u_y\hat{y}$ and $\omega_z(\mathbf{k}) = [i\mathbf{k} \times \mathbf{u}(\mathbf{k})]_z$. For the cross section at $z = \pi$, Fig. 3.4(b) and Fig. 3.4(d) illustrate the plots $\Pi_\omega^{(2D)}(k)$ vs. k at $t = 4, 49, 148$ for the grid resolution of 512^3 , and at $t = 4, 49$ for the grid resolution of 1024^3 . For 512^3 and 1024^3 grids at the same time, the energy and enstrophy fluxes are equal, which is consistent with the fact that our results are grid-independent.

The enstrophy flux is positive definite, but it is not constant in a significant wavenumber band, in contrast to 2D hydrodynamic turbulence for which $\Pi_\omega^{(2D)}(k)$ is constant in the inertial range and then it decreases after $k = k_d$ [219]. The steepening of $\Pi_\omega^{(2D)}(k)$ in strongly-rotating turbulence is due to the viscous effects, as in Eq. 3.10, and due to energy transfer from \mathbf{u}_\perp to u_z , analogous to that in quasi-static MHD [5, 33]; this is in contrast to constant $\Pi_\omega^{(2D)}(k)$ in hydrodynamic two-dimensional turbulence for $k > k_f$.

Now let us focus on the time frames $t = 49, 148$ when the coherent columnar structures are well developed and strong. For these times, in Fig. 3.5, we plot $kE_\omega^{(2D)}(k)$ and $\Pi_\omega^{(2D)}(k)$ vs. k in semi-log scale for $z = \pi/2, \pi$, and $3\pi/2$ planes. In rotating turbulence, $\Pi_\omega^{(2D)}(k)$ starts to decrease at small k itself because the enstrophy dissipation wavenumber, k_d , is quite small (see Table III). We compute the enstrophy dissipation wavenumber k_d using Eq. 3.11. It is difficult to estimate ϵ_ω of Eq. 3.9 because we do not have a band of wavenumbers where $\Pi_\omega^{(2D)}(k)$ is constant. In this chapter, we compute ϵ_ω using Eq. 3.10 by identifying the neck of the wavenumber range from where $\exp(-C(k/k_d)^2)$ spectrum starts. If the wavenumber at the neck is k_* , then using Eq. 3.10,

$$\epsilon_\omega = \Pi_\omega^{(2D)}(k_*) \exp(C(k_*/k_d)^2). \quad (3.20)$$

Incidentally we observe that k_* is approximately twice of Kolmogorov's wavenumber, k_η . We compute C using linear regression analysis. The values of k_d , ϵ_ω , and C are tabulated in Table 5.1. In Fig. 3.5, we plot the best fits to the enstrophy flux as dashed black curves [see Eq. 3.10]. We observe that the above equation describes the numerical data very well. Also note that $\Pi_\omega^{(2D)}(k)$ of 512^3 and 1024^3 grids almost overlap on each other. Hence, to contrast the two plots, we multiply $E(k)$ and $\Pi_\omega^{(2D)}(k)$ of 1024^3 grid with a factor $1/100$ to differentiate the two plots.

Motivated by the above observations, we model the enstrophy spectrum $E_\omega^{(2D)}(k)$ using Eq. 3.9. As shown in Fig. 3.5, we observe the numerical results to be in very good agreement with the model of Eq. 3.9. The red and the green curves in the Fig. 3.5 represent $kE_\omega^{(2D)}(k)$ and $\Pi_\omega^{(2D)}(k)$ for 512^3 resolution at $t = 49$ and $t = 148$ respectively,

TABLE 3.3: For the rapidly rotating decaying turbulence, we take the instantaneous 2D velocity field on the horizontal cross sections at $z = \pi/2, \pi$, and $3\pi/2$. List of the enstrophy dissipation rate, ϵ_ω , the enstrophy dissipation wavenumber, k_d , and constant C . These parameters are listed in the table at time $t = 49$ for 512^3 and 1024^3 , and $t = 148$ for 512^3 .

Grid	t	z	k_d	$\epsilon_\omega \times 10^5$	$C \times 10^2$
512^3	49	$\pi/2$	6.0	4.8	(2.73 ± 0.04)
512^3	49	π	6.0	4.9	(2.76 ± 0.04)
512^3	49	$3\pi/2$	6.0	4.9	(2.74 ± 0.04)
1024^3	49	$\pi/2$	6.6	8.4	(3.00 ± 0.02)
1024^3	49	π	6.6	8.7	(3.03 ± 0.02)
1024^3	49	$3\pi/2$	6.6	8.2	(2.98 ± 0.02)
512^3	148	$\pi/2$	2.7	0.04	(2.45 ± 0.05)
512^3	148	π	2.7	0.04	(2.51 ± 0.05)
512^3	148	$3\pi/2$	2.7	0.04	(2.48 ± 0.05)

while the cyan curve represents the corresponding plots for 1024^3 resolution at $t = 49$. Also note that as expected, $E_\omega^{(2D)}(k)$ and $\Pi_\omega^{(2D)}(k)$ decrease with time due to their decaying nature. Thus we claim that the enstrophy spectrum and flux for the rapidly rotating decaying turbulence are described by Eqs. 3.9-3.10 respectively.

We now model the energy spectrum for the full flow. Using $\omega = \nabla \times \mathbf{u}$ and Eq. 3.9, we deduce that

$$\begin{aligned} E^{(2D)}(k) &= \frac{1}{k^2} E_\omega^{(2D)}(k) \\ &= C \epsilon_\omega^{2/3} k^{-3} \exp\left(-C(k/k_d)^2\right). \end{aligned} \quad (3.21)$$

For the cube (3D flow),

$$E_\perp(k) = E_x(k) + E_y(k). \quad (3.22)$$

Though $E_\perp(k)$ is not strictly equal to $\sum_{k_z} E^{(2D)}(k)$, we observe that $E_\perp(k)$ has similar scaling as $E^{(2D)}(k)$, i.e.,

$$E_\perp(k) = C'' \epsilon_\omega^{2/3} k^{-3} \exp\left(-C(k/k_d)^2\right). \quad (3.23)$$

where C'' is another constant. This is evident from Fig. 3.6(a), in which we plot $k^3 E_\perp(k)$

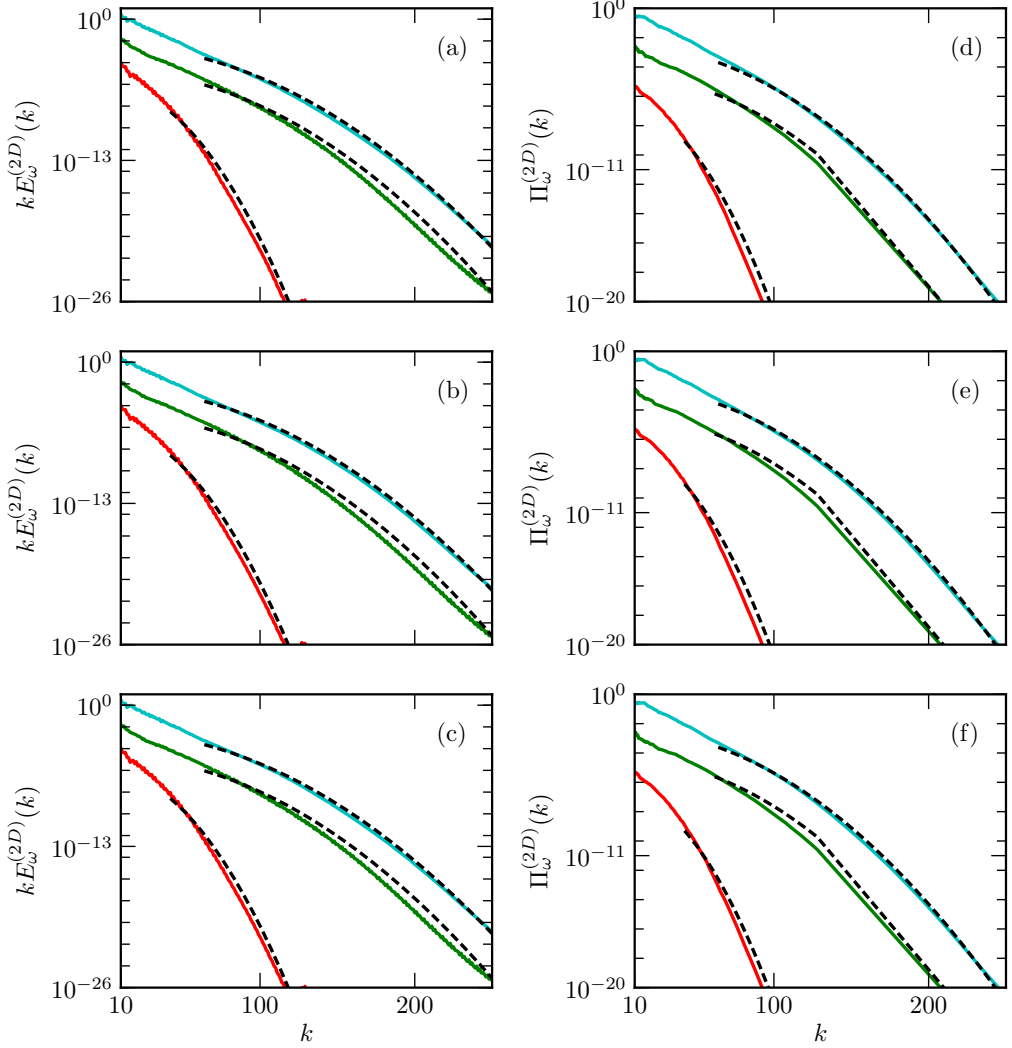


FIGURE 3.5: For the rapidly rotating decaying simulation using \mathbf{u}_\perp at $z = \pi/2, \pi, 3\pi/2$. Two-dimensional enstrophy spectrum $kE_\omega^{(2D)}(k)$ for (a) $z = \pi/2$, (b) $z = \pi$, (c) $z = 3\pi/2$ at $t = 49$ (green) and $t = 148$ (red) for 512^3 grid simulation, and at $t = 49$ (cyan) for the 1024^3 grid. The best fit curves using Equation (3.9) with parameters of Table 5.1 are shown as black dashed curves. (d,e,f) The corresponding plots of the 2D enstrophy flux $\Pi_\omega^{(2D)}(k)$ following the same color convection as above. The best fit curves however are of the form of Equation (3.10). Since $E_\omega^{(2D)}(k)$ and $\Pi_\omega^{(2D)}(k)$ of 512^3 and 1024^3 grids almost overlap on each other, we multiply $E_\omega^{(2D)}(k)$ and $\Pi_\omega^{(2D)}(k)$ of 1024^3 grid with a factor $1/100$ to differentiate the two plots.

vs. k and the best fit curves as dashed black lines, $C\epsilon_\omega^{2/3} \exp(-C(k/k_d)^2)$, at $t = 49, 148$ for 512^3 and $t = 49$ for 1024^3 grid resolution. In the figure, the red and green curves represent the numerical spectra for the 512^3 resolution (at $t = 49, 148$), while the cyan curve is for the 1024^3 resolution (at $t = 49$). We observe that $C'' \approx C$ because $E_z(k) \ll E_\perp(k)$. In the plots of Fig. 6 too, at $t = 49$, the energy spectra of 512^3 and 1024^3 grids almost overlap with each other. Therefore, we multiply $E(k)$ of 1024^3 grids with $1/100$ to contrast the two plots.

In rapidly rotating flows, the velocity component along z direction is strongly suppressed, hence $E_z(k) \ll E_\perp(k)$. This observation is supported by the plot of the anisotropy parameter of Fig. 3.1(g). Hence

$$\begin{aligned} E(k) &= E_x(k) + E_y(k) + E_z(k) \approx E_\perp(k) \\ &\approx C\epsilon_\omega^{2/3}k^{-3} \exp(-C(k/k_d)^2). \end{aligned} \quad (3.24)$$

In Fig. 3.6(b) we plot $k^3E(k)$ following the same convention as Fig. 3.6(a). We observe that the Eq. 3.24 fits with the numerical data quite well with the same C as of Fig. 3.5. Thus, we claim that $E(k) \approx C\epsilon_\omega^{2/3}k^{-3} \exp(-C(k/k_d)^2)$ for the rapidly rotating decaying turbulence.

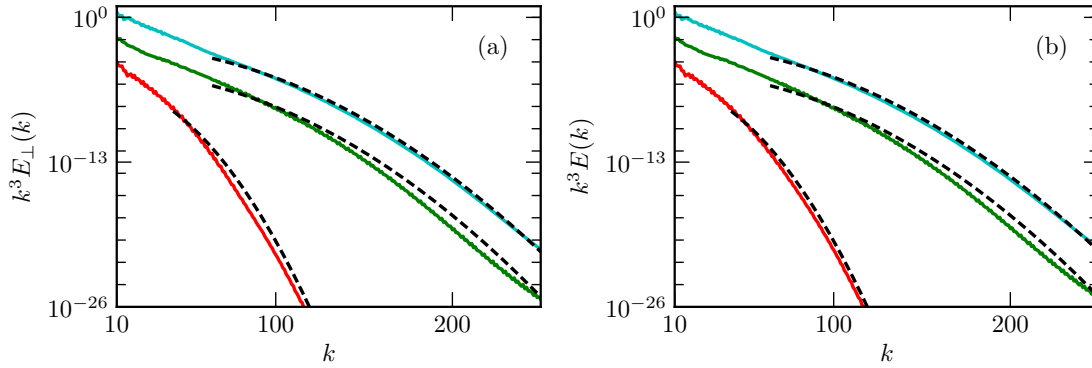


FIGURE 3.6: For the rapidly rotating decaying turbulence: (a) Normalized 3D energy spectrum $k^3 E_\perp(k)$ vs. k at $t = 49$ (green), 148 (red) for 512^3 grid simulation, and at $t = 49$ (cyan) for 1024^3 grid. The best fit curves following Equation (3.24) with ϵ_ω and C of Table 5.1 are plotted as black dashed curves. (b) The corresponding plots of $k^3 E(k)$ where $E(k) = E_\perp(k) + E_\parallel(k)$. Since $E(k)$ of 512^3 and 1024^3 grids almost overlap on each other, we multiply $E(k)$ of 1024^3 grid with a factor $1/100$ to differentiate the two plots.

As described in Sec. 1.4.2, for rapidly rotating turbulence, many researchers have reported dual spectrum for $E(k)$ with larger wavenumbers exhibiting Kolmogorov's spectrum. There is no unanimity on the spectral index for low wavenumber modes ($k < k_\Omega$) with researchers [77, 79, 98, 101–103, 112, 114, 142] predicting the spectral exponents as -2 , -3 , $-5/3$. In fact, Morize *et al.* [122] argue that the spectrum steepens with the increase of rotation speed. For details refer to Sec. 1.4.2. We did attempt to fit a power law ($E(k) \sim k^{-\alpha}$) with our data and observed that the spectral indices are -8 or lower for very small range of low wavenumbers. These observations yield stronger confidence in the model of Eqs. 3.9-3.10 that evidently spans over a much longer range of wavenumbers. We also remark that our model for $E(k)$ [Eq. 3.24] performs better than those of Pao and Kraichnan, which are described by Eq. 3.3 and Eq. 3.13 respectively. Note that the enstrophy and energy fluxes in Kraichnan's model are zero. See Appendix A.3 for details.

We conclude in the next section.

3.5 Summary

In this chapter, we have performed a numerical simulation of rapidly rotating decaying turbulence. In the asymptotic regime, the Rossby number of the flow is quite small, and the Reynolds number is quite large. Strong rotation causes quasi two-dimensionalization of the flow and formation of large coherent columnar structures. Most of the kinetic energy is concentrated in these structures, and the fluctuations in the inertial and the dissipative ranges have very small amount of energy leading to small Reynolds number for these fluctuations. Thus, rapidly rotating decaying turbulence has strong flow structures embedded in a sea of fluctuations of small magnitudes.

The main results of this chapter are as follows:

1. The significant fraction of energy is confined in Fourier modes $(\pm 1, 0, 0)$ and $(0, \pm 1, 0)$ that corresponds to the largest columnar structures in the flow.
2. The columnar structures in the system are formed due to the strong inverse cascade of energy. The vortex columns are quasi-2D with $u_z \ll u_\perp$, so we study the 2D energy and enstrophy spectra and fluxes of \mathbf{u}_\perp for various horizontal cross-sections. We observe that the kinetic energy flux is quite small for

$k > 8$, but the enstrophy flux, $\Pi_\omega^{(2D)}$ is significant in this regime. Further, we deduce the expression for the enstrophy spectrum and the enstrophy flux for such flows as Eqs. 3.9-3.10 respectively. Since $u_z \ll u_\perp$, $E(k) \approx E_\omega^{(2D)}(k)/k^2$, thus $E(k) \sim C\epsilon_\omega^{2/3}k^{-3} \exp(-C(k/k_d)^2)$. We observed that our proposed model for both kinetic energy spectrum and kinetic energy flux is in good agreement with numerical data.

As we have discussed the proposed model for the decaying rotating turbulence in this chapter, we start the discussion about the modeling of the kinetic energy spectrum of the forced rotating turbulence in the next chapter.

Chapter 4

On the energy spectrum of rapidly rotating forced turbulence

Turbulent fluid motion is an irregular condition of flow in which the various quantities show a random variation with time and space coordinates so that statistically distinct average values can be discerned.

– Hinze

In this chapter, we show the statistical features of the fully developed, forced, rapidly rotating, turbulent system using numerical simulations, and model the energy spectrum that fits well with the numerical data. We show that the behavior of the kinetic energy spectrum in the far dissipation range follows $\bar{E}(\bar{k}) \approx \exp(-0.05\bar{k})$, where overbar denotes appropriate non-dimensionalization. We also validate the Kuznetsov–Zakharov–Kolmogorov spectrum in wavenumber region smaller than the forcing wavenumber. The results shown in this chapter are based on the paper published in *Physics of Fluids* [185].

We performed numerical simulation for rotation rate $\Omega = 32$ in 512^3 and 102^3 grid resolutions. The simulations for 512^3 and 1024^3 ran up to $t = 56$ and $t = 3$ unit of time, respectively. The simulation details for the forced rotating turbulence are discussed in Sec. 2.5 of chapter 2. The parameters of the simulation are tabulated in Table 4.1.

This chapter is organized as follows: In Sec. 4.1, we discuss the effect of rotation on the 3D turbulent flow, that makes the flow quasi-two-dimensional. We also discuss

large scale coherent structures and a dual cascade of kinetic energy in the rotating turbulent flow. The model of the kinetic energy spectrum in the far dissipation range and the behavior of the kinetic energy spectrum in the wavenumber range $k < k_f$ are discussed in Sec 4.2. In the last section, we have summarized the main finding of the chapter.

N	k_f	Ω	ν	t_f	ϵ	Ro_L	Re_L	k_Ω	k_η	$k_{\max}\eta$
512^3	40 – 41	32	0.001	56	0.40	0.007	1736	286	141	4.4
1024^3	80 – 82	32	0.001	3	0.80	0.005	1786	202	168	3

TABLE 4.1: Parameters of the simulation: the grid-resolution N , the forcing wavenumber band k_f , rotation rate Ω , kinematic viscosity ν , final eddy turn-over time t_f , energy supply rate ϵ , Rossby number $\text{Ro}_L := u_{\text{rms}}/2\Omega L$, Reynolds number $\text{Re}_L := u_{\text{rms}}L/\nu$, Zeman wavenumber k_Ω , $k_{\max}\eta$, and the Kolmogorov dissipation wavenumber k_η . Here, L is integral length scale and it computed by Eq. 1.36.

4.1 Quasi-two-dimensionalization

As mentioned earlier, Coriolis force affects the perpendicular components of velocity field $\mathbf{u}_\perp = u_x\hat{\mathbf{x}} + u_y\hat{\mathbf{y}}$, and this force is the primary reason for the quasi-two-dimensionalization (2D) of three-dimensional (3D) turbulent flow. The quasi-two-dimensional behavior of the system is the signature of strong anisotropy in the system. The anisotropic parameter is a measure of anisotropy in the system.

In Fig. 4.1 we plot the anisotropy parameter $A \equiv E_\perp/2E_\parallel$ as a function of wavenumber. It is obvious from the figure that there is strong anisotropy ($A \gg 1$), and hence quasi-two-dimensionalization, at larger scales; the energy (E_\parallel) in the parallel (to Ω) component of velocity is much less than the average energy (E_\perp) in one of the perpendicular components. It is of importance to note that at smaller scales, the system is effectively isotropic since $A \sim 1$, and consequently the flow can be seen as a 3D turbulent flow where the effect of rotation is negligible.

The strong anisotropy at smaller wavenumber implies the formation of columnar structures in the system. We have investigated the energy contained in the smaller wavenumber and computed the percentage of energy associated with the modes.

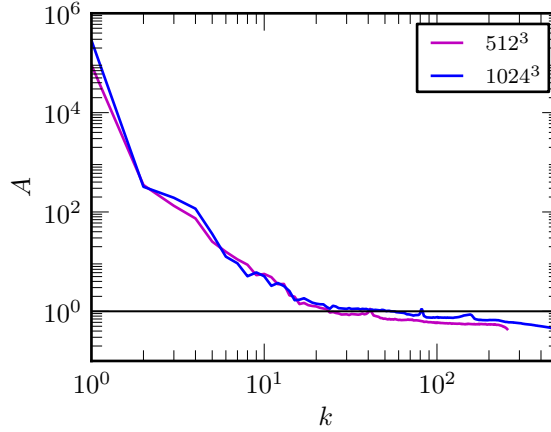


FIGURE 4.1: Anisotropy of the forced rotating turbulent system vs. wavenumber at $t = t_f$ for grid simulation of 512^3 grid resolution (magenta) and 1024^3 grid resolution (blue).

4.1.1 Large scale coherent structures

There is a large body of works [13, 14, 110, 122, 126, 144, 183, 184, 224] on the formation of the large scale structures, which is known to depend on the strength of rotation rate: at a very high rotation rate, the flow profile becomes quasi-two-dimensionalized with sharp coherent vortical columns, while at a low rotation rate, the columnar vortices are understandably disorganized. Figure 4.2(a) exhibits isosurfaces of constant $|\boldsymbol{\omega}|$ at $t = t_f$, where $\boldsymbol{\omega} = \nabla \times \mathbf{u}$ is the vorticity field. In Fig. 4.2(b) we plot the 2D velocity ($\mathbf{u} = u_x \hat{\mathbf{x}} + u_y \hat{\mathbf{y}}$) field for the horizontal cross-section taken at $z = \pi$ of the flow profile. The figure shows vortical columns. We observe that the columnar vortices are disorganized and not very sharp in appearance. Compared to the decaying case [184], in 3D forced rotating turbulence flow, the velocity in the direction of rotation is no longer constant, and the stretching and tilting of vortices occurs. Also, in the plane perpendicular to the direction of rotation, incompressible condition ($\nabla \cdot \mathbf{u}_\perp \neq 0$) is not satisfied and the two-dimensionalization is a relatively hindered than what happens in the decaying case. Additionally, the forcing randomizes the flow, and it starts affecting the velocity field and obstructs the alignment of vorticity field along the direction of rotation. This obstruction in alignment of velocity fields affects the structure formation in the forced rotating turbulent system.

In order to quantitatively understand the disorganization of the columnar struc-

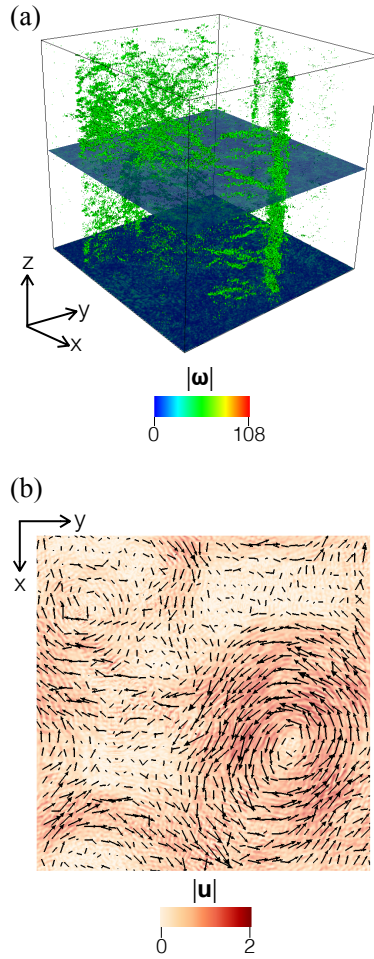


FIGURE 4.2: Plots for (a) iso-surfaces of various magnitudes of the 3D vorticity field, and (b) the density plot for the cross-section of 2D velocity field taken at $z = \pi$. Both the plots use the 1024^3 -grid simulations data.

tures in forced rotating turbulence, we study the energy content of the Fourier modes. Table 4.2 tabulates the energy contents of the most energetic Fourier modes for the forced rotating case at time frame $t = 56$ for the grid resolution of 512^3 and at $t = 3$ for 1024^3 grid. We do not list the energy of $-\mathbf{k}$ modes because $\mathbf{u}(-\mathbf{k}) = \mathbf{u}^*(\mathbf{k})$. The fraction of total energy contained in $18 \times 2 = 36$ Fourier modes is a significant amount of the total energy spread over 512^3 and 1024^3 modes. The Fourier modes $(k_x, k_y, k_z) = (1, 0, 0)$ and $(0, 1, 0)$ are the most dominant modes of the system. These modes contain 25 to 30 percent of total energy of the system. The situation is different in case of decaying rotating turbulence, where modes $(\pm 1, 0, 0)$ and $(0, \pm 1, 0)$ contain around 90 percent of total energy [184]. It may be remarked that in case of decaying turbulence these

4.1 Quasi-two-dimensionalization

modes are not strong initially but later in time they become dominant. In comparison, however, there is no significant temporal variation in the kinetic energy distribution for the forced rotating turbulence, as can be gathered from Table 4.2. The important thing to note is that, in case of the forced rotating turbulent system, more energy is uniformly distributed in the other modes as should be expected for the relatively less coherent columns. The large structure and anisotropy in the rotating turbulence are a consequences of the inverse cascade of energy.

TABLE 4.2: Percentage energy distribution among dominant modes at $t = 56$ and $t = 3$ for the grid resolution of 512^3 and 1024^3 at the rotation rate $\Omega = 32$ respectively. In table E_{mode} is defined as $E_{\text{mode}} = |u(\mathbf{k})|^2/2$, and E is the total energy of the system at $t = 3, 56$.

Mode (k_x, k_y, k_z)	E_{mode}/E (%) $t = 56$ $N = 512^3$	E_{mode}/E (%) $t = 3.0$ $N = 1024^3$
(1, 0, 0)	14.17	15.02
(0, 1, 0)	11.31	13.97
(1, 1, 0)	1.62	2.82
(-1, 1, 0)	1.43	0.45
(1, 2, 0)	0.92	1.77
(2, -1, 0)	0.51	0.40
(-2, 1, 0)	0.51	0.40
(2, 2, 0)	0.34	0.04
(1, -2, 0)	0.31	0.19
(-3, 1, 0)	0.31	0.22
(2, -2, 0)	0.21	0.12
(3, 1, 0)	0.13	0.06
(3, -2, 0)	0.13	0.06
(2, 1, 0)	0.13	0.23
(-1, -3, 0)	0.07	0.15
(-3, -2, 0)	0.05	0.44
(-2, -3, 0)	0.02	0.13
(-3, 0, 0)	0.02	0.06
Total %:	32.19	36.53

In the next subsection, we discuss the behavior of the kinetic energy flux for the system.

4.1.2 Inverse energy cascade

We compute the kinetic energy flux of the system using Eq. 2.26 and the results are shown in Fig. 4.3. The resulting figure, Fig. 4.3, explicitly depicts that at the scales larger than the scale at which forcing is active, there is inverse cascade of energy that is reminiscent of similar inverse cascade in the two-dimensional turbulence. As a result of this inverse cascade of the kinetic energy, there would be condensation of kinetic energy at lower wavenumber. This is also seen in the decaying rotating turbulent system [184]. This condensation is naturally expected to give rise to the large scale coherent structures. The inverse cascade of the kinetic energy below the forcing wavenumber affects the behavior of the kinetic energy spectrum in this region. We have studied the role of rotation on the energy spectrum in full wavenumber range.

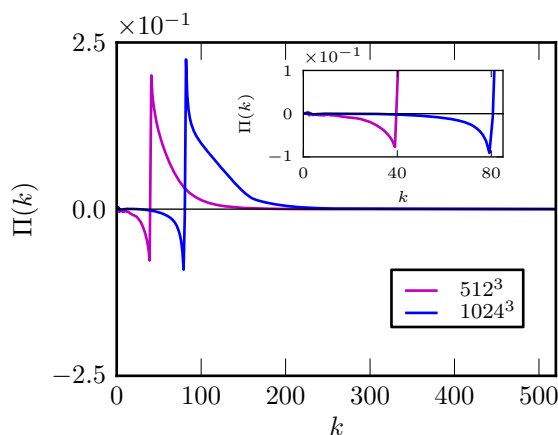


FIGURE 4.3: Plot of kinetic energy flux $\Pi(k)$ vs. k of the 3D velocity field at $t = t_f$ for grid resolution 512^3 (magenta) and 1024^3 grid resolution (blue). The peaks in the plots indicate the corresponding forced wavenumbers k_f .

4.2 The energy spectrum

The energy spectrum across the full range of wavenumbers is shown in Fig. 4.4(a) and Fig. 4.5. We note that about the forced scales (corresponding to the peaks in the plots), the spectrum is too disrupted to show any prominent scaling. We, thus, focus our attention on two different non-overlapping ranges of scales: the scales smaller than the forcing scales and the scales larger than the forcing scales.

It is obvious that the larger scales, being more affected by the rotation, should behave as if they are quasi-two-dimensionalized. In contrast, the smaller scales should have energy spectrum with an exponential term reminding one of the far dissipation range of the 3D isotropic homogeneous turbulence and the exponential fit found for the rapidly rotating decaying turbulence [184]. However, the energy spectra that we report in this chapter for both the ranges ($k < k_f$ and $k > k_f$) are—to the best of our knowledge—unreported in any direct numerical simulations done so far. In particular, we find that while the exponential fit in the decaying case goes as $\exp(-\text{constant} \times k^2)$, in the forced case it goes as $\exp(-\text{constant} \times k^1)$ that is less steep in the dissipation range ($k > k_\eta, k_f$). Furthermore, in the anisotropic regime, i.e., in the larger scales ($k < k_f$), the Kuznetsov–Zakharov–Kolmogorov (KZK) spectrum [108] emerges. In what follows, we model and discuss these spectra in detail as discovered in our numerical simulations.

4.2.1 Model spectrum for smaller scales

Most models of the forced rotating turbulence predict Kolmogorov’s $k^{-5/3}$ spectrum in the wavenumber range: $k_\Omega, k_f < k < k_{\text{DI}}$, where k_{DI} is the transition wavenumber (usually much smaller than k_η) between the inertial range and the dissipation range. Thus, in order to see this scaling, at the lower end we need to pick the larger one between k_Ω and k_f . Unfortunately, in our simulations, $k_\Omega > k_\eta$ and k_f are very close to k_η that is approximately just two to three times more than k_f . Because of this, there is no significant range of wavenumbers that could exhibit $k^{-5/3}$ spectrum discernible in a log-log plot.

Recently, Verma *et al.* [222] and Verma [27] have shown that for laminar hydrodynamic flows, the steady state energy spectrum and the flux are proportional $\exp(-k/k_\eta)/k$ and $\exp(-k/k_\eta)$ respectively. These functions satisfy Eq. 1.34, and also match with numerical simulations of the laminar flows. For our rapidly rotating flow, the energy content in the scales smaller than the forcing scale, $\sum_{k > k_f} E(k)$, is quite small; hence it can be treated as approximately laminar. This is due to the strong inverse cascade of energy to the larger scales that retain most of the energy. Motivated by this observation, we propose the following form for $E(k)$ in the smaller scales extending

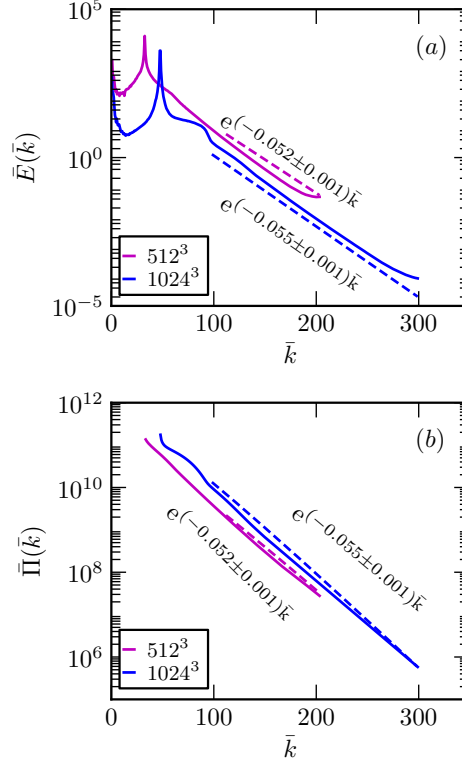


FIGURE 4.4: Plots of (a) the non-dimensionalized energy spectra, $\bar{E}(\bar{k})$, and (b) the non-dimensionalized energy flux, $\bar{\Pi}(\bar{k})$ at $t = t_f$, as generated by the simulations done with grid resolutions of 512^3 (magenta) and 1024^3 (blue) for the forced rotating turbulent fluid. The dotted lines are the fits generated in accordance with the energy spectra and the energy flux given in Eqs. (4.4)-(4.5).

into the far dissipation range:

$$E(k) \equiv \sum_{k-1 < k' \leq k} \frac{1}{2} |\hat{\mathbf{u}}(\mathbf{k}')|^2 = u_{\text{rms}}^2 f_L(k) \frac{1}{k} \exp(-\alpha k / k_{dh}). \quad (4.1)$$

From the form of this $E(k)$, it may be noted that Eq. 1.34 contains the effects of weak nonlinearity of the flow. The weak energy flux $\Pi(k)$ is the result of this nonlinearity.

The above $E(k)$ has only one exponent, viz., α , that needs to be determined. The exponent α may be a function of wavenumber k , but in our model, we have taken α as a constant. Here u_{rms} is the rms velocity of the high-pass filtered flow with all the component wave vectors greater than k_η . Note that we have introduced a new

wavenumber k_{dh} that is taken to be \sqrt{Re}/L , but now Re is calculated with U replaced by u_{rms} . In this context, recall that $k_\eta \equiv (\epsilon/\nu^3)^{1/4} \sim \sqrt{Re}/L$, where

$$\epsilon = \int_0^\infty 2\nu k^2 E(k) dk = 2\nu u_{\text{rms}}^2 k_{dh}^2 I, \quad (4.2)$$

with $I \equiv \int_0^\infty \bar{k} f_L(\bar{k}) \exp(-\alpha \bar{k}) d\bar{k}$ and $\bar{k} \equiv k/k_{dh}$. Thus, k_{dh} based on the high-pass filtered flow is analogous to k_η that is based on the unfiltered flow field.

Using \bar{k} , $\bar{E}(\bar{k}) \equiv E(k)k/u_{\text{rms}}^2$, and $\bar{\Pi}(\bar{k}) \equiv \Pi(k)/\epsilon$ as non-dimensionalized quantities, the relationship [Eq. 1.34] between the kinetic energy and the energy flux in the non-dimensionalized form becomes:

$$\frac{d\bar{\Pi}(\bar{k})}{d\bar{k}} = -\frac{\bar{k}}{I} \bar{E}(\bar{k}). \quad (4.3)$$

In the dissipation range $k \gg k_f$, where k_f is the forcing wavenumber and $f_L(\bar{k})$ is unity, the kinetic energy and the energy flux are respectively as follows:

$$\bar{E}(\bar{k}) = \exp(-\alpha \bar{k}), \quad (4.4)$$

$$\bar{\Pi}(\bar{k}) = \frac{1}{I} \left(\frac{1}{\alpha^2} + \frac{\bar{k}}{\alpha} \right) \exp(-\alpha \bar{k}). \quad (4.5)$$

It may be easily checked that the above two expressions satisfy the non-dimensionalized equation, Eq. 4.3. In Fig. 4.4(a) and Fig. 4.4(b), we plot $\bar{E}(\bar{k})$ vs. \bar{k} and $\bar{\Pi}(\bar{k})$ vs. \bar{k} respectively in semi-log scale at time frames $t = 56$ (magenta) for grid resolution of 512^3 and at $t = 3$ (blue) for 1024^3 grid. We observe that the predicted self-consistent model [Eq. 4.4 and Eq. 4.5] of the energy spectrum and the energy flux stands validated by our numerical data in the wavenumber range $k \in [141, 256]$ for 512^3 grid resolution, and $k \in [168, 512]$ for 1024^3 grid resolution. The values of α are 0.052 ± 0.001 for 512^3 grid resolution, and 0.055 ± 0.001 for 1024^3 grid. We are getting approximately same value of α for both the grid resolutions, thus, signifying that the parameter is robust and resolution-independent. The values of Re based on the aforementioned wavenumber ranges are 62 for 512^3 , and 115 for 1024^3 resolutions, which are one order less than the global Re (1736 and 1786 respectively for the grid resolutions 512^3 and 1024^3). Thus, there is reduction in strength of turbulence in the smaller scales, that is the reason why any power law scaling is hard to observe here.

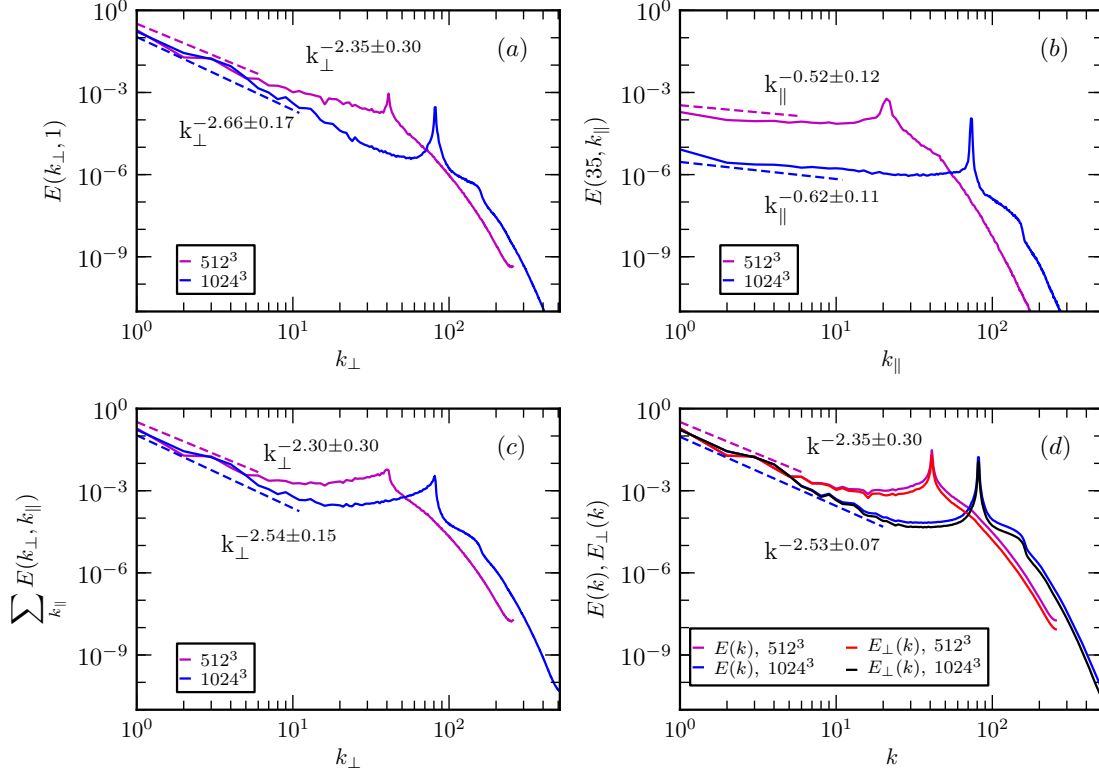


FIGURE 4.5: Plots of the (anisotropic) energy spectrum, $E(k_{\perp}, k_{\parallel})$ at $t = t_f$, as a function of (a) k_{\perp} for $k_{\parallel} = 1$, (b) k_{\parallel} for $k_{\perp} = 35$, and (c) k_{\perp} after the spectrum is summed over all k_{\parallel} . The dashed lines are the fitting lines; we have appropriately used the wavenumber range $1 \leq k_{\perp}, k_{\parallel} \leq 6$ for the 512^3 grid and $1 \leq k_{\perp}, k_{\parallel} \leq 11$ for the 1024^3 grid as the fitting ranges. As in the other plots, we have used magenta for 512^3 grid-resolution data and blue for 1024^3 grid-resolution data. Subplot (d) exhibits the plots for the (isotropic) energy spectra, $E(k)$ (magenta and blue) and $E(k_{\perp})$ (red and black), as functions of k . Here, we have used additional colours—red and black—to respectively indicate the data corresponding to 512^3 grid and 1024^3 grid. The fitting ranges in subplot (d) are $1 \leq k \leq 6$ for 512^3 grid and $1 \leq k \leq 20$ for 1024^3 grid.

4.2.2 Model spectrum near larger scales

Although one can extract scaling exponents from the $E(k)$ vs. k plot to characterise the system, strictly speaking, in the anisotropic regime, the energy spectrum should not be modelled as a function of k . It is more sensible that the energy spectrum be explicitly dependent on both \mathbf{k}_\perp (two dimensional vector perpendicular to the rotation axis) and k_\parallel (wavenumber corresponding to the direction parallel to the rotation axis). Thus, we define such a spectrum as,

$$E(k_\perp, k_\parallel) = \sum_{\substack{k_\perp-1 < k'_\perp \leq k_\perp, \\ k_\parallel-1 < k'_\parallel \leq k_\parallel}} \frac{1}{2} |\hat{\mathbf{u}}(k'_\perp, k'_\parallel)|^2. \quad (4.6)$$

Note that, under the assumption of axisymmetry, we have used the magnitude of \mathbf{k}_\perp in the argument of the energy spectrum.

The energy spectrum of the system is calculated by using Eq. 4.6 and plotted in Fig. 4.5. In Fig. 4.5(a)-(b), it is remarkable to note that the energy spectrum observed from our numerical simulation is quite close to the Kuznetsov–Zakharov–Kolmogorov (KZK) spectrum— $E(k) \sim k_\perp^{-5/2} k_\parallel^{-1/2}$ —within errorbars. The strong rotation supplies a small parameter, Ro , in the framework of weak turbulence. Using this it has shown [108] that, in the anisotropic limit $k_\perp \gg k_\parallel$, structures elongated along the rotation axis are brought forth through dominating local interactions. Further, the KZK spectrum comes out as an exact solution. Although the aforementioned weak turbulence analysis has been done for decaying rotating turbulent fluid, we emphasize that this spectrum appears in our numerical simulations exactly where the system is strongly anisotropic and shows elongated structures, thereby somewhat satisfying the requirements for the appearance of the spectrum. It may be noted, in this context, that the aforementioned plots are for the case: $k_\perp \gg k_\parallel$, just what the weak turbulence analysis requires. We also note that the shift of the peaks away from k_f in Fig. 4.5(b) is because the abscissa is k_\parallel and not k , and thus, the identity $k^2 = k_\perp^2 + k_\parallel^2$ with $k = k_f$ and $k_\perp = 35$ locates the peaks at $k_\parallel \approx 21$ and $k_\parallel \approx 74$ respectively for 512^3 and 1024^3 grid resolutions.

Additionally, in Fig. 4.5(c), we note that the scaling exponent of k_\perp is unchanged within the error limits even when the spectrum is summed over all k_\parallel . Further, Fig. 4.5(d) showcases the fact that this scaling exponent ($\sim -5/2$) is very robust; in the range

$A \gg 1$, even the isotropic energy spectrum, $E(k)$, scales as $\sim k^{-5/2}$ and so does $E_{\perp}(k)$ simply because the share of energy contained in the plane perpendicular to the rotation axis is large. We remark, however, the scaling exponent of k_{\parallel} is not very robust and it varies with the choice of k_{\perp} range (see Appendix A.5). Nevertheless, we believe that ours is the first numerical demonstration of KZK spectra in forced rotating turbulence.

4.3 Summary

We have performed direct numerical simulations of a 3D turbulent fluid forced at intermediate scales. The fluid is rotating with a high rotation rate corresponding to $Ro \sim 10^{-3}$. The main results of this chapter are as follows:

1. The system becomes highly anisotropic at larger scales; coherent columnar structures are formed but they are relatively more diffused in appearance compared to what is seen in the case of decaying rotating turbulence. We have also found dual cascade regions—forward and reverse cascades—for both the energy and the enstrophy (calculated on a 2D horizontal plane; see Appendix A.4).
2. We observed that the kinetic energy spectrum varies as $k_{\perp}^{-2.35 \pm 0.30}$ in wavenumber range $k_{\perp} \in [1, 6]$ for grid resolution of 512^3 , and scales as $k_{\perp}^{-2.66 \pm 0.30}$ in wavenumber range $k_{\perp} \in [1, 11]$ for grid resolution of 1024^3 . The kinetic energy spectrum as a function of k_{\parallel} shows power scalings for fixed k_{\perp} , specifically, $E(35, k_{\parallel}) \sim k_{\parallel}^{-0.52 \pm 0.12}$ in wavenumber range $k_{\parallel} \in [1, 6]$ for grid resolution of 512^3 and $E(35, k_{\parallel}) \sim k_{\parallel}^{-0.62 \pm 0.11}$ in wavenumber range $k_{\parallel} \in [1, 11]$ for 1024^3 grid. Within the error bars, these scalings are in conformity with the KZK-spectrum.
3. Our proposed model is in very good agreement with the numerical results over the wavenumber range $k \in [k_{\eta}, k_{\max}]$.

The main reasons for the anisotropy in the rotating turbulence is the Coriolis force, that redistributes the kinetic energy such that the three-dimensional isotropic system becomes anisotropic. Thus, in order to understand the system, an understanding of the anisotropic properties of the energy transfer is paramount. The next chapter is based on a comparative study of the anisotropic energy transfer of the decaying and the forced rotating turbulences.

Chapter 5

Anisotropic energy transfer in rotating turbulence

The necessary connection between the diffusion and the supply of energy to the turbulent motion is a fundamental characteristic of turbulent flow.

– Townsend's

In order to quantify the anisotropy in the distribution of energy among the Fourier modes, we need certain useful mathematical measures, e.g., ring-to-ring energy transfer and conical flux, which have been defined in chapter 2. We decompose the Fourier space into shells and sectors (see chapter 2 for definitions). As mentioned in chapter 2, a ring is the intersection of a shell and a sector. We have studied the energy transfer in the rapidly rotating [$\text{Ro} \sim \mathcal{O}(10^{-2}) - \mathcal{O}(10^{-3})$] decaying and forced fully developed turbulence [$\text{Re} \sim \mathcal{O}(10^3)$] by performing direct numerical simulations in cubic periodic boxes.

We present the results for the energy transfer, such as the shell-to-shell energy transfer, the ring-to-ring energy transfer, and the conical energy flux in the 3D hydrodynamic turbulence rendered anisotropic by rapid rotation. Specifically, we compare the anisotropic energy transfer in the decaying and the forced rotating turbulences. We have used the same initial condition for the decaying and the forced rotating turbulences mentioned in Sec. 2.5 of chapter 2. The grid resolution for the numerical

simulations is 512^3 . Most of our results are reported using data of a snapshot at $t = 4$ because at later times, the qualitative results do not change, and the numerical values of the meaningful and relevant quantities become too small to facilitate any meaning conclusions. Nonetheless, wherever possible and meaningful, we do discuss the data corresponding to $t = 50$ rather than the one for $t = 4$. We tabulate all the relevant parameters used in the simulations in Table 5.1. The results discussed in this chapter are based on a paper published in Physics of Fluids [225].

This chapter is organized as follows: In Sec. 5.1, we discuss the ring energy spectrum for decaying and forced rotating turbulence. The ring energy spectrum is one of the measures of the anisotropy in the system. In Sec. 5.2, we discuss the shell-to-shell energy transfer, which shows whether the transfer is local or non-local. In section 5.3, we discuss the behavior of the anisotropic energy transfer for the decaying and the forced rotating turbulent flows in detail. The analysis in this chapter is done for a snapshot at the corresponding time frame.

	Ω	ν	t_f	u_{rms}	L	Ro_L	Re_L	k_Ω	k_η
Forced	32	10^{-3}	56	0.85	2.04	0.007	1736	286	141
Decay	16	10^{-3}	4	0.75	1.45	0.016	1088	416	69
Decay	16	10^{-3}	50	0.51	2.76	0.006	1403	1871	32

TABLE 5.1: Parameters of the simulation: The values of the forcing wavenumber band, k_f ; the rotation rate, Ω ; the kinematic viscosity, ν ; the final simulation run time, t_f ; the Rossby number, $\text{Ro}_L := u_{\text{rms}}/2\Omega L$; the Reynolds number, $\text{Re}_L := u_{\text{rms}}L/\nu$; the Zeman wavenumber [6] $k_\Omega := (\Omega^3/\epsilon)^{1/2}$; and the Kolmogorov dissipation wavenumber, $k_\eta := (\epsilon/\nu^3)^{1/4}$ are given in the table. Here, u_{rms} is the r.m.s. velocity of the field and L is the integral length scale. (See Appendix A for details.). In case of forced rotating turbulence the system is forced in the wavenumber band $k_f \in (40, 41)$.

5.1 Ring energy spectrum

Using Eq. 2.21, we compute the ring energy spectrum for which we decompose the Fourier space into 256 shells of equal widths and each shell into 20 thin equispaced rings from $\theta = 0$ to $\theta = \pi/2$.

The contour plot of 3D vorticity field, the ring energy spectrum, and the contour

5.1 Ring energy spectrum

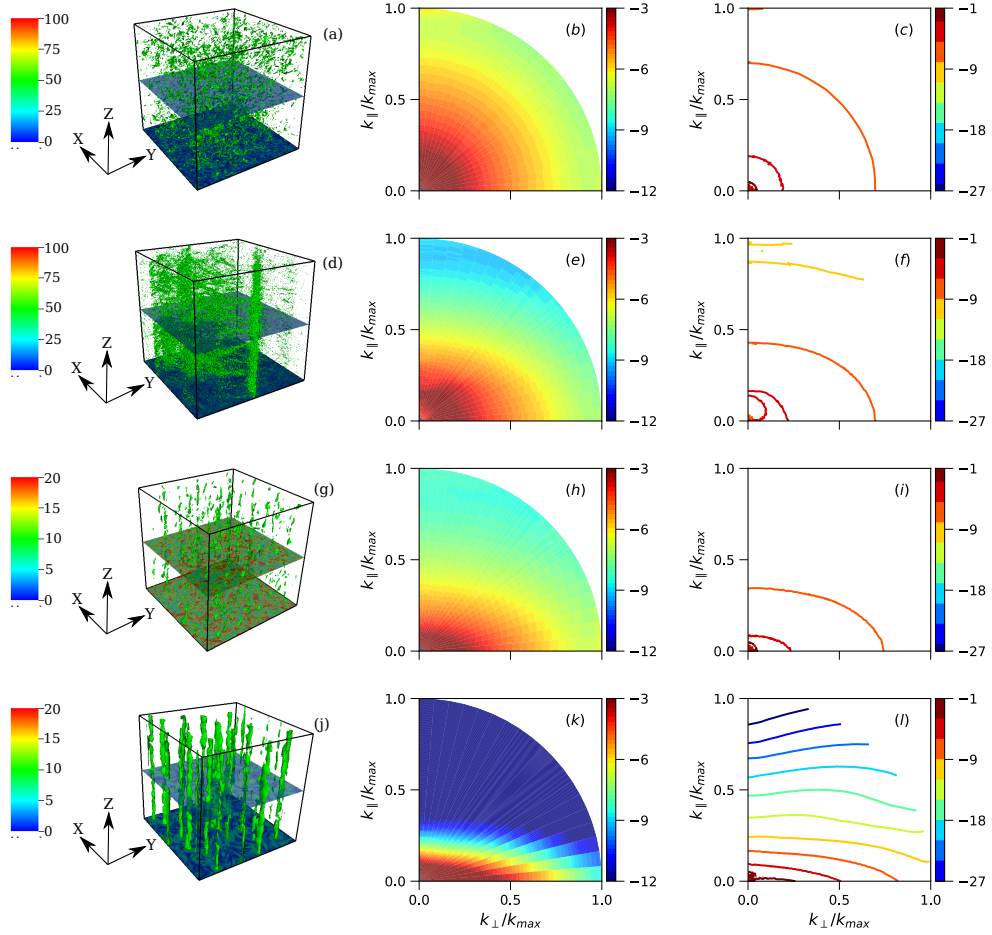


FIGURE 5.1: *Flow structure and distribution of ring energy $E^{(m,\alpha)}(k, \theta)$ in rotating turbulence.* The contour plot of 3D vorticity field, the ring energy spectrum, and the contour plot of ring energy spectrum are respectively shown in figures (a)-(c) at time frame $t = 0$ and in figures (d)-(f) at time frame $t = 56$ for the forced rotating turbulence with rotation rate $\Omega = 32$. Similarly, the contour plot of 3D vorticity field, the ring energy spectrum, and the contour plot of ring energy spectrum are respectively depicted in figures (g)-(i) at time frame $t = 0$ and in figures (j)-(l) at time frame $t = 4$ for the decaying rotating turbulence with rotation rate $\Omega = 16$.

plot of ring energy spectrum for forced rotating turbulence at time frame $t = 0$ are shown in the first row of Fig. 5.1, i.e., Fig. 5.1(a)-5.1(c), respectively. We observe that the vorticity field is random in nature and the system is isotropic. In Figs. 5.1(d)-5.1(f), we plot the same quantities for the forced rotating turbulence for $\Omega = 32$ at time frame $t = 56$ and observe formation of columnar structures in the system. Moreover, the ring energy spectrum shows that the forced rotating turbulent system is anisotropic at smaller wavenumbers and nearly isotropic at higher wavenumber region [98].

In the case of decaying rotating turbulence at time frame $t = 0$ [Figs. 5.1(g)-5.1(i)], we already observe (somewhat incoherent) columnar structures and mild anisotropy. This is because of the particular initial condition chosen for simulating the decaying rotating turbulence as mentioned earlier in Sec. 2.5. As the time progress, the decaying rotating turbulent system becomes more and more anisotropic, and more coherent columnar structures come into being. These facts are quantitatively illustrated in Figs. 5.1(j)-5.1(l). The density and the contour plots elucidate that as time progress, the kinetic energy is stronger near the equatorial [22, 99] region than in the polar region, which is a clear indication of the strong anisotropy induced in the system.

These may be contrasted with the results obtained in the MHD turbulence—either decaying or forced—where the system becomes in such a manner that the kinetic energy is comparatively more in the equatorial region [5, 200, 226]. In these MHD systems, a uniform external magnetic field is applied along the z -axis just like the angular velocity in case of the rotating turbulence.

The anisotropic behavior of the rotating turbulence, where energy is accumulated in the plane perpendicular to the rotating axis, is owing to the transfer of energy due to the nonlinear term. We start with investigating the shell-to-shell energy transfer followed by the studies of the conical energy flux and the ring-to-ring energy transfer.

5.2 Shell to shell energy transfer

Although, as we mentioned earlier, the shell-to-shell energy transfer is not designed to capture the anisotropy in the energy distribution in the system, below we discuss the transfer as obtained in our numerical simulations so as to compare our results with the ones existing in the literature. This discussion also makes one realize why the ring-to-ring and the conical energy fluxes are pertinent for the study at our disposal.

5.2 Shell to shell energy transfer

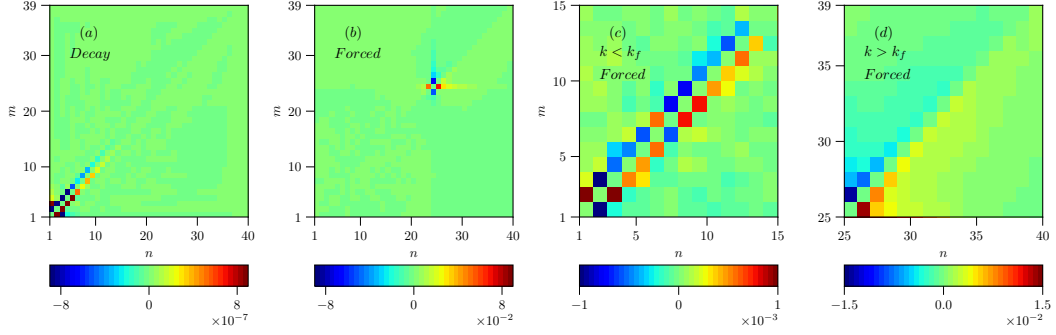


FIGURE 5.2: *Inverse and forward cascades.* Shell-to-shell energy transfer rate T_n^m (quantified by the colourbars) for (a) decaying rotating turbulence with $\Omega = 16$ at time frame $t = 50$, and (b) forced rotating turbulence with $\Omega = 32$ at time frame $t = 56$. The subplots (c) and (d) depict the shell-to-shell energy transfers in the two non-overlapping wavenumber regions— $k < k_f$ and $k > k_f$ respectively—for the forced rotating turbulence. The forcing shell number is 24. Here m and n denote the donor and the receiver shells respectively.

First, we partition the Fourier space into 40 concentric spherical shells. Recall that the inner and the outer radii of Shell(n) are k_{n-1} and k_n respectively. In this case, $k_n \in \{2, 4, 8, \dots, 128, 256\}$. We have used logarithmic binning for the shells lying in the inertial range in order to capture the local transfer of energy as has been argued by Kolmogorov about the energy transfer, albeit in the inertial range of homogeneous isotropic turbulence. To this end, we have chosen $k_n/k_{n-1} \approx 1.08$ for the k_n 's between 8 to 128. Subsequently, we compute the shell-to-shell energy transfer by using Eq. 2.27 and plot the results in Fig. 5.2. We adopt the convention that, given two shells, one is donor that transfers energy to the other, defined to be receiver. In the plots, the x -axis represents shell index, n , of the receiver shell and the y -axis represents shell index, m , of the donor shell.

From Fig 5.2(a), we observe that the most dominant transfer is local, occurring among $(n-1)$ th, n th and $(n+1)$ th shells for any n . Here any n th shell receives energy from $(n-1)$ th shell and gives energy to $(n+1)$ th shell, establishing that the energy transfer is local and forward in decaying rotating turbulence.

In contrast, in Fig 5.2(b), it appears that the most dominant transfers occur locally near the forcing shell, Shell(24). One can see that Shell(24) is transferring energy to Shell(23) and also to Shell(25), thereby signalling the inverse and the forward cascades

for $k < k_f$ and $k > k_f$ respectively. However, whether these cascades are present beyond the immediate neighbourhood of k_f , is not very clear from the figure. Thus, a more detailed analysis is done by studying the two wavenumber regions— $k < k_f$ and $k > k_f$ —separately. In Figs. 5.2(c)-5.2(d), in line with the results reported by Mininni et al. [79], we note a superposition of inverse and forward cascades of energy in the wavenumber region $k < k_f$ and forward energy transfer for $k > k_f$. We can also observe a hint of nonlocality, albeit weak, in the energy transfers.

Again, it is insightful to once again note the similarity with the analogous system, viz., the MHD turbulence: It is well known that the kinetic energy transfer is local and forward in the decaying MHD turbulence [191, 194] as well as in the forced [5, 192, 196, 197] MHD turbulence for the scales smaller than the forcing scale.

The shell-to-shell energy transfer tells us about how energy content of one shell is transferred to another shell. Since, by construction, the energy content of each shell is the sum of the energies in all the modes inside the shell, the information about the distribution of energy over the azimuthal and the polar angles is missing. Consequently, the study of the energy distribution among shells is not going to divulge the anisotropic nature of the rotating turbulence. Therefore, we now proceed to investigate the evolution of the energy distribution among sectors and rings.

5.3 Ring-to-ring energy transfer

We partition the northern hemisphere of radius $|\mathbf{k}| = 256$ into 20 sectors such that for i th sector, Sector(i), the polar angles of the inner and the outer conical boundaries are $(i - 1)\pi/40$ and $i\pi/40$ respectively. We can now easily compute the conical energy flux by using Eq. 2.28 for both the decaying and the forced rotating turbulences.

The results have been compactly illustrated in Fig. 5.3. We observe from Fig. 5.3 that, for both the decaying and the forced rotating turbulences, the net energy transferred through any conical boundary of a sector is equatorward. However, if we exclusively focus on the inverse cascade regime, i.e., $k < k_f$ in the forced case, the transfer is poleward as $\Pi(\theta) < 0$; the forward cascade in the higher wavenumber region is equatorward, as it should be in order for the aforementioned net energy transfer to be equatorward. It is also interesting to note that while the rate of energy transfer in the decaying case increases mostly monotonically with the polar angle, the rate first

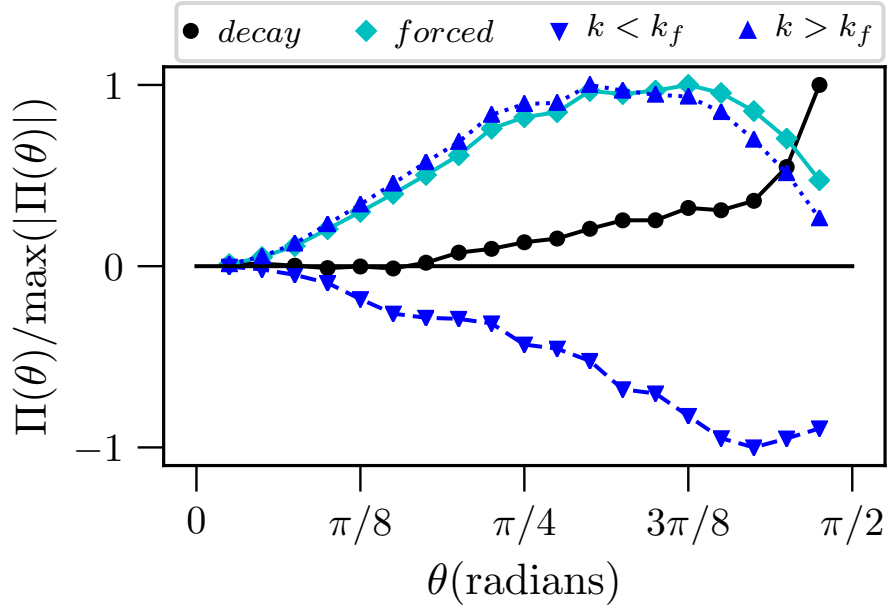


FIGURE 5.3: Conical flux is almost monotonic for the decaying rotating turbulence but distinctly non-monotonic for the forced counterpart. Plots of normalized conical energy flux, $\Pi(\theta)/\max(|\Pi(\theta)|)$, for rapidly rotating decaying turbulence (for $\Omega = 16$ and at $t = 4$) and forced turbulence (for $\Omega = 32$ and at $t = 56$) versus polar angle in radian. The solid black curve with circles and the solid cyan curve with diamonds respectively correspond to the decaying and the forced cases. Furthermore, the blue dotted curve with solid down-triangles and blue dashed curve with up-triangles correspond to the wavenumber ranges $k > k_f$ and $k < k_f$ respectively the same forced system.

increases and then decreases near the equator in the forced case. However, why the rate of energy transfer is not monotonic in the forced case unlike the decaying case is not immediately clear and requires further investigation.

While the kinetic energy flux concerns itself with the shell decomposition of the Fourier space, the conical energy flux deals with the sector decomposition of the same. Thus, just like the kinetic energy flux as given by Eq. 2.26, the conical energy flux provides a coarse-grained information about transfer of energy. Evidently, the most detailed information is hidden in the ring-to-ring energy transfer which quantifies how the parts of a sector in a given shell or how the parts of a shell in a given sector partici-

pate in the energy transfer. In short, the ring-to-ring energy transfer that quantifies the anisotropic energy transfer between the rings would uncover the minute details about the energy transfer (e.g., whether the transfer is local within a shell) in the rotating turbulence.

To this end we use 20 shells constructed in the same manner as described in Sec. 5.2 and 20 sectors as described in the beginning of this section, so that we have 400 rings partitioning the northern hemisphere of the Fourier space. Subsequently, we compute ring-to-ring energy transfer by using Eq. 2.29 and plot the results in Fig. 5.4. We adopt the convention that, given two rings, one is donor that transfers energy to the other, defined to be receiver. In the plots, the x -axis represents sector index, α , of the receiver ring and the y -axis represents sector index, β , of the donor ring.

Although we have done analysis with all the 20 shells, for illustrative purpose and concreteness, in Fig. 5.4(a), we work with a particular shell, Shell(10). We observe that the energy is transferred from Ring(10, α) to Ring(10, $\alpha + 1$) in the decaying case, i.e., the transfer is equatorward.

For the forced case, where now k_f corresponds to Shell(12), $\bar{T}_{(10, \alpha-1)}^{(10, \alpha)} > 0$ implying poleward transfer [Fig. 5.4(b)]; and $\bar{T}_{(n, \alpha+1)}^{(n, \alpha)} > 0$ for $n > 12$ [e.g., $n = 16$ in Fig. 5.4(c)] validating that the transfer is equatorward for the higher wavenumber region. The transfers in all the cases, including the case of decaying rotating turbulence, are predominantly local, i.e., the transfers happen mostly among the nearest neighbouring rings in a given shell.

One could now ask, since the shell-to-shell energy transfer is local and so is the ring-to-ring transfer in a given shell, what the property of energy transfer between rings of two adjacent shells is. It is not obvious a priori if the transfer is local. To answer this question in Fig. 5.4(d)-5.4(f), we depict the energy transfer between rings lying inside two adjacent shells: We plot the normalized ring-to-ring energy transfer between Ring(9, α) and Ring(10, β) for the decaying rotating turbulence and the forced rotating turbulence, and also between Ring(15, α) and Ring(16, β) for the forced case. From the close inspection of the figures, it is clear that the most dominant transfers in the forward cascade in the decaying case, and the inverse and the forward energy cascades forced case are local. The energy transfer rate, $\bar{T}_{(m, \alpha)}^{(n, \beta)}$, is the maximum when $|n - m| = 1$ and $\alpha = \beta$. In Figs. 5.5(a)-5.5(b), we show a schematic diagram of the anisotropic energy transfer (the ring-to-ring energy transfer) in the decaying and the

5.3 Ring-to-ring energy transfer

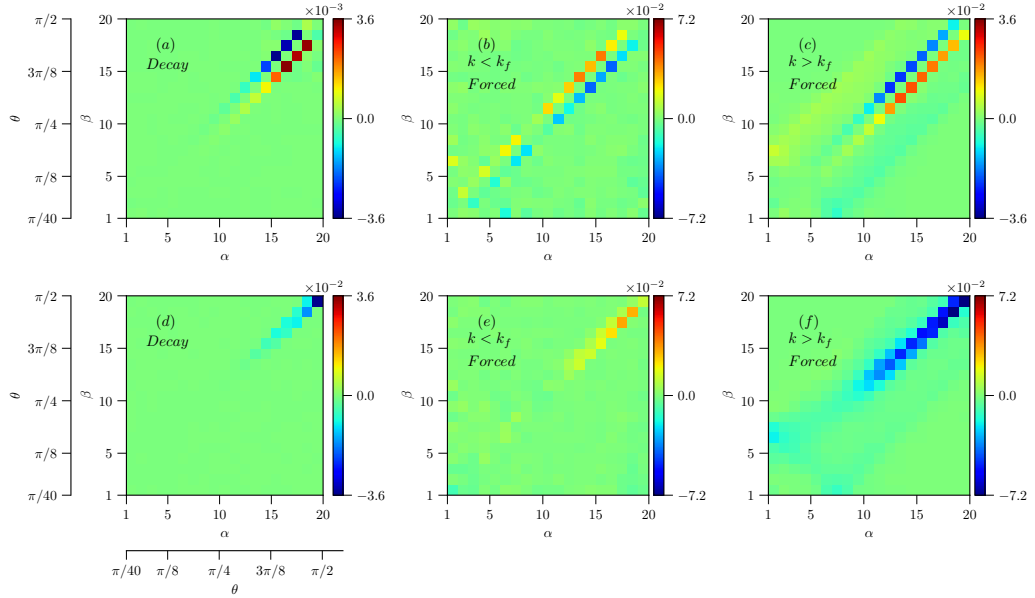


FIGURE 5.4: The local energy transfer is equatorward in decaying case; and is polewards in forced case for $k < k_f$ and equatorward for $k > k_f$. The normalized ring-to-ring energy transfer, $\bar{T}_{(n,\alpha)}^{(m,\beta)}$, has been quantified by the colourbars. The x -axis represents sector index, α , of receiver ring and the y -axis represents sector index, β , of the donor ring. The upper row exhibits the transfer among various rings inside (a) Shell(10) for the decaying rotating turbulence, (b) Shell(10) for the forced rotating turbulence, and (c) Shell(16) for the forced rotating turbulence. Shell(12) corresponds to the forcing scale. The lower panel illustrates the ring-to-ring energy transfer in (d) the decaying rotating turbulence from Shell(10) to Shell(9), (e) the forced rotating turbulence from Shell(10) to Shell(9), and (f) the forced rotating turbulence from Shell(16) to Shell(15).

forced rotating turbulences. In this figure, arrows represent the direction of the energy transfer.

In passing, we remark that the details of the ring-to-ring energy transfer has been explored in the case of the forced MHD turbulence [5, 187] as well and it has been reported that—quite contrary to what we observe for the rotating hydrodynamic turbulence—the transfer of kinetic energy is poleward in the wavenumber regime, $k > k_f$. Considering the close analogy between the two turbulent systems, one under the influence of uniform magnetic field and the other undergoing rotation, the aforementioned difference in their properties is an intriguing point to ponder upon.

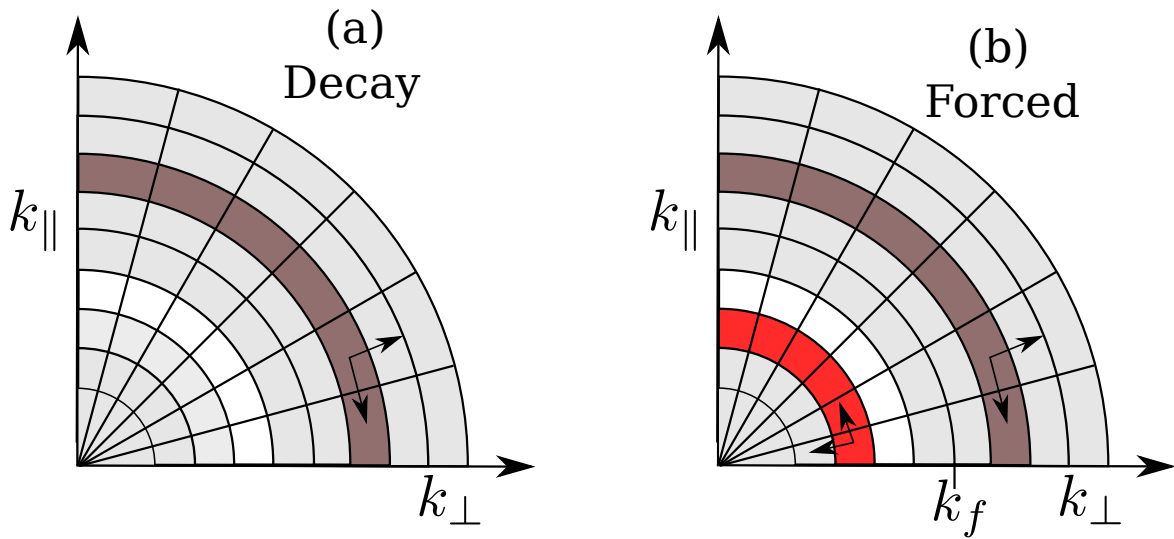


FIGURE 5.5: Schematic diagram for the anisotropic energy transfer in (a) decaying, and (b) forced rotating turbulence.

5.4 Summary

We have conducted numerical simulations of the decaying and the forced rotating turbulent flows in a cubic periodic boxes of size $(2\pi)^3$. The grid resolution of the simulations is 512^3 . We have studied the energy transfer in the rapidly rotating [$\text{Ro} \sim \mathcal{O}(10^{-2}) - \mathcal{O}(10^{-3})$] fully developed turbulence [$\text{Re} \sim \mathcal{O}(10^3)$]. There is emergence of anisotropy in the system due to rotation and this has been our primary focus in this chapter. We have systematically investigated and characterized this anisotropy in detail through the ring-to-ring energy transfer, and we have compared the effects of

the rapid rotation on the anisotropic energy transfers in the forced turbulence and the decaying turbulence. The main outcomes of this chapter are as follows:

1. For the decaying case, we find that the energy transfer between shells is local and forward, i.e., low to high wavenumbers. Furthermore, the transfer of energy between different ring inside a single shell is local and equatorward. The conical energy flux in the decaying rotating turbulence increases monotonically with the sectors' indices, i.e., the flux is maximum at the equator. Also, the most dominant transfer of energy occurs between the rings in the same sector of two adjacent shells. Some of these numerical results are in line with the analytical predictions of Cambon and Jacquin [169], and Walleffe [188].
2. The forced rotating turbulence is rather more interesting because of the present of a forcing wavenumber k_f . We find the well-known forward cascade of energy in the wavenumber range $k > k_f$, but a coexistence of the inverse and the forward cascades of energy in $k < k_f$ wavenumber region. These cascades are dominantly local in nature. The conical energy flux becomes more and more strong upto the polar angle $3\pi/8$ (approximately) and then becomes weaker as the equator is reached. The ring-to-ring energy transfer reveals a poleward transfer of energy in wavenumber region $k < k_f$ and an equatorward transfer of energy in the wavenumber region $k > k_f$. Additionally, here also we find that the transfer of energy occurs predominantly between the rings belonging to the same sector but to two adjacent shells.

Up to now, in this thesis, we have discussed the statistical models which are in good agreement with the numerical data in the far dissipation range of the rotating turbulence. We have also investigated the cause of the anisotropic behavior of the system through the anisotropic energy transfer. In the next chapter, We summarize the main conclusion of the thesis.

Chapter 6

Discussions and conclusions

The future belongs to those who believe in the beauty of their dreams.

– Eleanor Roosevelt

6.1 Conclusions of the thesis

The 3D homogeneous and isotropic turbulence shows the Kolmogorov power-law scaling, i.e., $E(k) \sim k^{-5/3}$ for the kinetic energy spectrum in the inertial range, and the transfer of energy is forward in nature. In the presence of rotation, the Coriolis force makes the system anisotropic, and it deviates from the Kolmogorov scaling. The system also shows an inverse cascade of energy. Owing to the inverse cascade of energy, the columnar structures are observed in the system, and a significant part of the total energy of the system are accumulated in smaller wavenumber modes. One of the main reasons for the anisotropy in the system is the anisotropic energy transfer due to the nonlinear term. The goal of the thesis has been to understand the direction of the anisotropic energy transfer, which makes the system anisotropic, and model the kinetic energy spectrum of the system.

In this thesis, we have studied the statistical properties viz., the kinetic energy spectrum, the enstrophy spectrum, the kinetic energy flux, etc., of both the decaying

and the forced rotating turbulences and modeled the kinetic energy spectrum. We have performed direct numerical simulations in a three-dimensional cubic periodic box of box size $(2\pi)^3$. We have used two different angular velocities: $\Omega = 16$ for the decaying rotating turbulence and $\Omega = 32$ for the forced rotating turbulence. The Rossby number is quite small [$\text{Ro} \sim \mathcal{O}(10^{-2}) - \mathcal{O}(10^{-3})$] and the Reynolds number is quite high [$\text{Re} \sim \mathcal{O}(10^3)$].

We have computed the kinetic energy spectrum, kinetic energy flux, and kinetic energy transfer, which are the pertinent statistical quantities to understand the effect of rotation on the 3D homogeneous and isotropic turbulence. We have decomposed the Fourier space into shells, sectors, and rings to study the anisotropic property of the system. We have used variable energy flux formalism to construct the model for the kinetic energy spectrum. The primary outcomes of the thesis are discussed below.

We have observed that the Coriolis forced makes the system quasi-two-dimensional, where the transverse velocity components are very much stronger than the parallel velocity components. A detailed analysis of the anisotropic properties of the decaying rotating turbulence shows the transverse components of the velocity field are stronger than the parallel components of the velocity field in smaller wavenumber region. We have decomposed the Fourier space into rings and have computed the ring energy spectrum. The ring spectrum of the system shows an explicit dependency on the polar angles. A rigorous study of the ring spectrum of decaying rotating turbulence shows that the system is anisotropic at every scales. We observed that a major fraction of energy is confined in Fourier modes $(\pm 1, 0, 0)$ and $(0, \pm 1, 0)$ in the decaying case.

The strong columnar structure in decaying rotating turbulence indicates quasi-two-dimensional behavior of the system with $u_z \ll u_\perp$, so we study the 2D energy and enstrophy spectra and fluxes of \mathbf{u}_\perp for various horizontal cross-sections. Based on the Pao's model for the energy spectrum, we have modeled the enstrophy spectrum of a horizontal cross-section perpendicular to the rotation axis. Our proposed model for the enstrophy spectrum is in good agreement with the numerical data. We have extended this model to modeled the kinetic energy spectrum of whole 3D decaying rotating turbulence. Again, our extended model in the wavenumber range $2k_\eta < k < k_{max}$ is in good agreement with the numerical results. We have computed the mode-to-mode energy transfer for the decaying rotating turbulence, which reveals that the dominant transfer of energy occurs towards the modes $(\pm 1, 0, 0)$, $(0, \pm 1, 0)$, and $(\pm 1, \pm 1, 0)$.

The numerical studies of the forced rotating turbulence shows a relatively weak columnar structure, although the most dominant energetic modes are still $(\pm 1, 0, 0)$ and $(0, \pm 1, 0)$. A significant amount of energy is also distributed in other modes. The system is anisotropic at smaller wavenumbers, and at larger wavenumbers, it shows isotropic behavior. We have observed a dual cascade of kinetic energy: an inverse cascade of energy for the wavenumber region $k < k_f$ (where k_f is the forcing wavenumber) and a forward cascade of energy in the wavenumber region $k > k_f$. In the anisotropic limit ($k_{\perp} \gg k_{\parallel}$), the anisotropic energy spectrum in the smaller wavenumber range shows KZK spectrum, i.e., $E(k_{\perp}, k_{\parallel}) \sim k_{\perp}^{-5/2} k_{\parallel}^{-1/2}$. As mentioned earlier, the system is isotropic at larger wavenumbers; we modeled the kinetic energy spectrum in this wavenumber region, that is in good agreement with the numerical result. The anisotropic properties of forced rotating turbulence are analyzed by ring decomposition of the Fourier space. The ring energy spectrum of forced rotating turbulence shows that the system is anisotropic at smaller wavenumber whereas nearly isotropic at larger wavenumber in the Fourier space.

The transfer of energy between modes in the Fourier space due to the nonlinear term is a prominent reason for the system to be anisotropic. We have computed the anisotropic energy transfer for the rotating turbulence. Especially, we have focused on the shell-to-shell energy transfer, the ring-to-ring energy transfer, and the conical energy flux. We have decomposed the Fourier space into shells, sectors, and rings. The shell-to-shell energy transfer for decaying rotating turbulence is local and forward. In case of the forced rotating turbulence, we have observed a mixed inverse cascade and forward cascade of energy for $k < k_f$, and a forward cascade of energy for $k > k_f$. The conical energy flux for the decaying case is such that energy is transferred from the polar region towards the equatorial regions. This result is the first numerical validation of Waleffe [188] instability assumption for the transfer of energy in the rotating decaying turbulence. A close analysis of the anisotropic energy transfer, i.e., the ring-to-ring energy transfer for the decaying rotating turbulence, support the results of the conical energy flux, and it also shows that the dominant energy transfer between different shells occurs in the same sectors. The anisotropic energy transfer between rings is local in nature.

In the case of the forced rotating turbulence, the conical energy flux shows that energy is transferred from the equatorial region towards the polar region for the wavenumber range $k < k_f$, and from polar region to equatorial region in the wavenumber range,

$k > k_f$. Again, the ring-to-ring energy transfer supports the results of the conical energy flux. We have observed that the transfer of energy is local between rings, and the dominant energy transfer between different shells predominantly occurs within the same sectors.

6.2 Future directions

In the present thesis, we have examined the statistical properties like kinetic energy spectrum, kinetic energy flux, etc. of the decaying and the forced rotating turbulent flows. We have also modeled the kinetic energy spectrum of decaying in far dissipation range and of forced rotating turbulence in the wavenumber region $k < k_f$. We have shown that the anisotropic energy in the decaying and the forced rotating turbulences is transferred from the polar region to the equatorial region. Here, we discuss some of the possible future projects, that can be extend the scope of our results up to now:

1. The large scale structure is one of the prominent features of rotating turbulence. The Coriolis force affects the large scale of the flow. As a result, the cyclone and anti-cyclone are observed in the flow. To study the mechanism for the reported asymmetry in the strength of cyclones and anti-cyclones in the rotating turbulent flows could be an interesting problem to study [14, 227, 228].
2. In our study, we have used a non-helical force which injects no kinetic helicity in the flow. It may be interesting to investigate the anisotropic behavior of the energy transfer in the rapidly rotating turbulence with helical forcing; many astrophysical, geophysical, engineering rotating flows have non-zero helicities [229–232, 232] in them. Also, the kinetic helicity plays a major role in the rotating flows. Thus, a detailed comparative study of the present work on strongly-rotating turbulence with those on helical rotating turbulence may be quite insightful.
3. As we have emphasized in this thesis, in spite of the similarities between the rotating turbulence and the MHD turbulence, the directions of anisotropic energy transfers in both the systems are at odds with each other: in the MHD turbulence (whether decaying or forced), the transfer is mostly polewards. While it is tempting to comment that the reason for this difference might be traced to the induction

equation—whose counterpart is absent in the hydrodynamic turbulence, it is an open question as to how (if at all) this additional equation brings about the difference in the properties of anisotropic energy transfers of the rotating turbulence and the MHD turbulence.

4. The ring decomposition scheme used in this thesis can also be used to study any other anisotropic system, e.g., 3D rotating Rayleigh–Bénard convection [27, 106], and the rotating stratified flow [9]. In fact, the decomposition can be put to use in finding the detailed behavior of helicity cascade in the rotating helical turbulence and subsequently, to understand how the helicity cascade affects the energy cascade [98, 233].
5. The results presented in the current thesis indicates that the strong rotation induces strong vortical structures. Note that our simulations have very small Rossby number in comparison to the earlier simulations. Weak rotation (Rossby numbers of order 1) is likely to yield energy spectrum with power laws ($E(k) \sim k^{-\alpha}$). It will be interesting to make a comprehensive study of variations of turbulence properties with the variation of Ro.
6. Our investigation highlights that the statistical features of the decaying rotating turbulence and the forced rotating turbulence are quite different. This fact suggests that a similar scientific comparison of the decaying versus the forced turbulences under the simultaneous effects of the rotation and the non-zero kinetic helicity is worth pursuing in future. This is important because, in any realistic experiment of the forced rotating turbulence, the experimental set-ups are such that some finite amount of the kinetic helicity would invariably be imparted to the fluid. Also, the kinetic helicity is significant inside the Earth’s outer core, and is similarly important in the other planets and the stars.
7. At this stage, we don’t have a detailed first-hand understanding of the dependency of scaling of the kinetic energy spectrum on different types of forcing. It will require an elaborate study. Nevertheless, we should point out that Sen et al. [103] investigated the kinetic energy spectrum with different forcing schemes like Taylor–Green (TG), Arnold–Childress–Beltrami (ABC), random, and random anisotropic forcing. In this study, the system was forced at wavenumber $k_f = 40$. In their study the kinetic energy spectra for different forcing schemes showed the following scalings: (a) $E(k_{\perp}) \approx k_{\perp}^{-1}$ for ABC forcing, (b) $E(k_{\perp}) \approx k_{\perp}^{-3}$ for

TG forcing, (c) $E(k_{\perp}) \approx k_{\perp}^{-3}$ for random forcing, and (d) $E(k_{\perp}) \approx k_{\perp}^{-5/3}$ for random anisotropic forcing. The results show that the scaling of the kinetic energy spectrum depends upon the nature of the forcing scheme. It may be an excellent problem to pursue in the future.

Appendix A

Appendix

A.1 Finite-size effects

To verify the finite size scaling, we performed numerical simulations of rotating turbulence in two boxes of sizes $(2\pi)^3$ and $(4\pi)^3$. For the initial condition of these runs, we took our 512^3 simulation data at $t = 98$. In the $(4\pi)^3$ box, $\mathbf{u}(\mathbf{x})$ outside the $(2\pi)^3$ box (central region) was set to zero at $t = 0$. The simulation was carried out till $t_f = 104$. In Fig. A.1(a) and Fig. A.1(b), we exhibit density plots of the vorticity field at $z = \pi$, i.e., $\omega_z(x, y, z = \pi)$, at $t = 100$. We observe that the size of the vortex in the $(4\pi)^3$ box is twice compared to that in $(2\pi)^3$ box. Hence, the large-scale vortex is indeed due to nonlinear effects, and it is independent of the box size. We also compute the integral length scales L for the two boxes, and observe them to be approximately 5.1 and 11.5 respectively. See Fig. A.1(c) for an illustration. Clearly, the integral length scale for $(4\pi)^3$ box is approximately double of that of $(2\pi)^3$ box. Thornber [234] studied the impact of domain size and statistical error in decaying turbulence. Our preliminary studies on strongly-rotating turbulence appear to show that its results are somewhat immune to system size. That is, the Fourier modes and their interactions are independent of the box size.

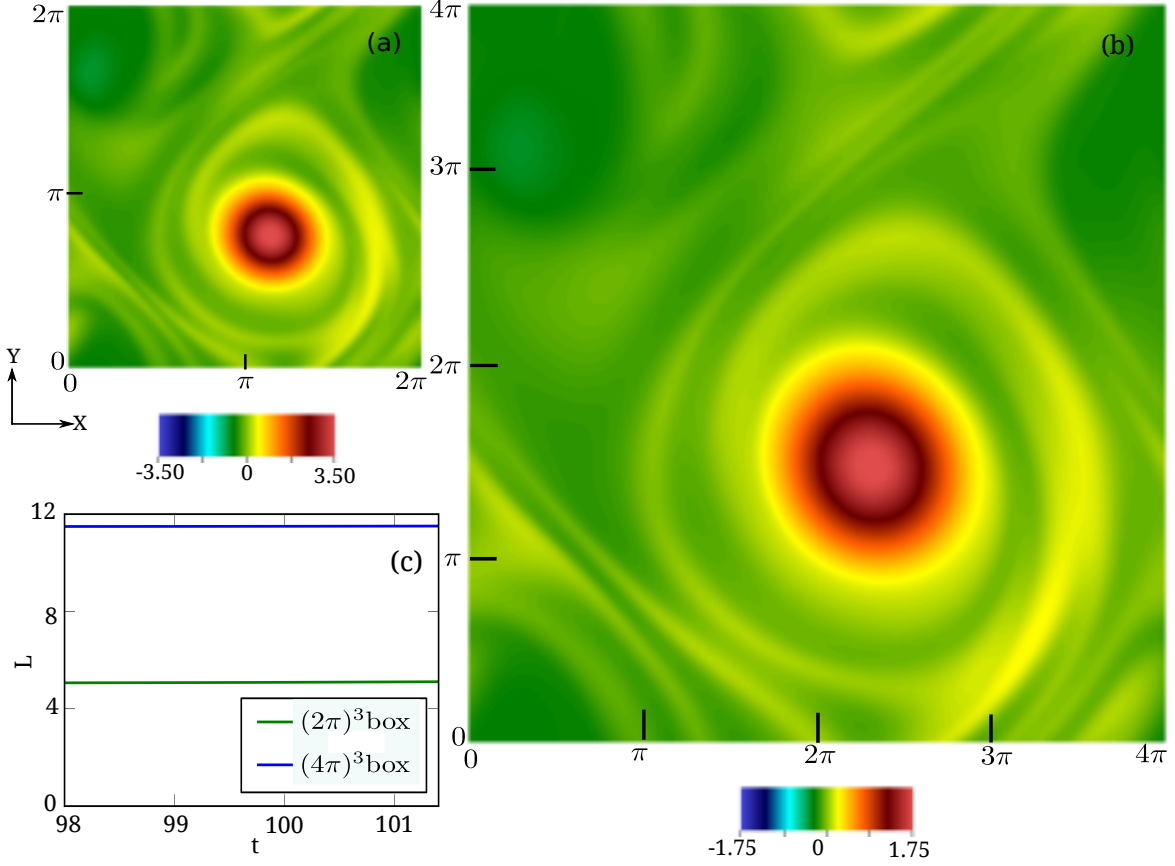


FIGURE A.1: For rapidly rotating turbulence, the density plots of ω_z at $z = \pi$ in boxes of sizes $(2\pi)^3$ (a) and $(4\pi)^3$ (b). For initial condition, we take the 512^2 data at $t = 49$ of Fig. 3.2. Clearly, the size of the vortex in $(4\pi)^3$ box is twice that of $(2\pi)^3$ box. (c) Plots of the time series of integral length scales L in $(2\pi)^3$ (green curve) and $(4\pi)^3$ (blue curve). Here $L_{4\pi} \approx 2L_{2\pi}$.

A.2 Fourier modes $(1, 0, 0)$ and $(0, 1, 0)$ in rotating turbulence

In Sec. 3.3, we showed that $(1, 0, 0)$ and $(0, 1, 0)$ are the most dominant Fourier modes of strongly-rotating turbulence. In this section we discuss the 2D flow pattern when the system has only $(1, 0, 0)$ and $(0, 1, 0)$ Fourier modes. Here we choose the velocity field as

$$\mathbf{u}(x, y) = \hat{x} \sin y + \hat{y} \sin x. \quad (\text{A.1})$$

In Fig. A.2, we exhibit the velocity field along with the density plot of ω_z for the above field. The flow pattern is quite similar to that of Fig. 3.2(f), except that Figure A.2(a)

shows cyclone-anticyclone symmetry, but Fig. 3.2(f) is asymmetric in cyclone-anticyclone pattern. Clearly, the cyclone-anticyclone asymmetry arises due to rotation.

In Appendix A.1 we described the results of numerical simulations of rapidly rotating turbulence. In Fig. A.2(b) we exhibit the time series of energies of Fourier modes $(1,0,0)$, $(0,1,0)$, $(1,1,0)$, and $(-1,1,0)$, along with the total energy E_T . Clearly, the modes $(1,0,0)$, $(0,1,0)$ dominate other modes.

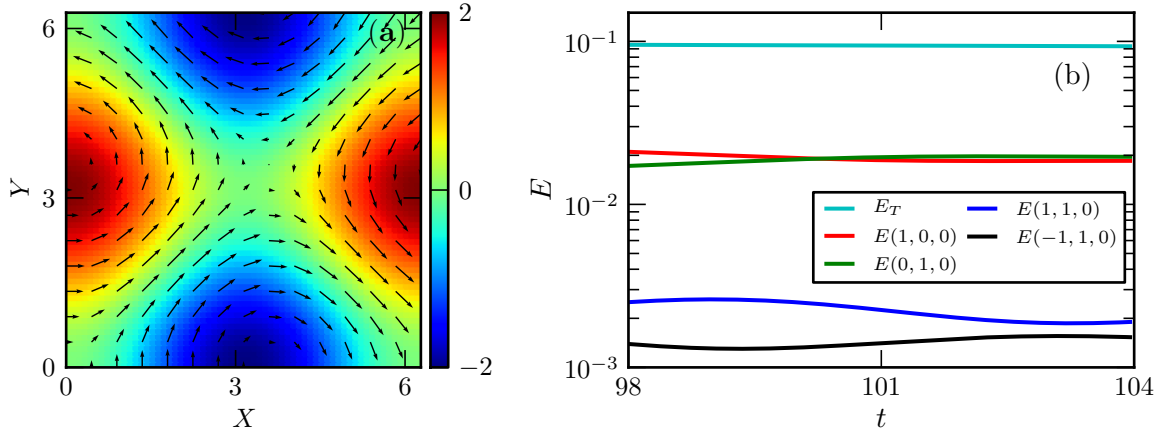


FIGURE A.2: (a) For the 2D velocity field $\mathbf{u}(x, y) = \hat{x} \sin y + \hat{y} \sin x$ that corresponds to the Fourier modes $(1,0,0)$ and $(0,1,1)$, the vector plot of the velocity field superposed with the density plot of the vorticity field ω_z . (b) For the rotating simulation of Appendix A.1, time series of the energies of the modes $(1,0,0)$, $(0,1,0)$, $(1,1,0)$, $(-1,1,0)$ and the total energy E_T .

A.3 Comparison between our model and that of Pao's model

In this section, we argue that for strongly-rotating decaying turbulence, Eq. 3.24 describes the energy spectrum in the intermediate and decaying range. This is the prediction of our model based on the variable enstrophy flux. However, it is important to compare it with the other models. In Figure A.3, we plot $E(k)$ for the numerical data of 1024^3 grid at $t = 49$. The plot also contains $E(k)$ predicted by Eq. 3.24 and that by Pao's model [see Eq. (3.3)]. Clearly, our model performs better than Pao's model.

We also remark that the predictions of Kraichnan's model given by Eq. 3.13 is not suitable for our simulations because $\text{Re} \gg 1$ for our flows. Kraichnan's model assumes

that the nonlinearity is absent, which is not the case for our system. From Eq. 3.13 we deduce that the kinetic energy evolution in Kraichnan's model is

$$E(k, t) = E(k, 0) \exp(-2\nu k^2 t). \quad (\text{A.2})$$

Thus, the evolution of $E(k)$ depends on the initial condition, and $E(k)$ quickly decays to zero.

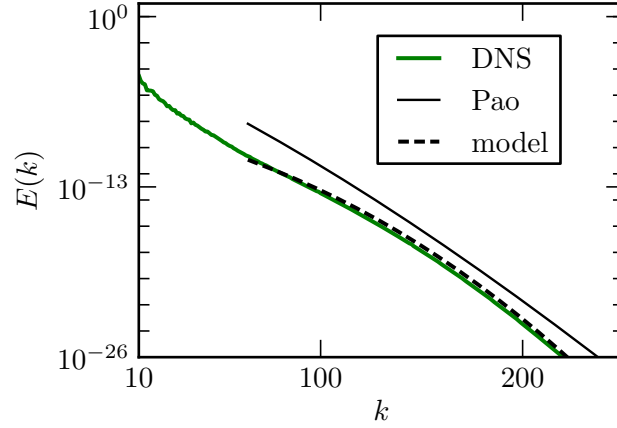


FIGURE A.3: Plot of $E(k)$ for the 3D velocity field of 1024^3 grid along with the predictions of our model and that of Pao. This plot corresponds to the green curve of Figure 3.6.

A.4 Inverse Enstrophy Cascade

We studied the enstrophy flux of plane perpendicular to the axis of rotation. We compute the enstrophy flux of the 2D velocity field \mathbf{u}_\perp at the plane using the formula:

$$\Pi_\omega^{(2D)}(k_*) = \sum_{k > k_*} \sum_{p \leq k_*} S^{\omega\omega}(\mathbf{k}|\mathbf{p}|\mathbf{q}). \quad (\text{A.3})$$

Here,

$$S^{\omega\omega}(\mathbf{k}|\mathbf{p}|\mathbf{q}) = \text{Im}[(\mathbf{k} \cdot \mathbf{u}_\perp(\mathbf{q})) (\omega_z(\mathbf{p})\omega_z^*(\mathbf{k}))], \quad (\text{A.4})$$

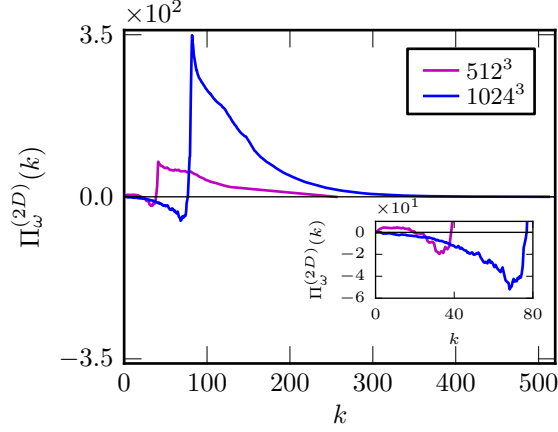


FIGURE A.4: Plot of the 2D enstrophy flux, $\Pi_{\omega}^{(2D)}(k)$, for the 2D velocity field on the horizontal cross-section, $z = \pi$, at $t = t_f$ for the grid-resolutions 512^3 (magenta) and 1024^3 (blue). The inset highlights the inverse cascade of the flux. The peaks in the plots indicate the corresponding forced wavenumbers k_f .

with,

$$\omega_z(\mathbf{k}) = [i\mathbf{k} \times \mathbf{u}(\mathbf{k})]_z, \quad (\text{A.5})$$

represents the enstrophy transfer from mode $\omega_z(\mathbf{p})$ to mode $\omega_z(\mathbf{k})$ with mode $\mathbf{u}(\mathbf{q})$ acting as a mediator. Figure A.4 illustrate the enstrophy flux of the horizontal cross-section taken at $z = \pi$ at time frame $t = 56$ (magenta) for grid resolution of 512^3 and at $t = 3$ (blue) for 1024^3 grid. Arguably [97], when the vortex merger is strong in 2D turbulent flow, the mean enstrophy flux is negative [235, 236] for the scales larger than the injection scales. Therefore, the negative enstrophy flux in the scales larger than the injection scale [as exhibited in Fig. A.4] signifies that our rotating 3D flow is appreciably two-dimensionalized.

We have also computed the 3D enstrophy flux using the formula:

$$\Pi_{\omega}(k_*) = \sum_{|\mathbf{k}| > k_*} \sum_{|\mathbf{p}| \leq k_*} S_{3D}^{\omega\omega}(\mathbf{k}|\mathbf{p}|\mathbf{q}), \quad (\text{A.6})$$

where,

$$S_{3D}^{\omega\omega}(\mathbf{k}|\mathbf{p}|\mathbf{q}) = \text{Im} \{ [\mathbf{k} \cdot \mathbf{u}(\mathbf{q})] [\boldsymbol{\omega}(\mathbf{p}) \cdot \boldsymbol{\omega}^*(\mathbf{k})] \}. \quad (\text{A.7})$$

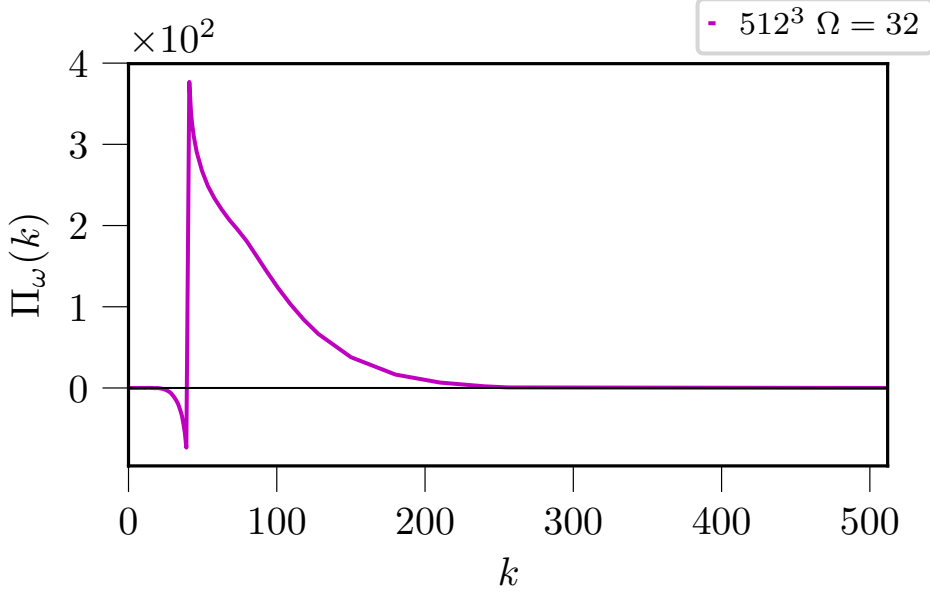


FIGURE A.5: Plot of the 3D enstrophy flux, $\Pi_\omega(k)$, for the 3D velocity field at $t = t_f$ for the grid-resolutions 512^3 . The peaks in the plots indicate the corresponding forced wavenumbers k_f .

In Fig. A.5, we exhibit the 3D enstrophy flux at time frame $t = 56$ for grid resolution of 512^3 with $\Omega = 32$. Here, we observe a forward cascade of enstrophy flux for the wavenumbers greater than the energy injection wavenumber. Apart from the forward cascade of enstrophy flux we also observed an inverse cascade of enstrophy flux in the wavenumber region $k < k_f$.

A.5 Anisotropic Energy Spectrum's Scaling With k_{\parallel}

The KZK spectrum exists in the anisotropic limit, viz., $k_{\perp} \gg k_{\parallel}$, in rapidly rotating turbulence as was shown by Galtier [108] [and we have observed so in Fig. 4.5]; however,

A.5 Anisotropic Energy Spectrum's Scaling With k_{\parallel}

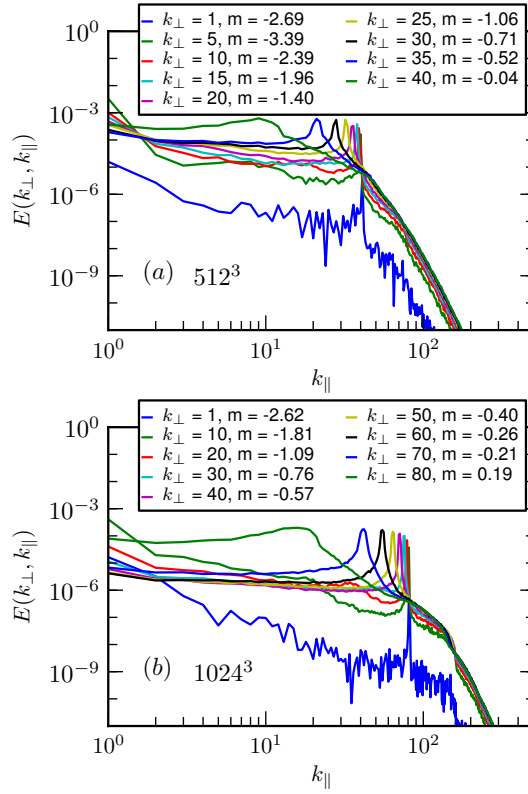


FIGURE A.6: Plots of the (anisotropic) energy spectrum, $E(k_{\perp}, k_{\parallel})$ at $t = t_f$, as a function of k_{\parallel} with different k_{\perp} for (a) 512^3 grid resolution and (b) 1024^3 grid resolution. The fitting exponent (m) in $E(k_{\perp}, k_{\parallel}) \sim k_{\parallel}^{-m}$ has been calculated in the wavenumber range $1 \leq k_{\parallel} \leq 6$ for the 512^3 grid resolution and $1 \leq k_{\parallel} \leq 11$ for the 1024^3 grid resolution is shown in the legends.

that analysis did not include forcing. Since our investigation is for the forced rotating turbulent fluid, we must keep this added complication in mind while extracting the exponent of k_{\parallel} in the anisotropic energy spectrum. The scaling of the energy spectrum as a function of k_{\parallel} depends on the choice of k_{\perp} in the anisotropic limit, which is shown in Fig. A.6.

In Fig A.6, we plot the energy spectrum as a function of k_{\parallel} for different k_{\perp} for both the 512^3 grid resolution and the 1024^3 grid resolution. In order to extract the exponent, we have to not only decide what range of k_{\parallel} to use but also what value of k_{\perp} to choose. Although, one would like to choose a large enough range while maintaining $k_{\perp} \gg k_{\parallel}$, we are restricted in our choice because the peak corresponding to the forcing scale restricts us: the upper bound of the fitting range should ideally be as much away

from the forcing scale as possible but the peak shift towards lower wave number, in line with the identity $k^2 = k_{\perp}^2 + k_{\parallel}^2$, as k_{\perp} increases, thereby making the range smaller. This is at odds with the fact that k_{\perp} must be much greater than k_{\parallel} for witnessing the KZK spectrum. Thus, it effectively becomes a matter of systematic investigation where one should work with all possible combinations of the k_{\parallel} -ranges and the value of k_{\perp} . What we can definitely conclude from Fig. A.6 is that for 512^3 grid resolution, the range $1 \leq k_{\parallel} \leq 6$ and $k_{\perp} = 35$ make an ideal combination which leads to the observation of the KZK-spectrum in the anisotropic limit in the forced rotating turbulence. Similar conclusion can be made for the 1024^3 grid resolution with the range $1 \leq k_{\parallel} \leq 11$ and $k_{\perp} = 35$.

A.6 Integral length scale in decaying rotating turbulence

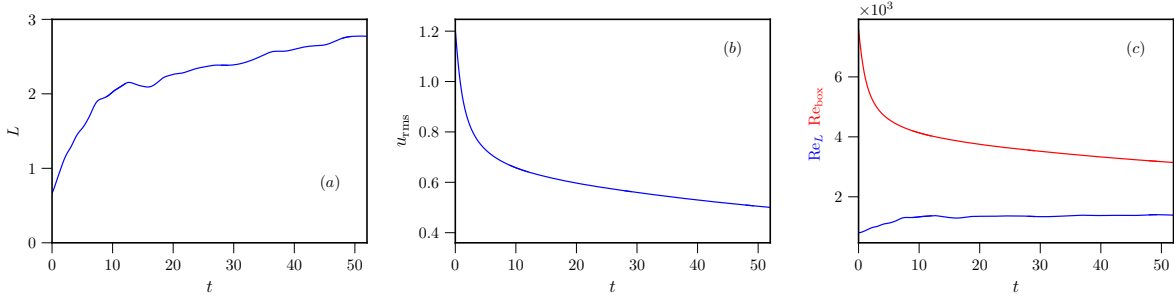


FIGURE A.7: The plots show the time evolutions of (a) the integral length scale, L , (b) rms velocity of the field, u_{rms} , and (c) the Reynolds numbers— Re_{box} (solid red curve) and Re_L (solid blue curve) in decaying rotating turbulence.

As is well known, rotation in a fluid system makes the statistical properties of the fluid anisotropic. Specifically, it leads to the columnar structures as observed in the 3D turbulent fluid in rotation. The coherence of columnar structure can be captured through the integral length scale (L) of the system. We can calculate the integral length scale of the system following Kumar et al. [39]:

$$L := 2\pi \frac{\int_0^{k_{\text{max}}} E(k) k^{-1} dk}{\int_0^{k_{\text{max}}} E(k) dk} = \frac{4\pi}{u_{\text{rms}}^2} \int_0^{k_{\text{max}}} E(k) k^{-1} dk, \quad (\text{A.8})$$

where we have introduced the r.m.s velocity of the field,

$$u_{\text{rms}}^2 := 2 \int_0^{k_{\text{max}}} E(k) dk. \quad (\text{A.9})$$

On plotting the integral length scale of decaying rotating turbulence in Fig. A.7, we find that the integral length scale of the system increases with time which is the signature that the structures become more coherent. This is illustrated better through Fig. 5.1(g) and Fig 5.1(j) where one notes the emergence of sharper columnar structures with time.

Also, we observe in Fig. A.7(b) that u_{rms} of the decaying rotating turbulence is decreasing with time. As a consequence of the nature of the time evolutions of L and u_{rms} , the Reynolds number— $\text{Re}_{\text{box}} := 2\pi u_{\text{rms}}/\nu$ —based on the system size and the Reynolds number— $\text{Re}_L := Lu_{\text{rms}}/\nu$ —based on the integral length scale show contrasting behaviours; while the former decreases with time, the latter increases with time [see Fig. A.7(c)].

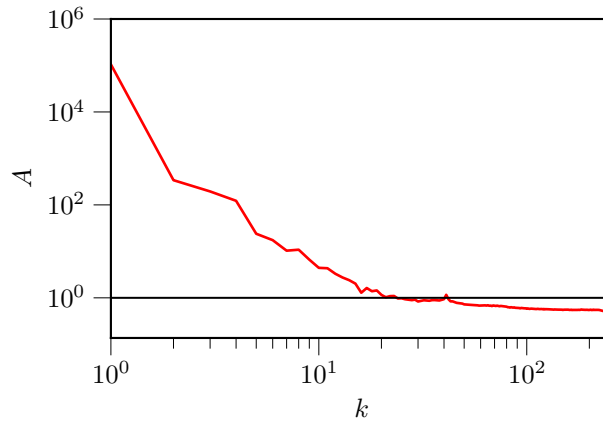


FIGURE A.8: Plot of the anisotropic parameter of system as a function of wavenumber k for forced rotating turbulence at time frame $t = 56$.

A.7 Statistical properties of forced rotating turbulence

Now we briefly outline some of the statistical properties, e.g., anisotropy, kinetic energy spectrum, and kinetic energy flux of the forced rotating turbulence.

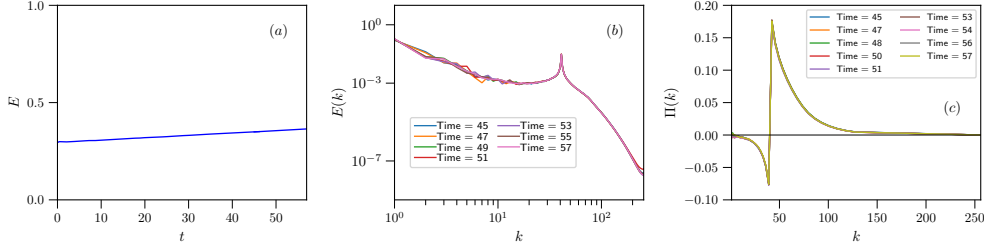


FIGURE A.9: Plots for the time evolution of (a) total energy, (b) the kinetic energy spectrum as a function of k , and (c) kinetic energy flux as a function of k for forced rotating turbulence.

Qualitatively speaking, a rotating turbulent system is dominated by the anisotropic features introduced by the Coriolis force in the band of wavenumbers smaller than the Zeman wavenumber. One of the convenient measures of anisotropy is anisotropic parameter, $A := E_{\perp}/2E_{\parallel}$. Here, $E_{\perp} = E_x + E_y$ and $E_{\parallel} = E_z$, where $E_x = \int (u_x^2/2) d\mathbf{r}$, $E_y = \int (u_y^2/2) d\mathbf{r}$, and $E_z = \int (u_z^2/2) d\mathbf{r}$. The integrations are over the entire volume of the fluid, i.e., the cubic box of size $(2\pi)^3$ in our case. Fig. A.8 highlights the fact that there is very strong anisotropy ($A \gg 1$) in the range of small to intermediate wavenumbers, whereas at larger wavenumbers the system is nearly isotropic ($A \sim 1$).

Next in Fig. A.9(a), we present the time evolution of the total kinetic energy of the forced rotating turbulent system and observe a rather slow increase of energy over 57 large eddy turn-over times; the increase is 23.74% of the total initial energy. In spite of this increase in the total energy, we note that the statistical features like the kinetic energy spectrum [Fig. A.9(b)] and the kinetic energy flux [Fig. A.9(c)] of the forced rotating turbulence system do not change significantly as time progress from $t = 45$ to $t = 57$. Thus, in this thesis, we have reported the statistical results corresponding to the forced system at time frame $t = 56$.

It is also of interest to compare the anisotropic kinetic energy spectrum with the total kinetic energy spectrum of the forced rotating turbulence. Let k_{\perp} denote the wavenumber modes in a plane perpendicular to the direction of rotation axis and k_{\parallel} denote wavenumber modes along the direction of rotation axis. The anisotropic energy

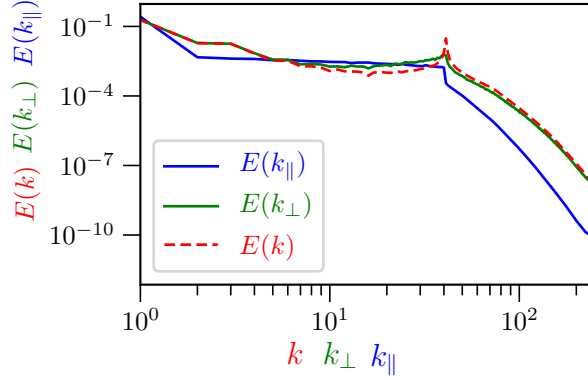


FIGURE A.10: Plots for total kinetic energy spectrum, $E(k)$, as a function of wavenumber k (dashed red curve), $E(k_{\perp})$ as function of k_{\perp} (solid green curve), and $E(k_{\parallel})$ as a function of k_{\parallel} (solid blue curve) for forced rotating turbulence at time frame $t = 56$.

spectrum is, then, defined as

$$E(k_{\perp}, k_{\parallel}) = \sum_{\substack{k_{\perp}-1 < k'_{\perp} \leq k_{\perp}, \\ k_{\parallel}-1 < k'_{\parallel} \leq k_{\parallel}}} \frac{1}{2} |\hat{\mathbf{u}}(k'_{\perp}, k'_{\parallel})|^2. \quad (\text{A.10})$$

From this definition, we can extract following two important statistical quantities:

$$E(k_{\perp}) = \sum_{k_{\parallel}} E(k_{\perp}, k_{\parallel}), \quad (\text{A.11})$$

$$E(k_{\parallel}) = \sum_{k_{\perp}} E(k_{\perp}, k_{\parallel}). \quad (\text{A.12})$$

In Fig. A.11, we have plotted $E(k_{\perp})$ and $E(k_{\parallel})$ for the case of the forced rotating turbulence. We note that $E(k_{\perp})$ plotted as a function of k_{\perp} almost overlaps with the total kinetic energy spectrum, $E(k)$, plotted as a function of k . When we compare them with the plot of $E(k_{\parallel})$ versus k_{\parallel} , we find that comparatively larger share of the energy of the system is accumulated in the modes perpendicular to the direction of the rotation axis.

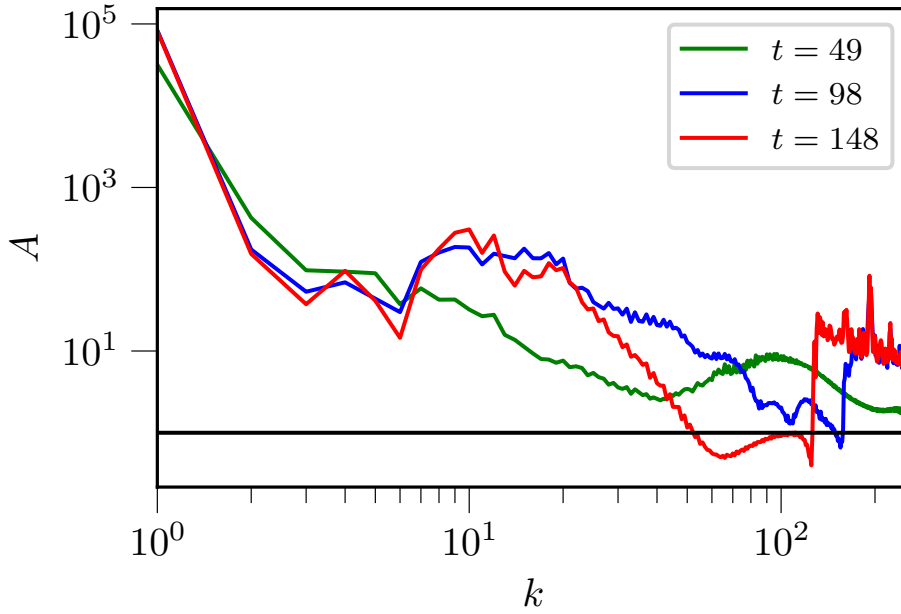


FIGURE A.11: Plots for anisotropy A of decaying rotating turbulence as a function of wavenumber k for different time frames $t = 49$ (red solid curve), $t = 98$ (blue solid curve), and $t = 148$ (red solid curve)

A.8 Scale dependent anisotropy in decaying rotating turbulence

We have plotted the scale-dependent anisotropy A vs wavenumber in fig. A.11 for decaying rotating turbulence at three different time frames i.e. $t = 49$ (solid green curve), $t = 98$ (solid blue curve), and $t = 148$ (solid red curve). We observed that the system is more anisotropic i.e. $A \gg 1$ for lower wavenumbers, and it approaches isotropy at larger wavenumbers.

Bibliography

- [1] E. Yarom, Y. Vardi, and E. Sharon. Experimental quantification of inverse energy cascade in deep rotating turbulence. *Phys. Fluids*, 25(8):085105, 2013.
- [2] C. Lamriben, P.-P. Cortet, F. Moisy, and L. R. M. Maas. Excitation of inertial modes in a closed grid turbulence experiment under rotation. *Phys. Fluids*, 23(1):015102, 2011.
- [3] M. K. Verma. *Energy Transfers in Fluid Flows: Multiscale and Spectral Perspectives*. Cambridge University Press (UK), 2019.
- [4] M. Lesieur. *Turbulence in Fluids*. Springer (Dordrecht), 2012.
- [5] K. S. Reddy, R. Kumar, and M. K. Verma. Anisotropic energy transfers in quasi-static magnetohydrodynamic turbulence. *Phys. Plasmas*, 21(10):102310, 2014.
- [6] O. Zeman. A note on the spectra and decay of rotating homogeneous turbulence. *Phys. Fluids*, 6(10):3221, 1994.
- [7] A. R. Choudhuri. *Physics of Fluids and Plasmas*. Cambridge University Press (UK), 1998.
- [8] J. Theiss. A generalized rhines effect and storms on jupiter. *Geophys. Res. Lett.*, 33(8), 2006.
- [9] P. A. Davidson. *Turbulence in Rotating, Stratified and Electrically Conducting Fluids*. Cambridge University Press (UK), 2013.

BIBLIOGRAPHY

- [10] G. K. Vallis. *Atmospheric and Oceanic Fluid Dynamics: Fundamentals and Large-Scale Circulation*. Cambridge University Press (UK), 2017.
- [11] Y. D. Afanasyev and J. D. C. Craig. Rotating shallow water turbulence: Experiments with altimetry. *Phys. Fluids*, 25(10):106603, 2013.
- [12] L. J. A. Van Bokhoven, H. J. H. Clercx, G. J. van Heijst, and R. R. Trieling. Experiments on rapidly rotating turbulent flows. *Phys. Fluids*, 21:096601, 2009.
- [13] P. J. Staplehurst, P. A. Davidson, and S. B. Dalziel. Structure formation in homogeneous freely decaying rotating turbulence. *J. Fluid Mech.*, 598:1, 2008.
- [14] B. Gallet, A. Campagne, P.-P. Cortet, and F. Moisy. Scale-dependent cyclone-anticyclone asymmetry in a forced rotating turbulence experiment. *Phys. Fluids*, 26(3):035108, 2014.
- [15] A. Campagne, B. Gallet, F. Moisy, and P.-P. Cortet. Direct and inverse energy cascades in a forced rotating turbulence experiment. *Phys. Fluids*, 26(12):125112, 2014.
- [16] C. N. Baroud, B. B. Plapp, Z.-S. She, and H. L. Swinney. Anomalous self-similarity in a turbulent rapidly rotating fluid. *Phys. Rev. Lett.*, 88(11):114501, 2002.
- [17] L. Jacquin, O. Leuchter, C. Cambon, and J. Mathieu. Homogeneous turbulence in the presence of rotation. *J. Fluid Mech.*, 220:1, 1990.
- [18] E. J. Hopfinger, F. K. Browand, and Y. Gagne. Turbulence and waves in a rotating tank. *J. Fluid Mech.*, 125:505, 1982.
- [19] F. S. Godeferd and F. Moisy. Structure and Dynamics of Rotating Turbulence: A Review of Recent Experimental and Numerical Results. *Appl. Mech. Rev.*, 67(3):030802, 2015.
- [20] G. P. Bewley, D. P. Lathrop, L. R. M. Maas, and K. R. Sreenivasan. Inertial waves in rotating grid turbulence. *Phys. Fluids*, 19(7):071701, 2007.
- [21] S. C. Dickinson and R. R. Long. Oscillating-grid turbulence including effects of rotation. *J. Fluid Mech.*, 126:315, 1983.

BIBLIOGRAPHY

- [22] C. Lamriben, P.-P. Cortet, and F. Moisy. Direct measurements of anisotropic energy transfers in a rotating turbulence experiment. *Phys. Rev. Lett.*, 107(2):024503, 2011.
- [23] H. P. Greenspan. *The Theory of Rotating Fluids*. Cambridge University Press (UK), 1968.
- [24] P. A. Davidson. *Turbulence*. Oxford University Press (UK), 2015.
- [25] C. Canuto, M. Y. Hussaini, A. Quarteroni, and T. A. Zhang. *Spectral Methods in Fluid Turbulence*. Springer (Berlin), 1988.
- [26] J. P. Boyd. *Chebyshev and Fourier Spectral Methods*. Dover (NY), 2013.
- [27] M. K. Verma. *Physics of Buoyant Flows*. World Scientific (Singapore), 2018.
- [28] G. Dar, M. K. Verma, and V. Eswaran. Energy transfer in two-dimensional magnetohydrodynamic turbulence: formalism and numerical results. *Physica D*, 157(3):207, 2001.
- [29] F. Waleffe. The nature of triad interactions in homogeneous turbulence. *Phys. Fluids A*, 4(2):350, 1992.
- [30] M. K. Verma. Statistical theory of magnetohydrodynamic turbulence: recent results. *Phys. Rep.*, 401(5):229, 2004.
- [31] M. K. Verma and K. S. Reddy. Modeling quasi-static magnetohydrodynamic turbulence with variable energy flux. *Phys. Fluids*, 27(2):025114, 2015.
- [32] M. K. Verma. Variable enstrophy flux and energy spectrum in two-dimensional turbulence with Ekman friction. *Europhys. Lett.*, 98:14003, 2012.
- [33] M. K. Verma. Anisotropy in Quasi-Static Magnetohydrodynamic Turbulence. *Rep. Prog. Phys.*, 80(8):087001, 2017.
- [34] S. Chakraborty, M. H. Jensen, and A. Sarkar. On two-dimensionalization of three-dimensional turbulence in shell models. *Eur. Phys. J. B*, 73(3):447, 2010.
- [35] S. Chakraborty. Signatures of two-dimensionalisation of 3D turbulence in the presence of rotation. *Europhys. Lett.*, 79(1):14002, 2007.
- [36] V. M. Canuto and M. S. Dubovikov. A dynamical model for turbulence. V. The effect of rotation. *Phys. Fluids*, 9(7):2132–2140, 1997.

BIBLIOGRAPHY

- [37] M. Hossain. Reduction in the dimensionality of turbulence due to a strong rotation. *Phys. Fluids*, 6(3):1077, 1994.
- [38] U. Frisch. *Turbulence*. Cambridge University Press (UK), 1995.
- [39] R. Kumar, M. K. Verma, and R. Samtaney. Energy transfers and magnetic energy growth in small-scale dynamo. *Europhys. Lett.*, 104(5):54001, 2014.
- [40] A. N. Kolmogorov. Dissipation of Energy in Locally Isotropic Turbulence. *Dokl Acad Nauk SSSR*, 32(1):16, 1941.
- [41] S. B. Pope. *Turbulent Flows*. Cambridge University Press (UK), 2000.
- [42] E. A. Novikov. Variation in the dissipation of energy in a turbulent flow and the spectral distribution of energy. *Appl. Math. Mech.*, 25(1445), 1963.
- [43] Robert H. Kraichnan. Isotropic turbulence and inertial-range structure. *Phys. Fluids*, 9(9):1728–1752, 1966.
- [44] Mahendra K. Verma and Jayanta K. Bhattacharjee. Computation of Kolmogorov’s constant in magnetohydrodynamic turbulence. *EPL*, 31(4):195–200, August 1995.
- [45] Katepalli R. Sreenivasan. On the universality of the Kolmogorov constant. *Phys. Fluids*, 7(11):2778, November 1995.
- [46] L.-P. Wang, S. Chen, Brasseur J. G., and J. C. Wyngaard. Examination of hypotheses in the Kolmogorov refined turbulence theory through high-resolution simulations. Part 1. Velocity fields. *J. Fluid Mech.*, 309:113–156, 1996.
- [47] P. K. Yeung and Ye Zhou. Universality of the Kolmogorov constant in numerical simulations of turbulence. *Phys. Rev. E*, 56(2):1746–1752, August 1997.
- [48] Diego A. Donzis and Katepalli R. Sreenivasan. The bottleneck effect and the Kolmogorov constant in isotropic turbulence. *J. Fluid Mech.*, 657:171–188, June 2010.
- [49] G. E. Elsinga and I. Marusic. The anisotropic structure of turbulence and its energy spectrum. *Phys. Fluids*, 28(1):011701, 2016.

BIBLIOGRAPHY

- [50] S. S. Pawar and J. H. Arakeri. Kinetic energy and scalar spectra in high Rayleigh number axially homogeneous buoyancy driven turbulence. *Phys. Fluids*, 28(6):065103, 2016.
- [51] P. Buchhave and C. M. Velte. Measurement of turbulent spatial structure and kinetic energy spectrum by exact temporal-to-spatial mapping. *Phys. Fluids*, 29(8):085109, 2017.
- [52] P. C. Valente, C. B. da Silva, and F. T. Pinho. Energy spectra in elasto-inertial turbulence. *Phys. Fluids*, 28(7):075108, 2016.
- [53] J. Von Neuman.
- [54] U. Frisch and R. Morf. Intermittency in nonlinear dynamics and singularities at complex times. *Phys. Rev. A*, 23:2673–2705, 1981.
- [55] S. G. Saddoughi and S. V. Veeravalli. Local isotropy in turbulent boundary layers at high Reynolds number. *J. Fluid Mech.*, 268:333, 1994.
- [56] Y.-H. Pao. Structure of Turbulent Velocity and Scalar Fields at Large Wavenumbers. *Phys. Fluids*, 8(6):1063, 1965.
- [57] R. H. Kraichnan. The structure of isotropic turbulence at very high Reynolds numbers. *J. Fluid Mech.*, 5:497, 1959.
- [58] L. M. Smith and W. C. Reynolds. The dissipation-range spectrum and the velocity-derivative skewness in turbulent flows. *Phys. Fluids A*, 3:992, 1991.
- [59] K. R. Sreenivasan. On the fine-scale intermittency of turbulence. *J. Fluid Mech.*, 151:81, 1985.
- [60] C. Foias, O. Manley, and L. Sirovich. Empirical and stokes eignfunctions and far-dissipative turbulent spectrum. *Phys. Fluids A*, 2:464, 1990.
- [61] T. Sanada. Comment on the dssipation-range spectrum in turbulent flows. *Phys. Fluids A*, 4:1086, 1992.
- [62] O. P. Manley. The dissipation range spectrum. *Phys. Fluids A*, 4:1320, 1992.
- [63] D. O. Martínez, S. Chen, G. D. Doolen, R. H. Kraichnan, L.-P. Wang, and Y. Zhou. Energy spectrum in the dissipation range of fluid turbulence. *J. Plasma Phys.*, 57(1):195, 1997.

BIBLIOGRAPHY

- [64] S. Kida and Y. Murakami. Kolmogorov similarity in free decaying turbulence. *Phys. Fluids*, 30:2030, 1987.
- [65] J. A. Domaradzki. Nonlocal triad interactions and the dissipation range of isotropic turbulence. *Phys. Fluids A*, 4:2037, 1992.
- [66] S. Chen, G. D. Doolen, J. R. Herring, R. H. Kraichnan, S. A. Orszag, and Z.-S. She. Far-dissipation range of turbulence. *Phys. Rev. Lett.*, 70(20):3051, 1993.
- [67] L D Landau and E M Lifshitz. *Fluid Mechanics*. Butterworth-Heinemann, 1987.
- [68] Andrey Nikolaevich Kolmogorov. A refinement of previous hypotheses concerning the local structure of turbulence in a viscous incompressible fluid at high Reynolds number. *J. Fluid Mech.*, 13:82–85, 1962.
- [69] U. Frisch. Fully developed turbulence and intermittency. *ANN NY ACAD SCI*, 357(1):359–367, 1980.
- [70] A. M. Yaglom. Fluctuations in energy dissipation as influencing the shape of turbulence characteristics in an inertial interval. *Dokl. Akad. Nauk SSSR*, 166:49–52, 1966.
- [71] Katepalli R. Sreenivasan and P. Kailasnath. An Update on the Intermittency Exponent in Turbulence. *Phys. Fluids A*, 5(2):512, February 1993.
- [72] J-P. Laval, B. Dubrulle, and S. Nazarenko. Nonlocality and intermittency in three-dimensional turbulence. *Phys. Fluids*, 13(7):1995–2012, 2001.
- [73] T. Gotoh, D. Fukayama, and T. Nakano. Velocity field statistics in homogeneous steady turbulence obtained using a high-resolution direct numerical simulation. *Phys. Fluids*, 14(3):1065–1081, 2002.
- [74] Charles Meneveau and Katepalli R. Sreenivasan. The multifractal nature of turbulent energy dissipation. *J. Fluid Mech.*, 224:429–484, March 1991.
- [75] Y. Gagne, B. Castaing, C. Baudet, and Y. Malécot. Reynolds dependence of third-order velocity structure functions. *Phys. Fluids*, 16(2):482–485, 2004.
- [76] P. Debue, V. Shukla, D. Kuzay, D. Faranda, E.-W. Saw, F. Daviaud, and B. Dubrulle. Dissipation, intermittency, and singularities in incompressible turbulent flows. *Phys. Rev. E*, 97:053101, 2018.

BIBLIOGRAPHY

- [77] W.-C. Müller and M. Thiele. Scaling and energy transfer in rotating turbulence. *Europhys. Lett.*, 77(3):34003, 2007.
- [78] J Seiwert, C Morize, and F Moisy. On the decrease of intermittency in decaying rotating turbulence. *Phys. Fluids*, 20(7):071702, July 2008.
- [79] P. D. Mininni, A. Alexakis, and A. Pouquet. Scale interactions and scaling laws in rotating flows at moderate Rossby numbers and large Reynolds numbers. *Phys. Fluids*, 21(1):015108, 2009.
- [80] H. Tennekes and J L Lumley. *A First Course in Turbulence*. MIT Press (USA), 1972.
- [81] R. H. Kraichnan. Inertial ranges in two-dimensional turbulence. *Phys. Fluids*, 10:1417, 1967.
- [82] V. Borue. Spectral exponents of enstrophy cascade in stationary two-dimensional homogeneous turbulence. *Phys. Rev. Lett.*, 71:3967, 1993.
- [83] L. M. Smith and V. Yakhot. Bose condensation and small-scale structure generation in a random force driven 2D turbulence. *Phys. Rev. Lett.*, 71(3):352, 1993.
- [84] T. Gotoh. Energy spectrum in the inertial and dissipation ranges of two-dimensional steady turbulence. *Phys. Rev. E*, 57:2984, 1998.
- [85] J. Paret and P. Tabeling. Experimental observation of the two-dimensional inverse energy cascade. *Phys. Rev. Lett.*, 79(21):4162, 1997.
- [86] G. Boffetta, A. Cenedese, S. Espa, and S. Musacchio. Effects of friction on 2D turbulence: An experimental study of the direct cascade. *Europhys. Lett.*, 71(4):590, 2005.
- [87] M. A. Rutgers. Forced 2D turbulence: Experimental evidence of simultaneous inverse energy and forward enstrophy cascades. *Phys. Rev. Lett.*, 81(11):2244, 1998.
- [88] E. Lindborg and K. Alvelius. The kinetic energy spectrum of the two-dimensional enstrophy turbulence cascade. *Phys. Fluids*, 12(5):945, 2000.
- [89] T. Ishihara and Y. Kaneda. Energy spectrum in the enstrophy transfer range of two-dimensional forced turbulence. *Phys. Fluids*, 13(2):544, 2001.

BIBLIOGRAPHY

- [90] N. Schorghofer. Energy spectra of steady two-dimensional turbulent flows. *Phys. Rev. E*, 61:6572, 2000.
- [91] S. Chen, R. E. Ecke, G. L. Eyink, M. Rivera, M. Wan, and Z. Xiao. Physical mechanism of the two-dimensional inverse energy cascade. *Phys. Rev. Lett.*, 96(8):084502, 2006.
- [92] Q. Chen, S. Chen, G. L. Eyink, and D. D. Holm. Intermittency in the joint cascade of energy and helicity. *Phys. Rev. Lett.*, 90:214503, 2003.
- [93] G. Boffetta and R. E. Ecke. Two-Dimensional Turbulence. *Annu. Rev. Fluid Mech.*, 44(1):427, 2012.
- [94] V. Borue. Inverse energy cascade in stationary two-dimensional homogeneous turbulence. *Phys. Rev. Lett.*, 72:1475, 1994.
- [95] M. Chertkov, C. Connaughton, I. Kolokolov, and V. Lebedev. Dynamics of energy condensation in two-dimensional turbulence. *Phys. Rev. Lett.*, 99:084501, 2007.
- [96] C. V. Tran and J. C. Bowman. Robustness of the inverse cascade in two-dimensional turbulence. *Phys. Rev. E*, 69:036303, 2004.
- [97] P. Fischer and C.-H. Bruneau. Wavelet-based analysis of enstrophy transfers in two-dimensional turbulence. *Phys. Fluids*, 21:065109, 2009.
- [98] P. D. Mininni, D. L. Rosenberg, and A. Pouquet. Isotropization at small scales of rotating helically driven turbulence. *J. Fluid Mech.*, 699:263, 2012.
- [99] A. Delache, C. Cambon, and F. S. Godeferd. Scale by scale anisotropy in freely decaying rotating turbulence. *Phys. Fluids*, 26(2):025104, 2014.
- [100] Y. Zhou. A phenomenological treatment of rotating turbulence. *Phys. Fluids*, 7(8):2092, 1995.
- [101] X. Yang and J. A. Domaradzki. Large eddy simulations of decaying rotating turbulence. *Phys. Fluids*, 16(11):4088, 2004.
- [102] L. Biferale, F. Bonaccorso, I. M. Mazzitelli, M. A. T. van Hinsberg, A. S. Lanotte, S. Musacchio, P. Perlekar, and F. Toschi. Coherent Structures and Extreme Events in Rotating Multiphase Turbulent Flows. *Phys. Rev. X*, 6:041036, 2016.

BIBLIOGRAPHY

- [103] A. Sen, P. D. Mininni, D. L. Rosenberg, and A. Pouquet. Anisotropy and nonuniversality in scaling laws of the large-scale energy spectrum in rotating turbulence. *Phys. Rev. E*, 86(3):036319, 2012.
- [104] D. L. Castello and H. J. H. Clercx. Lagrangian velocity autocorrelations in statistically steady rotating turbulence. *Phys. Rev. E*, 83:056316, 2011.
- [105] P. A. Davidson, P. J. Staplehurst, and B. Dalziel, S. On the evolution of eddies in a rapidly rotating system. *J. Fluid Mech.*, 557:135, 2006.
- [106] S. Chandrasekhar. *Hydrodynamic and Hydromagnetic Stability*. Clarendon Press (UK), 1968.
- [107] S. V. Nazarenko and A. A. Schekochihin. Critical balance in magnetohydrodynamic, rotating and stratified turbulence: towards a universal scaling conjecture. *J. Fluid Mech.*, 677:134–153, 2011.
- [108] S. Galtier. Weak inertial-wave turbulence theory. *Phys. Rev. E*, 68(1):015301, 2003.
- [109] P. K. Yeung and Y. Zhou. Numerical study of rotating turbulence with external forcing. *Phys. Fluids*, 10(11):2895, 1998.
- [110] L. M. Smith and F. Waleffe. Transfer of energy to two-dimensional large scales in forced, rotating three-dimensional turbulence. *Phys. Fluids*, 11(6):1608, 1999.
- [111] Y. Hattori, R. Rubinstein, and A. Ishizawa. Shell model for rotating turbulence. *Phys. Rev. E*, 70:046311, 2004.
- [112] L. M. Smith and Y. Lee. On near resonances and symmetry breaking in forced rotating flows at moderate Rossby number. *J. Fluid Mech.*, 535:111, 2005.
- [113] M. Thiele and W.-C. Müller. Structure and decay of rotating homogeneous turbulence. *J. Fluid Mech.*, 637:425, 2009.
- [114] Y. B. Baqui, P. A. Davidson, and A. Ranjan. Are there two regimes in strongly rotating turbulence? *Phys. Fluids*, 28(4):045103, 2016.
- [115] F. Bellet, F. S. Godeferd, J. F. Scott, and C. Cambon. Wave turbulence in rapidly rotating flows. *J. Fluid Mech.*, 562:83, 2006.
- [116] C. Cambon, N. N. Mansour, and F. S. Godeferd. Energy transfer in rotating turbulence. *J. Fluid Mech.*, 337:303, 1997.

BIBLIOGRAPHY

- [117] K. P. Iyer, I. Mazzitelli, F. Bonaccorso, A. Poquet, and L. Biferale. Rotating turbulence under precession like perturbation. *Eur. Phys. J. E*, 38(12):128, 2015.
- [118] L. Biferale, S. Musacchio, and F. Toschi. Split energy-helicity cascades in three-dimensional homogeneous and isotropic turbulence. *J. Fluid Mech.*, 730:309, 2013.
- [119] L. Biferale, S. Musacchio, and F. Toschi. Inverse Energy Cascade in Three-Dimensional Isotropic Turbulence. *Phys. Rev. Lett.*, 108(16):164501, 2012.
- [120] J. Proudman. On the motion of solids in liquids possessing vorticity. *Proc. R. Soc. Lond. A*, 92:408, 1916.
- [121] G. I. Taylor. Experiments with rotating fluids. *Proc. R. Soc. A*, 100:114, 1921.
- [122] C. Morize, F. Moisy, and M. Rabaud. Decaying grid-generated turbulence in a rotating tank. *Phys. Fluids*, 17(9):095105, 2005.
- [123] L. J. A. Van Bokhoven, C. Cambon, L. Liechtenstein, F. S. Godeferd, and H. J. H. Clercx. Refined vorticity statistics of decaying rotating three-dimensional turbulence. *J. Turbul.*, 9(6):1, 2008.
- [124] A. Ibbetson and D. J. Tritton. Experiments on turbulence in a rotating fluid. *J. Fluid Mech.*, 68:639, 1975.
- [125] M. Lesieur, S. Yanase, and O. Métais. Stabilizing and destabilizing effects of a solid-body rotation on quasi-two-dimensional shear layers. *Phys. Fluids A*, 3(3):403, 1991.
- [126] P. Bartello, O. Métais, and M. Lesieur. Coherent structures in rotating three-dimensional turbulence. *J. Fluid Mech.*, 273:1, 1994.
- [127] E. Deusebio, G. Boffetta, E. Lindborg, and S. Musacchio. Dimensional transition in rotating turbulence. *Phys. Rev. E*, 90(2):023005, 2014.
- [128] P. A. Davidson, T. Nickels, and P. Krogstad. The logarithmic structure function law in wall-layer turbulence. *J. Fluid Mech.*, 550:51, 2006.
- [129] J. Bardina, J. H. Ferziger, and R. S. Rogallo. Effect of rotation on isotropic turbulence - Computation and modelling. *J. Fluid Mech.*, 154:321, 1985.
- [130] N. Goldenfeld and H.-Y. Shih. Turbulence as a problem in non-equilibrium statistical mechanics. *J. Stat. Phys.*, 167(3):575, 2017.

BIBLIOGRAPHY

- [131] D. Ruelle. Non-Equilibrium Statistical Mechanics of Turbulence. *J. Stat. Phys.*, 157(2):205, 2014.
- [132] S. Chakraborty, A. Saha, and J. K. Bhattacharjee. Large deviation theory for coin tossing and turbulence. *Phys. Rev. E*, 80(5):056302, 2009.
- [133] A. N. Kolmogorov. The local structure of turbulence in incompressible viscous fluid for very large Reynolds numbers. *Dokl Acad Nauk SSSR*, 30(4):301, 1941.
- [134] A. S. Monin and A. M. Yaglom. *Statistical Fluid Mechanics, Volume 1: Mechanics of Turbulence*, volume 1. Dover (NY), 2007.
- [135] A. S. Monin and A. M. Yaglom. *Statistical Fluid Mechanics, Volume 2: Mechanics of Turbulence*, volume 2. Dover (NY), 2007.
- [136] D. C. Leslie. *Developments in the Theory of Turbulence*. Clarendon Press (Oxford), 1973.
- [137] G. K. Batchelor. *Theory of Homogeneous Turbulence*. Cambridge University Press (UK), 1971.
- [138] R. H. Kraichnan. Inertial-range spectrum of hydromagnetic turbulence. *Phys. Fluids*, 7:1385, 1965.
- [139] P. S. Iroshnikov. Turbulence of a Conducting Fluid in a Strong Magnetic Field. *Sov. Astron.*, 7:566, 1964.
- [140] P. Sagaut and C. Cambon. *Homogeneous Turbulence Dynamics*. Cambridge University Press (UK), 2008.
- [141] S. Chakraborty and J. K. Bhattacharjee. Third-order structure function for rotating three-dimensional homogeneous turbulent flow. *Phys. Rev. E*, 76(3):036304, 2007.
- [142] Y. B. Baqui and P. A. Davidson. A phenomenological theory of rotating turbulence. *Phys. Fluids*, 27(2):025107, 2015.
- [143] Y. Morinishi, K. Nakabayashi, and S. Q. Ren. Dynamics of anisotropy on decaying homogeneous turbulence subjected to system rotation. *Phys. Fluids*, 13:2912, 2001.

BIBLIOGRAPHY

- [144] F. S. Godeferd and L. Lollini. Direct numerical simulations of turbulence with confinement and rotation. *J. Fluid Mech.*, 393:257, 1999.
- [145] L. Bourouiba and P. Bartello. The intermediate Rossby number range and two-dimensional-three-dimensional transfers in rotating decaying homogeneous turbulence. *J. Fluid Mech.*, 587:139, 2007.
- [146] R. H. Kraichnan. Inertial-range transfer in two-and three-dimensional turbulence. *J. Fluid Mech.*, 47:525, 1971.
- [147] W. D. McComb. The inertial-range spectrum from a local energy-transfer theory of isotropic turbulence. *J. Phys. A*, 9(1):179, 1976.
- [148] G. Treviño. Energy transfer in turbulence. *Phys. Fluids A*, 1(12):2061, 1989.
- [149] G. L. Eyink. Energy dissipation without viscosity in ideal hydrodynamics i. fourier analysis and local energy transfer. *Phys. Fluids A*, 78(3):222, 1994.
- [150] J. C. Wyngaard. On the mean rate of energy transfer in turbulence. *Phys. Fluids*, 14(7):2426, 2002.
- [151] S. C. Ling and T. T. Huang. Decay of weak turbulence. *Phys. Fluids*, 13(2912), 1970.
- [152] R. G. Deissler. On the localness of the spectral energy transfer in turbulence. *Appl. Sci. Res.*, 34(4):379, 1978.
- [153] D. W. Carter and F. Coletti. Small-scale structure and energy transfer in homogeneous turbulence. *J. Fluid Mech.*, 854:505, 2018.
- [154] J. A. Domaradzki. Analysis of energy transfer in direct numerical simulations of isotropic turbulence. *Phys. Fluids*, 31(10):2747, 1988.
- [155] J. A. Domaradzki and R. S. Rogallo. Local Energy Transfer and Nonlocal Interactions in Homogeneous, Isotropic Turbulence. *Phys. Fluids A*, 2(3):414, 1990.
- [156] P. K. Yeung and James G. Brasseur. The response of isotropic turbulence to isotropic and anisotropic forcing at the large scales. *Phys. Fluids A*, 3(5):884, 1991.
- [157] S. Kida and K. Ohkitani. Fine structure of energy transfer in turbulence. *Phys. Fluids A*, 4(8):1602, 1992.

BIBLIOGRAPHY

- [158] V. Shanmugasundaram. Modal interactions and energy transfers in isotropic turbulence as predicted by local energy transfer theory. *Fluid Dyn. Res.*, 10(4-6):499, 1992.
- [159] Y. Zhou. Degrees of locality of energy transfer in the inertial range. *Phys. Fluids*, 5:1092, 1993.
- [160] Y. Zhou. Interacting scales and energy transfer in isotropic turbulence. *Phys. Fluids A*, 5(10):2511, 1993.
- [161] J. G. Brasseur and C.-H. Wei. Interscale dynamics and local isotropy in high reynolds number turbulence within triadic interactions. *Phys. Fluids*, 6(2):842, 1994.
- [162] P. K. Yeung, J. G. Brasseur, and Q. Wang. Dynamics of direct large-small scale couplings in coherently forced turbulence: concurrent physical- and fourier-space views. *J. Fluid Mech.*, 283:43, 1995.
- [163] A. Alexakis, P. D. Mininni, and A. Pouquet. Imprint of large-scale flows on turbulence. *Phys. Rev. Lett.*, 95(26):264503, 2005.
- [164] J. A. Domaradzki and D. Carati. An analysis of the energy transfer and the locality of nonlinear interactions in turbulence. *Phys. Fluids*, 19(8):085112, 2007.
- [165] J. A. Domaradzki and D. Carati. A comparison of spectral sharp and smooth filters in the analysis of nonlinear interactions and energy transfer in turbulence. *Phys. Fluids*, 19(8):085111, 2007.
- [166] P. D. Mininni, A. Alexakis, and A. Pouquet. Nonlocal interactions in hydrodynamic turbulence at high reynolds numbers: The slow emergence of scaling laws. *Phys. Rev. E*, 77:036306, 2008.
- [167] G. L. Eyink and H. Aluie. Localness of energy cascade in hydrodynamic turbulence. I. Smooth coarse graining. *Phys. Fluids*, 21:115107, 2009.
- [168] H. Aluie. Localness of energy cascade in hydrodynamic turbulence. ii. sharp spectral filter. *Phys. Fluids*, 21:115108, 2009.
- [169] C. Cambon and L. Jacquin. Spectral approach to non-isotropic turbulence subjected to rotation. *J. Fluid Mech.*, 202(-1):295, 1989.

BIBLIOGRAPHY

- [170] L. M. Smith, J. R. Chasnov, and F. Waleffe. Crossover from two- to three-dimensional turbulence. *Phys. Rev. Lett.*, 77:2467–2470, 1996.
- [171] A. Mahalov and Y. Zhou. Analytical and phenomenological studies of rotating turbulence. *Phys. Fluids*, 8(8):2138, 1996.
- [172] C. Cambon, R. Rubinstein, and F. S. Godeferd. Advances in wave turbulence: rapidly rotating flows. *New J. Phys.*, 6:73, 2004.
- [173] Q. Chen, S. Chen, G. L. Eyink, and D. D. Holm. Resonant interactions in rotating homogeneous three-dimensional turbulence. *J. Fluid Mech.*, 542:139, 2005.
- [174] L. Bourouiba, D. N. Straub, and M. L. Waite. Non-local energy transfers in rotating turbulence at intermediate Rossby number. *J. Fluid Mech.*, 690:129, 2012.
- [175] G. Bordes, F. Moisy, T. Dauxois, and P.-P. Cortet. Experimental evidence of a triadic resonance of plane inertial waves in a rotating fluid. *Phys. Fluids*, 24(1):014105, 2012.
- [176] A. Pouquet, A. Sen, D. L. Rosenberg, P. D. Mininni, and J. Baerenzung. Inverse cascades in turbulence and the case of rotating flows. *Phys. Scripta*, 155:014032, 2013.
- [177] E. Yarom and E. Sharon. Experimental observation of steady inertial wave turbulence in deep rotating flows. *Nat. Phys.*, 10(7):510, 2014.
- [178] P. Clark di Leoni, P. J. Cobelli, P. D. Mininni, P. A. Dmitruk, and W. H. Matthaeus. Quantification of the strength of inertial waves in a rotating turbulent flow. *Phys. Fluids*, 26(3):035106, 2014.
- [179] M. Buzzicotti, P. Clark Di Leoni, and L. Biferale. On the inverse energy transfer in rotating turbulence. *Eur. Phys. J. E*, 41(11):131, 2018.
- [180] M. Buzzicotti, H. Aluie, L. Biferale, and M. Linkmann. Energy transfer in turbulence under rotation. *Phys. Rev. Fluids*, 3:034802, 2018.
- [181] K. Seshasayanan and A. Alexakis. Condensates in rotating turbulent flows. *J. Fluid Mech.*, 841:434, 2018.
- [182] F. Moisy, C. Morize, M. Rabaud, and J. Sommeria. Decay laws, anisotropy and cyclone–anticyclone asymmetry in decaying rotating turbulence. *J. Fluid Mech.*, 666:5, 2010.

BIBLIOGRAPHY

- [183] A. Ranjan and P. A. Davidson. Evolution of a turbulent cloud under rotation. *J. Fluid Mech.*, 756:488, 2014.
- [184] M. K. Sharma, A. Kumar, M. K. Verma, and S. Chakraborty. Statistical features of rapidly rotating decaying turbulence: Enstrophy and energy spectra and coherent structures. *Phys. Fluids*, 30(4):045103, 2018.
- [185] M. K. Sharma, M. K. Verma, and S. Chakraborty. On the energy spectrum of rapidly rotating forced turbulence. *Phys. Fluids*, 30(11):115102, 2018.
- [186] B. Gallet and C. R. Doering. Exact two-dimensionalization of low-magnetic-Reynolds-number flows subject to a strong magnetic field. *J. Fluid Mech.*, 773:154, 2015.
- [187] B. Teaca, M. K. Verma, B. Knaepen, and D. Carati. Energy transfer in anisotropic magnetohydrodynamic turbulence. *Phys. Rev. E*, 79(4):046312, 2009.
- [188] F. Waleffe. Inertial transfers in the helical decomposition. *Phys. Fluids A*, 5(3):677, 1993.
- [189] P. Goldreich and S. Sridhar. Magnetohydrodynamic turbulence revisited. *ApJ*, 485(2):680, 1997.
- [190] S. V. Nazarenko, A. C. Newell, and S. Galtier. Non-local MHD turbulence. *Physica D*, 152:646, 2001.
- [191] O. Schilling and Y. Zhou. Triadic energy transfers in non-helical magnetohydrodynamic turbulence. *J. Plasma Phys.*, 68(5):389, 2002.
- [192] A. Alexakis, P. D. Mininni, and A. Pouquet. Shell-to-shell energy transfer in magnetohydrodynamics. I. steady state turbulence. *Phys. Rev. E*, 72(4):046301, 2005.
- [193] P. D. Mininni, A. Alexakis, and A. Pouquet. Shell-to-shell energy transfer in magnetohydrodynamics. II. Kinematic dynamo. *Phys. Rev. E*, 72(4):046302, 2005.
- [194] O. Debliquy, M. K. Verma, and D. Carati. Energy fluxes and shell-to-shell transfers in three-dimensional decaying magnetohydrodynamic turbulence. *Phys. Plasmas*, 12(4):042309, 2005.
- [195] M. K. Verma, A. Ayyer, and A. V. Chandra. Energy transfers and locality in magnetohydrodynamic turbulence. *Phys. Plasmas*, 12(8):082307, 2005.

BIBLIOGRAPHY

- [196] D. Carati, O. Debliquy, B. Knaepen, B. Teaca, and M. K. Verma. Energy transfers in forced MHD turbulence. *J. Turbul.*, 7(51):1, 2006.
- [197] A. Alexakis, B. Bigot, H. Politano, and S. Galtier. Anisotropic fluxes and nonlocal interactions in magnetohydrodynamic turbulence. *Phys. Rev. E*, 76(5):056313, 2007.
- [198] A. Alexakis. Two-dimensional behavior of three-dimensional magnetohydrodynamic flow with a strong guiding field. *Phys. Rev. E*, 84(5):056330, 2011.
- [199] H. Miura and K. Araki. Structure transitions induced by the hall term in homogeneous and isotropic magnetohydrodynamic turbulence. *Phys. Plasmas*, 21(7):072313, 2014.
- [200] S. Sundar, M. K. Verma, A. Alexakis, and A. G. Chatterjee. Dynamic anisotropy in MHD turbulence induced by mean magnetic field. *Phys. Plasmas*, 24(2):022304, 2017.
- [201] P. Grete, B. W. O'Shea, K. Beckwith, W. Schmidt, and A. Christlieb. Energy transfer in compressible magnetohydrodynamic turbulence. *Phys. Plasmas*, 24(9):092311, 2017.
- [202] Y. Yang, W. H. Matthaeus, Y. Shi, M. Wan, and S. Chen. Compressibility effect on coherent structures, energy transfer, and scaling in magnetohydrodynamic turbulence. *Phys. Fluids*, 29(3):035105, 2017.
- [203] N. T. Baker, A. Pothérat, L. Davoust, and F. Debray. Inverse and direct energy cascades in three-dimensional magnetohydrodynamic turbulence at low magnetic reynolds number. *Phys. Rev. Lett.*, 120:224502, 2018.
- [204] B. Knaepen and R. Moreau. Magnetohydrodynamic turbulence at low magnetic reynolds number. *Annu. Rev. Fluid Mech.*, 40:25, 2008.
- [205] H. K. Moffatt. On the suppression of turbulence by a uniform magnetic field. *J. Fluid Mech.*, 28:571, 1967.
- [206] U. Schumann. Numerical simulation of the transition from three- to two-dimensional turbulence under a uniform magnetic field. *J. Fluid Mech.*, 74:31, 1976.

BIBLIOGRAPHY

- [207] S. Oughton, E. R. Priest, and W. H. Matthaeus. The influence of a mean magnetic field on three-dimensional magnetohydrodynamic turbulence. *J. Fluid Mech.*, 280:95, 1994.
- [208] S. Galtier and B. D. G. Chandran. Extended spectral scaling laws for shear-alfvén wave turbulence. *Physics of Plasmas*, 13(11):114505, 2006.
- [209] T. Teitelbaum and P. D. Mininni. Effect of helicity and rotation on the free decay of turbulent flows. *Phys. Rev. Lett.*, 103(1):014501, 2009.
- [210] M. K. Verma, A. G. Chatterjee, R. K. Yadav, S. Paul, M. Chandra, and R. Samtaney. Benchmarking and scaling studies of pseudospectral code Tarang for turbulence simulations. *Pramana-J. Phys.*, 81(4):617, 2013.
- [211] A. G. Chatterjee, M. K. Verma, A. Kumar, R. Samtaney, B. Hadri, and R. Khurram. Scaling of a fast fourier transform and a pseudo-spectral fluid solver up to 196608 cores. *J Parallel Distrib Comput*, 113(Supplement C):77 – 91, 2018.
- [212] A. J. Chorin and J. E. Marsden. *A mathematical Introduction to Fluid Mechanics*. Springer-Verlag, 1980.
- [213] S.M. Cox and P.C. Matthews. Exponential time differencing for stiff systems. *J. Comput. Phys.*, 176(2):430 – 455, 2002.
- [214] P. Burattini, M. Kinet, D. Carati, and B. Knaepen. Spectral energetics of quasi-static MHD turbulence. *Physica D*, 237(1):2062, 2008.
- [215] P. Vorobieff, M. Rivera, and R. E. Ecke. Soap film flows: Statistics of two-dimensional turbulence. *Phys. Fluids*, 11(8):2167, 1999.
- [216] D. Carati, S. Ghosal, and P. Moin. On the representation of backscatter in dynamic localization models. *Phys. Fluids*, 7(3):606, 1995.
- [217] K. Yoshimatsu, M. Midorikawa, and Y. Kaneda. Columnar eddy formation in freely decaying homogeneous rotating turbulence. *J. Fluid Mech.*, 677:154, 2011.
- [218] C. N. Baroud, B. B. Plapp, H. L. Swinney, and Z.-S. She. Scaling in three-dimensional and quasi-two-dimensional rotating turbulent flows. *Phys. Fluids*, 15(8):2091, 2003.
- [219] H. J. H. Clercx and G. J. F. Van Heijst. Two-Dimensional Navier–Stokes Turbulence in Bounded Domains. *Appl. Mech. Rev.*, 62:020802, 2009.

BIBLIOGRAPHY

- [220] J. Qian. Universal equilibrium range of turbulence. *The Physics of Fluids*, 27(9):2229–2233, 1984.
- [221] Y. Zhu and R. A. Antonia. The spatial resolution of hot-wire arrays for the measurement of small-scale turbulence. *Measurement Science and Technology*, 7(10):1349–1359, oct 1996.
- [222] M. K. Verma, A. Kumar, P. Kumar, S. Barman, A. G. Chatterjee, R. Samtaney, and R. A. Stepanov. Energy spectra and fluxes in dissipation range of turbulent and laminar flows. *Fluid Dyn.*, 53(6):862, 2018.
- [223] S. H. Strogatz. *Nonlinear Dynamics and Chaos: With Applications to Physics, Biology, Chemistry and Engineering*. Westview press (US), 2014.
- [224] F. Moisy, C. Morize, M. Rabaud, and J. Sommeria. Decay laws, anisotropy and cyclone–anticyclone asymmetry in decaying rotating turbulence. *J. Fluid Mech.*, 666:5, 2011.
- [225] M. K. Sharma, M. K. Verma, and S. Chakraborty. Anisotropic energy transfers in rapidly rotating turbulence. *Phys. of Fluids*, 31(8):085117, 2019.
- [226] B. Favier, F. S. Godeferd, C. Cambon, and A. Delache. On the two-dimensionalization of quasistatic magnetohydrodynamic turbulence. *Phys. Fluids*, 22(7):075104, 2010.
- [227] B. Sreenivasan and P. A. Davidson. On the formation of cyclones and anticyclones in a rotating fluid. *Phys. Fluids*, 20:085104, 2008.
- [228] Aurore N. Cyclone-anticyclone asymmetry and alignment statistics in homogeneous rotating turbulence. *Physics of Fluids*, 27(3):035108, 2015.
- [229] A. M. Soward, C. A. Jones, D. W. Hughes, and N. O. Weiss. *Fluid Dynamics and Dynamos in Astrophysics and Geophysics*. CRC Press (US), 2002.
- [230] P. M. Bellan. *Magnetic Helicity, Spheromaks, Solar Corona Loops, And Astrophysical Jets*. World Scientific, Singapore (Singapore), 1948.
- [231] K. C. Tsinganos. *Solar and Astrophysical Magnetohydrodynamic Flows*. Kluwer Academic (Dordrecht), 1996.
- [232] Dr. M. Boyce P.E. *Centrifugal Compressors: A Basic Guide*. PennWell Corporation (USA), 2003.

BIBLIOGRAPHY

- [233] P. D. Mininni and A. Pouquet. Rotating helical turbulence. I. Global evolution and spectral behavior. *Phys. Fluids*, 22(3):035105, 2010.
- [234] B. Thornber. Impact of domain size and statistical errors in simulations of homogeneous decaying turbulence and the Richtmyer-Meshkov instability. *Phys. Fluids*, 28(4):045106, 2016.
- [235] K. Ohkitani. Wave number space dynamics of enstrophy cascade in a forced two-dimensional turbulence. *Phys. Fluids A*, 3:1598, 1991.
- [236] A. Babiano and Antonello P. Coherent vortices and tracer cascades in two-dimensional turbulence. *J. Fluid Mech.*, 574:429, 2007.